2004

Study of the Excited-State Absorption Properties of Polymethine Molecules

Richard Stanley Lepkowicz
University of Central Florida

UNIVERSITY OF CENTRAL FLORIDA
DISSERTATION APPROVAL

The members of the Committee approve the dissertation entitled *Study of the Excited-State Absorption Properties of Polymethine Molecules* by Richard Lepkowicz, defended February 24, 2004.

Eric W. Van Stryland, Chair

David J. Hagan, Co-Chair

George Stegeman
Committee Member

Florencio Hernandez
Committee Member

Shin-Tson Wu
Committee Member

It is recommended that this dissertation be used in partial fulfillment of the requirements for the degree of Doctor of Philosophy in the School of Optics.

David J. Hagan, Associate Director

Eric W. Van Stryland, Director

Patricia J. Bishop
Vice Provost and Dean of Graduate Studies

The committee, the college, and the University of Central Florida are not liable for any use of the materials presented in this study.

STUDY OF THE EXCITED-STATE ABSORPTION PROPERTIES OF POLYMETHINE MOLECULES

by

RICHARD STANLEY LEPKOWICZ
B.S. Georgia Institute of Technology, 1998
M.S. University of Central Florida, 2000

A dissertation submitted in partial fulfillment of the requirements
for the degree of Doctor of Philosophy
in the School of Optics
at the University of Central Florida
Orlando, Florida

Spring Term
2004

Major Professors: Eric W. Van Stryland and David J. Hagan

ABSTRACT

This dissertation investigates excited-state nonlinearities in a series of polymethine dyes for the application of nanosecond optical limiting. Optical limiters are devices that for low intensity light exhibit a high linear transmittance, but for high intensity light strongly attenuate the incident radiation. These devices would serve to protect optical sensors from intense laser radiation by clamping the maximum energy allowed through an optical system below the damage threshold of the sensor. The search is ongoing for optical materials that are both broadband and have high damage thresholds to be effective materials for limiting applications. Polymethine dyes are promising compounds due to a strong and broad excited-state absorption (ESA) band in the visible region. However, the effectiveness of polymethine molecules as applied to optical limiting is hindered by a saturation of the ESA process at high fluences.

Experiments and theoretical modeling are performed to determine the root causes of this saturation effect in both the picosecond and nanosecond time regime. The polymethine molecules studied have chromophore lengths from di- to pentacarbocyanine (2 to 5 -CH=CH- groups) with various bridge structures. This allows us to develop relationships between the molecular parameters of the polymethine molecules and overall nonlinear absorption performance. The experiments conducted included femtosecond white light continuum pump-probe experiments to measure ESA spectra, picosecond two-color polarization-resolved pump-probe to measure excited-state dynamics and the orientation of transition dipole moments, and picosecond and nanosecond optical limiting and z-scans. From these experiments we are able to

develop energy level models that describe the nonlinear absorption processes in polymethines from the picosecond to nanosecond time regime.

This work, along with the quantum chemical modeling performed at the Institute of Physics and National Academy of Sciences of Ukraine, has resulted in the creation of dyes that have improved photochemical stability with larger nonlinearities. These are useful not only for optical limiting but also for a wide variety of nonlinear optical applications.

This dissertation is dedicated to my parents, Patricia and Leonard Lepkowicz, my wife Heather, and our three kids; Ra, Josephine, and Abigail, for their continuous support and encouragement over the years.

ACKNOWLEDGMENTS

I would first like to thank my advisors, Dr. Eric W. Van Stryland and Dr. David J. Hagan, for giving me the opportunity to work in their labs. It has been a real pleasure, and I have learned a great deal working with them over the years.

I am also deeply grateful for the opportunity to work with Dr. Olga Prhzonska from the Institute of Physics and National Academy of Sciences of Ukraine. She not only provided the polymthine molecules studied in this dissertation, but also countless discussions and emails trying to teach an optics student some organic chemistry. Without her this dissertation would not have been possible.

I would also like to thank the graduate students and post-docs I have worked with in the nonlinear optics group over the years. In particular I would like to thank Joel Hales for helping me make it through CREOL, he is a great friend and someone I admire greatly. Special thanks go to Dr. Andrey Kobyakov for teaching me how to approach new problems and write scientific papers. His guidance on theoretical calculations was invaluable to me. I would like to thank Dr. Eloy Hernandez for his expertise on lab skills. He taught me several of my lab skills I have developed over the years.

Finally, I would like to express my gratitude to the entire faculty, staff, and students for making my time at CREOL a great experience. Special thanks go to Dr. George Stegeman, Dr. Shin-Tson Wu, and Dr. Florencio Hernandez for sitting on my committee.

TABLE OF CONTENTS

LIST OF FIGURES

LIST OF TABLES

LIST OF ABBREVIATIONS

Acronym/Unit	Description
2PA	Two-photon absorption
BBO	Beta-barium borate
CAP	Chloroaluminum phthalocyanine
CCD	Charge coupled device
CS_2	carbon disulfide
ESA	Excited-state absorption
FWHM	Full width half maximum
HITCI	1,1',3,3,3',3'-hexamethylindotricarbocyanine iodide
HOMO	Highest occupied molecular orbitals
HW $1/e^2$M	Half width $1/e^2$ maximum
K-K	Kramers-Kronig
KDP	Potassium dihydrogen phosphate
KD^*P	Potassium dideuterium phosphate
LUMO	Lowest unoccupied molecular orbitals
NLO	Nonlinear optics
ND:YAG	Neodymium -doped Yttrium Aluminum Garnet
ODE	Ordinary differential equation
OPG/A	Optical parametric generator/amplifier

OPO	Optical parametric oscillator
PD	Polymethine Dyes
PDE	Partial differential equation
PUA	Polyurethane acrylate elastopolymer
RSA	Reverse saturable absorption
SA	Saturable absorption
SHG	Second harmonic generation
THG	Third harmonic generation

CHAPTER 1: INTRODUCTION

This chapter provides an introduction to nonlinear optical phenomenon in general, and quickly delves into excited-state absorption (ESA) which is the primary optical nonlinearity studied in this dissertation. This includes a formal definition of excited-state absorption as well as an historical account of excited-state absorption which is covered in Section 1.1.1. What follows in Section 1.1.2 is an overview of the applications of excited-state absorption. The structure and characteristics of the polymethine molecules, which are the primary molecules studied in this dissertation are reviewed in Section 1.1.3. The dissertation statement is given in Section 1.2. The chapter is concluded with the dissertation outline in Section 1.3.

1.1 Background and Motivation

The field of nonlinear optics (NLO) covers the interaction of intense light fields with matter, which encompasses the study of fundamental aspects of light and matter all the way to applications such as optical switching [1,2,3]. Even though the nonlinear nature of Maxwell's constitutive relationships were known before the advent of the laser, experiments were not performed until after its invention in 1960 [4]. The observation of second-harmonic generation by Franken et. al. in 1961 [5] is considered the beginning of the field. Second-harmonic generation corresponds to a second order nonlinearity ($\chi^{(2)}$), which encompasses other effects such as difference frequency generation, optical rectification, linear electro-optic effect, and parametric emission. The third order term ($\chi^{(3)}$) gives rise to nonlinear refraction, two-photon absorption (2PA) , stimulated Raman and Brillouin scattering, and four-wave mixing. The

nonlinear refraction and the two-photon absorption are the instantaneous terms most closely related to the type of nonlinearity studied in this dissertation, so they will briefly be discussed.

The 2PA process is associated with the imaginary part of $\chi^{(3)}$, whereas the nonlinear index is connected with the real part of $\chi^{(3)}$. It is important to note that 2PA is interrelated with the change in the refractive index (nonlinear index) by the nonlinear Kramers-Krönig (K-K) relationship [6]. The main characteristic of 2PA is that it is an instantaneous process, which means the two photons are absorbed virtually simultaneously ($\sim 10^{-15}$ s). This makes 2PA processes dependent on the irradiance (energy per unit area per unit time) of the incident pulse. The 2PA process can crudely be modeled as a two step absorption process where the first photon is absorbed into a virtual state that has an infinitesimal lifetime. ESA, on the other hand, is a nonlinear absorption process in which the absorption of the material is based on the incident fluence (energy per unit area) as long as the lifetime of the excited-state is longer than that of the pulse width of the incident beam. ESA can be considered to be a nonlinear absorption process that arises out of the cascading of two linear absorption processes, also known as a cumulative nonlinearity. ESA will be discussed in detail in the following Sections.

1.1.1 Definition and Historical Account of ESA

Depending on the properties of the material, ESA can affect the absorption as a function of fluence in two drastically different ways. The first type is known as saturable absorption (SA) or optical "bleaching" in which the absorption of the material decreases with increasing fluence. Labeling SA as an ESA process in certain cases can be a misnomer since only two energy levels are required, but in the context of this dissertation in which we are dealing with large organic

molecules that have several excited-state levels that are broad due to their vibrational levels it is appropriate. The other type of ESA being an increase in absorption as a function of increasing fluence and is referred to as reverse saturable absorption (RSA).

Saturable absorption was the first type of ESA experimentally observed in 1941 by Lewis et al. [7]. But before the work of Giuliano and Hess in 1967 [8] it was believed that the optical bleaching seen in organic molecules under intense radiation was due to equalization of the transition rate of absorption and that of stimulated emission. Giuliano and Hess proved that stimulated emission would be negligible in complex organic molecules due to the ultrafast decay time of the vibronic sublevels of the excited states, which would detune the energy of the excited state from the incident light energy. Thus, without stimulated emission, an intense pulse could in essence completely deplete the ground state population and highly populate an excited state. The simplest model to describe ESA processes is the three-level all-singlet model shown in Figure 1.1. It is important to note that labeling the higher excited-state as S_2 doesn't necessarily mean that the ESA transition is to the real second level of the excited-state of the molecule, and the true level can only be determined through quantum chemical modeling. It will be shown in Chapter 3 that the excited-state transition for polymethines is connected with the S_1 to S_5 transition. The ground- and excited-state cross-sections are denoted by σ_{01} and σ_{12}, respectively. Associated with each energy level (S_0, S_1, and S_2) is a series of closely spaced vibronic sublevels that have sub-picosecond relaxation times. The lifetime of the first excited-state is typically in the range of 100's of picoseconds to several nanoseconds and is denoted as τ_{10}. The higher excited-state lifetime (τ_{21}) is on the order of several picoseconds. In terms of this model SA and RSA can be described in the following context. In the case of optical bleaching the excited-state

cross-section is smaller than the ground-state cross-section, thus when S_1 becomes highly populated the absorption of the material decreases. For an RSA material the excited-state cross-section is larger than the ground-state cross-section, and in this case when S_1 becomes highly populated the absorption of the material increases.

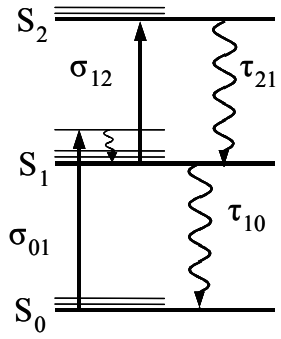

Figure 1.1: Three-level energy manifold schematic of an excited-state absorber; S_0 is the ground state; S_1 and S_2 are the excited singlet states.

Giuliano and Hess used a five-level model of the energy manifold of organic molecules to explain the dynamics of excited-state absorption. This model is shown in Figure 1.2 and is widely accepted today as the generic model for an excited-state absorber [9]. The five-level model starts with the three-level model shown in Figure 1.1 and adds a second decay pathway (τ_{13}) from the first excited-state (S_1) to a triplet state (T_1) which has its own ESA characteristics (σ_{34}, τ_{43}). The main characteristic being a long lifetime (τ_{30}), which is advantageous for nanosecond limiting applications.

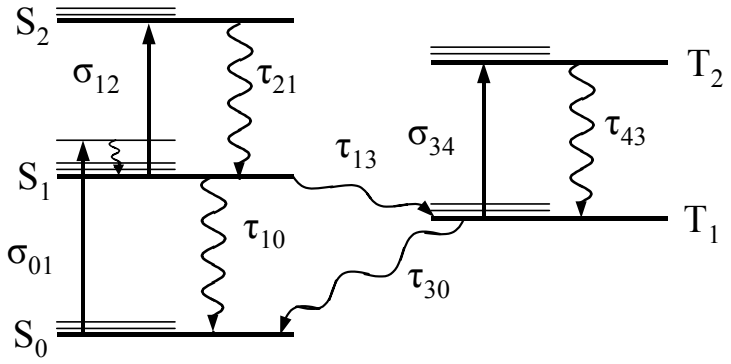

Figure 1.2: Five-level energy manifold schematic of an excited-state absorber. S_0 is the ground state; S_1 and S_2 are the excited singlet states and T_1 and T_2 are triplet states.

1.1.2 Applications of ESA

The initial interest in ESA materials occurred in the mid-1960's for shortening the temporal pulse widths of lasers passively through Q-switching [10] and mode locking [11]. Both of these phenomena are based on SA and a lot of work was spent on modeling these processes [12,13,14], which laid the ground work for an understanding of RSA processes that started to be investigated in the mid-1970's [15,16]. It took nearly another decade after RSA materials were identified before applications were developed using them. Initially the interest for RSA materials was in optical pulse processing applications such as mode locking [17] or pulse compression [18]. However, in 1984 when Harter et. al. demonstrated that RSA materials could be used as passive power/energy limiters, [19] the real explosion in the field of RSA materials occurred. A power/energy (optical) limiter is a device that for low intensity light exhibits a high linear transmittance, but for high intensity light strongly attenuates the incident radiation. These

devices would serve to protect optical sensors from intense laser radiation by clamping the maximum energy allowed through an optical system below the damage threshold of the sensor, be it an eye or an electronic optical detector. Harter et. al. defined five criteria for an RSA material to function as an optical limiter at a specific wavelength as:

(1) Excited state absorption cross-section (σ_{12}) must be larger than the ground state absorption cross-section (σ_{01}) (see Figure 1.1).

(2) Ground state absorption cross-section (σ_{01}) is large so that the incident radiation saturates the first excited state (S_1).

(3) Neither of the excited states involved in the RSA process decay to other levels that trap the excitation.

(4) Stimulated emission is negligible.

(5) The lifetime of the first excited state (τ_{10}) is short compared to the pulse width (τ_p) for an irradiance dependent limiter or the lifetime is long compared to the pulse width for a fluence dependent limiter.

Several different nonlinear optical processes in various materials are being investigated for passive optical limiting applications [20]. But there are several reasons why RSA in organic molecules is particularly attractive compared to other mechanisms such as two-photon and free carrier absorption, nonlinear refraction, and induced scattering. For molecules in which the excited-state absorption cross-section (σ_{12}) is large compared to that of the ground-state absorption cross-section (σ_{01}) there exists the possibility of having large nonlinear absorption while maintaining high linear transmittance. Due to the fact that the light is absorbed as opposed

to being spread (e.g. nonlinear scattering or refraction) it was suggested by Perry [9] that the limiting may be more reliable and could be used in highly convergent optical systems. In molecules which possess singlet (S_1-S_2) and triplet (T_1-T_2) ESA the nonlinear absorption should work for a wide range of pulse widths (picosecond to microsecond). The main advantage organic molecules have over other materials is the ability to systematically alter the chemical structure, thus allowing the ability to tailor specific photophysical properties and maximize the nonlinearity. Because of these reasons optical limiting has been investigated in a number of different organic molecules such as porphyrins, fullerenes, phthalocyanines, and naphthalocyanines [9,20,21,22,23]. The best of these materials have possessed excited-state absorption cross-sections up to 30 times that of the ground-state cross-section, while having a ground-state cross-section at the excitation wavelength of 10^{-18} to 10^{-17} cm^2. Polymethine molecules on the other hand have been shown to possess excited-state cross-sections up to 200 times that of the ground state cross-section in the visible region (532 nm), while having a ground-state cross-section of the same order of magnitude as the phthalocyanines (10^{-18} cm^2) at the excitation wavelength [24]. All of these molecules including the polymethines have shortcomings that prevent them from behaving as ideal materials for optical limiting. More importantly it is not well understood how or even if any of these known materials can be modified to get the desired nonlinear response over a given spectral range (i.e. visible 400 – 700 nm). We believe that there is great promise in the polymethines of being able to achieve this goal since they possess a large ground-state absorption cross-section, which allows for complete population of the excited-state, while maintaining the largest known ratio of excited-state to ground-state cross-sections. It is important to note that while in this dissertation we constantly

refer to the ratio of excited-state to ground-state cross-sections the difference is the quantity that appears in the propagation equation. The ratio can be misleading because it doesn't provide information about the size of the cross-sections, and therefore two dyes with the same ratio can have drastically different ESA properties. However, all the polymethines studied in this dissertation have ground-state cross-sections of the same order of magnitude so only stating the ratio is an accurate comparison.

1.1.3 Structure and Characteristics of Polymethine Molecules

Polymethine dyes have been used for various applications since the turn of the century. Polymethine dyes were first primarily used in photography to extend the spectral response of silver halide [25]. After the invention of the laser, polymethine dyes were used in applications such as saturable absorbers for Q-switching and modelocking [26], and gain medium in dye lasers [27]. The name polymethine refers to the resonant chain of the molecule, which is the light absorbing chromophore of the molecule. The polymethine chromophore is composed of the streptocyanine cationic dye family shown in Figure 1.3a, where R and R` are alkyl groups. The key feature of the polymethine chromophore is an alternating partial charge (δ^+ and δ^- are positive and negative, respectively) of the methine groups (-C=) along with an equalization of the bond lengths as shown in Figure 1.3b. This property allows for large delocalization of the π-electron system.

(a) 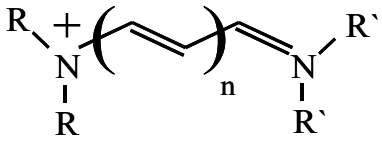

(b) 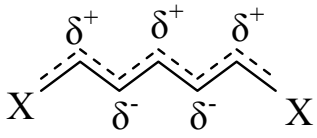

Figure 1.3: (a) Streptocyanine cation that constitutes the polymethine chromophore, R, R' are alkyl groups. (b) π electron distribution of polymethine chromophore, where X is electronegative terminal groups w.r.t. the carbon atom.

The vinyl group (-CH=CH-) in the polymethine chain can be as large as 7 (n=7) units [28]. Polymethine dyes are typically not photochemically stable and the stability degrades as the chain length is increased from the cyanine limit (n=0) to the carbocyanine (n=1) and on to the di- , tri-, etc. carbocyanine structures. In this dissertation we work with polymethines of chain length up to pentacarbocyanines. All the chemical structures are displayed in Figure 1.4. It should also be noted that much work has been spent on making this series of dyes photochemically stable [24]; with the exception of the pentacarbocyanine dyes, which were only recently synthesized.

PD 2350		PD2351
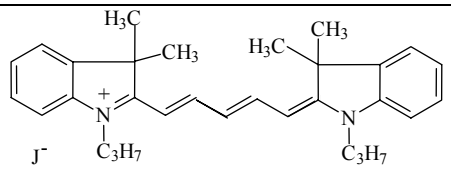		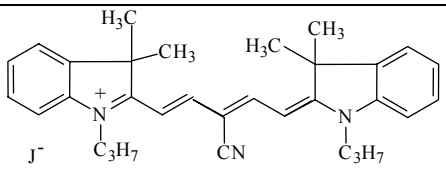
PD2335		**PD2238**
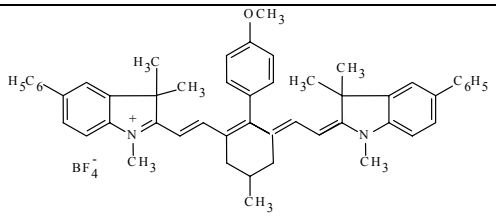		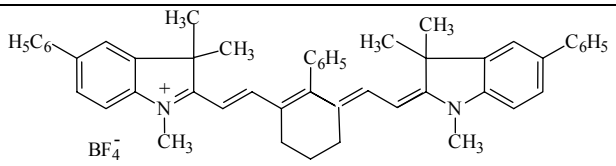
PD824		**PD2332**
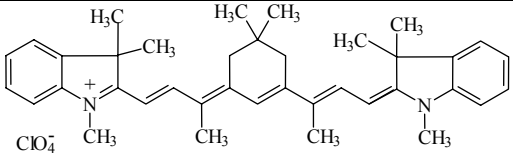		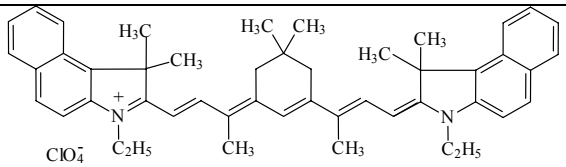
PD2257		**PD3428**
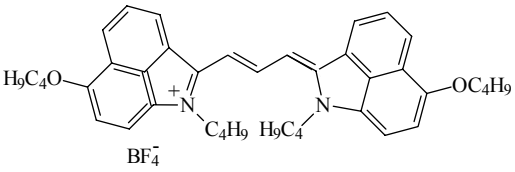		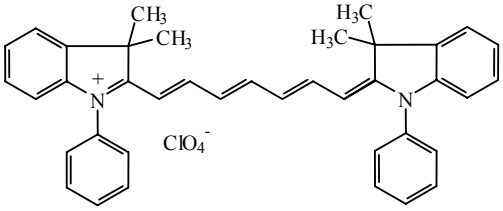
PD1952		**PD2410**
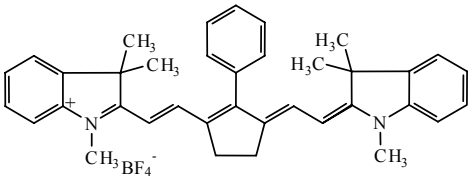		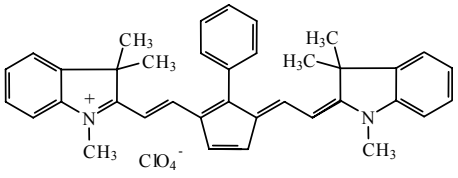
PD1659		**PD2398**
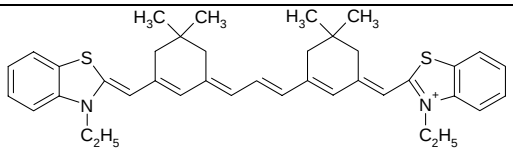		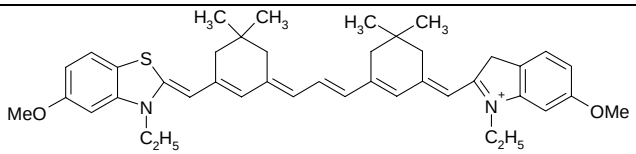

Figure 1.4: Chemical structure of the polymethine dyes studied in this dissertation.

The chemical names of the dyes shown in Figure 1.4 are listed in appendix A, but the general distinction between these dyes can be made as a function of the polymethine chain length: di- (PDs 2350 and 2351), tri - (PDs 2335, 2338, 1952, 2410, and 3428), tetra- (PDs 824 and 2332), and pentacarbocyanine (PDs 1659 and 2438). The linear absorption spectra for all dyes in ethanol are presented in Figure 1.5, which were recorded with a Varian Cary 500 spectrophotometer.

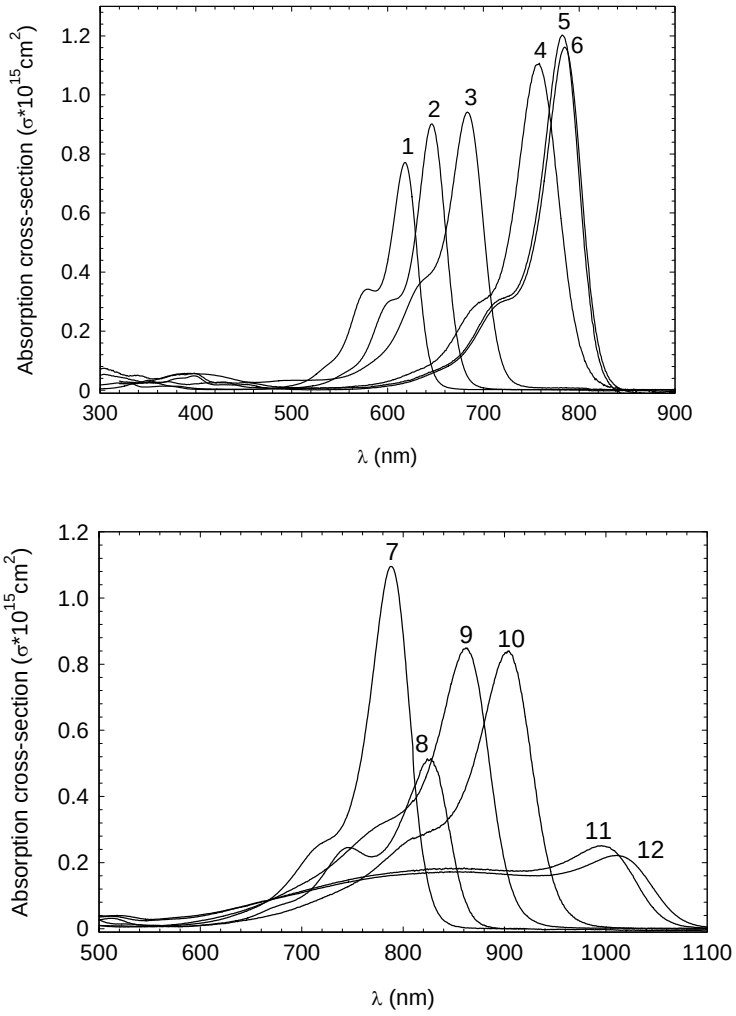

Figure 1.5: Linear absorption spectrum in ethanol, 1) PD 2351, 2) PD 2350, 3) PD 2410, 4) PD 3428, 5) PD 2335 6) PD 2338, 7) PD 1952, 8) PD 2257, 9) PD 824, 10) PD 2332, 11) PD 1659, 12) PD 2398

1.2 Dissertation Statement

This dissertation investigates the excited state nonlinearities in a series of polymethine dyes, shown in Figure 1.4, for the application of nanosecond optical limiting. The major

constraint of polymethine dyes as applied to optical limiting is a saturation of the RSA process at high fluences. Experiments and theoretical modeling are performed to determine the root cause of this saturation effect in both the picosecond and nanosecond regime. The nature of this saturation in the picosecond regime has been revealed and a general energy level structure similar to that shown in Figure 1.1 is used to characterize the process in a polymethine and two other types of organic molecules. Characterization of the excited-state dynamics of polymethine molecules in several host environments has been carried out using a polarization-resolved pump-probe method, and an analysis has been performed to separate excited-state lifetimes from orientational diffusion times. Also, in the process of performing this study a new method was developed for determining the spectral position and orientation of the transition dipole moments that can be applied to at least polymethine molecules, and probably all types of organic molecules. The ultimate goal of these experiments is the development of relationships between molecular parameters and overall nonlinear absorption performance. Several different solvents are used as host environments to investigate how hydrogen bonding, polarity, dielectric friction, slip and stick boundary conditions, and viscosity affect the excited state properties. Along with the quantum chemical modeling performed at the Institute of Physics and National Academy of Sciences of Ukraine, this work has resulted in the synthesis of dyes that have improved photochemical stability with larger nonlinearities which is useful for not only optical limiting but also a wide variety of nonlinear optical applications.

1.3 Dissertation Outline

This dissertation is organized as follows. Chapter 1 gives an introduction to the type of optical nonlinearity being studied and an overview of the materials investigated in this dissertation. Chapter 2 describes a theoretical and experimental study of the absorption of picosecond laser pulses in organic materials that exhibit RSA modeled with a four-level energy manifold. The initial investigation into the excited-state dynamics of polymethine molecules is covered in chapter 3 and describes how lifetimes and rotational motions of the polymethine molecules in different host environments can be measured using a polarization-resolved pump-probe technique. Chapter 4 introduces a new experimental technique developed over the course of this dissertation to measure the spectral position and orientation of the transition dipole moments of polymethine molecules. The effect of symmetry breaking in long chain polymethine molecules is investigated in chapter 5. The work presented in chapter 6 addresses the saturation process in the nanosecond regime as well as developing relationships between conjugation length and absolute excited-state cross sections in a large sampling of host environments. Chapter 7 draws conclusions and suggestions for future work based on the entirety of the dissertation.

CHAPTER 2: PICOSECOND OPTICAL LIMITNG IN REVERSE SATURABLE ABSORBERS: A THEORETICAL AND EXPERIMENTAL STUDY

2.1 Introduction

In this work we theoretically and experimentally study absorption of picosecond laser pulses in materials that exhibit reverse saturable absorption (RSA) modeled with a four-level system. Using an approximate solution to the rate equations we derive, analyze, and verify, numerically and experimentally, a single dynamical equation for the spatial evolution of the pulse fluence that includes both the rate equations and the propagation equation. This analytical approach considerably simplifies the study of optical limiting with picosecond pulses and helps to predict behavior of the nonlinear transmittance, the level of output signal clamping, and a possible transition from RSA to SA that restricts the performance of optical limiters based on RSA.

The absorption of an intense laser pulse through a RSA material depends on the time-dependent population densities of the ground and excited states which, in turn, depend on the parameters of the nonlinear medium and the laser pulse characteristics. The population dynamics would in general be modeled with the five-level system shown in Figure 1.2. But under picosecond pulse excitation the triplet states ($T_{1,2}$) can be neglected because the intersystem crossing time (τ_{13}) is typically long (> 1 ns) compared to the pulse width (τ_p) (~10's of ps). The three-level system (Figure 1.1) models RSA in the picosecond regime, but often fails to match data taken at very high input fluences. The addition of a higher lying fourth level [29,30,31] allows for a better match with data for many materials. As was discussed in Chapter 1 the numbering of the energy levels in the model do not correspond to the real levels of the molecule.

The S_2 to S_3 transition represents a conglomerate of all possible transitions that originate from an excited-state higher than S_1. The four-level model we use is shown in Figure 2.1.

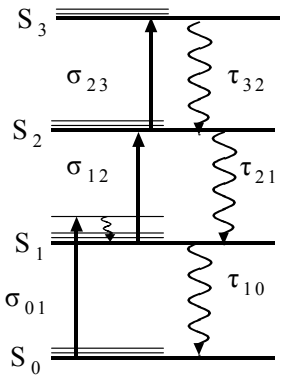

Figure 2.1: Schematic diagram of the four-level model of RSA with picosecond pulse illumination; S_0 is the ground state, S_1, S_2, and S_3 are excited singlet states.

The population dynamics are described by the multi-level rate equations [9,13, 29,30,31,32,33] and are discussed in Section 2.3. A general analytical solution to the system of rate and propagation equations represents a difficult problem. Thus, the solution is usually obtained numerically for a particular set of parameters [30,32,33,34]. However, it is still difficult to gain a basic insight into the properties of the nonlinear absorber due to the number of variables involved in the problem. For example, to determine the dependence of the sample transmittance on the input fluence with all other parameters fixed, one has to perform a full integration of the rate equations and the propagation equation for each value of the input fluence. To study the effects of any other parameter (e.g., pulse shape, width, lifetimes, absorption cross-sections,

sample thickness, etc.) the entire set of calculations has to be repeated. Even with contemporary computing capabilities this task is very time-consuming.

Alternatively, an assumption of the so-called fast absorbers [9] (where the pulse length is much longer than the lifetime of each excited state) allows for an analytical solution of the problem. Mathematically, this means that the differential rate equations reduce to a set of algebraic equations that can be easily solved [31,32,33,34]. However, this steady-state, or stationary, solution is not always applicable because it assumes long pulses so that a triplet excited state has to be taken into account for many materials [9,13, 32,33,34,35,36,37,38,39].

Unlike the steady-state approach, which had been studied previously [30,31,32,33], here we perform a dynamical analysis and show that the stationary solution to the rate equations only gives a very rough estimate for the absorption of short pulses. We show that the behavior of the limiting curve can be accurately predicted based on the solution of a single ordinary differential equation (ODE). The analytical results will allow us to understand the impact of each individual parameter on the absorptive properties of the material and accurately predict various phenomena, as, e.g., turnover from RSA to SA [30,31,32,33].

This chapter is organized as follows. Section 2.2 covers the experimental methods which include a description of the laser system and the optical limiting setup. In Section 2.3 we introduce the rate equations and useful normalizations. In Section 2.4 we solve the rate equations for a rectangular (flat-top) input pulse. This solution is then used to study the optical limiting properties of several materials. Particular emphasis is given to the effect of the turnover from RSA to SA and to the comparison of the dynamical solution with predictions of the steady-state analysis. In Section 2.5 experimental verification of the theoretical analysis is presented for two

organic dyes; a carbocyanine dye 1,1',3,3,3',3'-hexamethylindotricarbocyanine iodide (HITCI) [29,30] and a polymethine dye 2-[2-[3-[(1,3-dihydro-3,3-dimethyl-1-phenyl-2H-indol-2-ylidene)ethylidene]-2-phenyl-1-cyclohexen-1-yl]ethenyl]-3,3-dimethyl-1-phenylindolium perchlorate (PD3) [24,40]. Also in this section the results are discussed for chloroaluminum phthalocyanine (CAP) [36] in which the proposed model fails to adequately describe the limiting curve. Section 2.6 concludes the chapter.

2.2 Experimental Methods

2.2.1 Quantel Picosecond Laser System

The laser system used for the optical limiting experiments in this chapter is a 10 Hz picosecond active/passive modelocked and Q-switched Neodymium-doped Yttrium Aluminum Garnet (Nd:YAG) laser. The laser produces a 56 nanosecond long train of picosecond pulses separated by 7 ns, which each have a pulsewidth of approximately 40 picoseconds (FWHM). The pulsewidths are measured using standard autocorrelation techniques as discussed in references [41,42]. A single pulse is switched out from this train for use in the experiment. The fundamental (1.064 μm) is frequency doubled to 532 nm using an angle tuned KDP crystal. The 532 nm beam has a pulse width of 25 picoseconds (FWHM). The laser system with an additional amplifier can produce pulses with energies of several hundred microJoules (μJ).

2.2.2 Optical Limiting

A schematic of the optical limiting setup is shown in Figure 2.2. The input energy is varied from 1 nJ up to 10 μJ using the rotatable half-waveplate, which is attached to a stepper motor, and a polarizer. A single cycle of the rotation stage from minimum to maximum spans a factor of 20 in energy; therefore 3 measurements are performed to cover the entire energy range. A beam splitter (BS) placed before the first lens (L1) redirects fifty percent of the energy to a reference detector (D_R) which has its voltage calibrated to the energy in front of the sample. An open aperture Z-scan [43] is performed to determine the location of the focal plane of L1. Once the focal plane is determined the sample is placed there for all the optical limiting experiments. The second lens (L2) is 2 inches in diameter, which is used as a collection lens for the transmitted energy onto the signal detector (D_S). The ratio of these two detectors (D_S/ D_R) gives the transmittance of the sample.

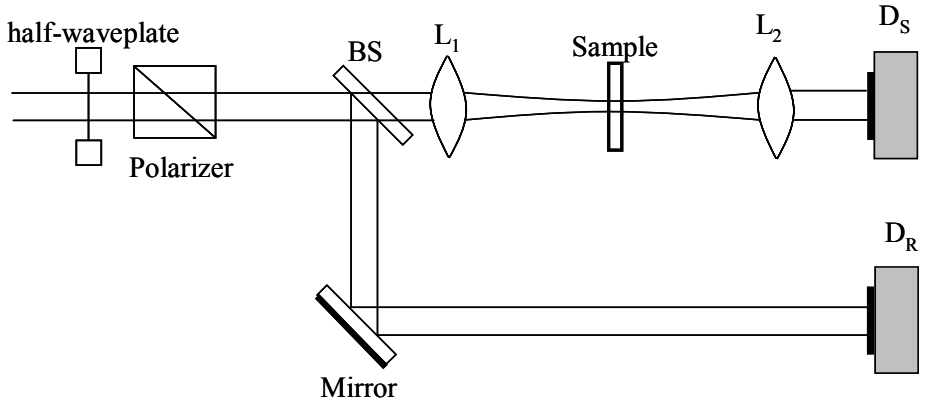

Figure 2.2: Schematic of optical limiting experiment. BS: 50-50 Beam Splitter, L1: 1 inch 15 cm focal length lens, L2: 2 inch 10 cm focal length lens, DS and DR are signal and reference detectors, respectively.

The beam size in the focal plane (beam waist) of the optical limiting setup is important for calculating the fluence and irradiance levels, which are the important beam parameters for nonlinear optical measurements. There are several different methods for measuring the beam waist and three were used in this chapter and throughout this dissertation, each method will be briefly described below. The simplest, but least accurate, method is to measure the size of the beam on a CCD camera at the input to L1 and then to assume the input is a perfect Gaussian beam with waist on L1 and that the lens produces the diffraction limited spot size in the focal plane. This method usually underestimates the size of the beam, which gives the half width $1/e^2$ M (HW$1/e^2$ M) diffraction limited beam waist (ω_0) given by the following equation [44]:

$$\omega_0 = \frac{\lambda f}{\pi W} \tag{1}$$

where λ is the wavelength of light, f is the focal length of the lens, and W is the HW$1/e^2$ M radius of the input beam. The second method is using a knife edge (razor blade) to scan the beam profile perpendicular to the beam propagation direction from one side of focus to the other. This method is quite accurate at measuring the actual beam size in the focal plane and gives information about how close the beam is to being Gaussian by the M^2 parameter [45]. The final method used to determine the size of the beam waist is to perform a closed aperture Z-scan [43] on carbon disulfide (CS_2), which has been thoroughly characterized and has a nonlinear refractive index of $3.1 \bullet 10^{-14} cm^2/W$. From this measurement we look at the distance between the peak and valley of the Z-scan is approximately equal to $1.7Z_0$ [43], where Z_0 is the Rayleigh

range and can be related to the beam waist by $Z_0 = \pi\omega_0^2 / \lambda$. This method is not only useful for checking the beam waist, but also provides a calibration for the irradiance.

2.3 Basic Equations and Normalizations

The model we use to describe RSA is the singlet state four-level structure depicted in Figure 2.1. Since we are interested in picosecond excitation we can ignore the triplet states because the intersystem crossing times are typically much longer (> 1 ns) than the pulsewidth [9]. The effects of the vibronic sublevels are not explicitly accounted for in the rate equations (Eq. 2) due to the fact that the have sub-picosecond relaxation times, however we are implicitly taking them into consideration so stimulated emission processes can be neglected. In addition the lifetime τ_{32} is assumed to be much less then the pulsewidth resulting in negligible population in level 3. As a result, the rate equations can be written as follows [30, 31]

$$\begin{aligned}
\frac{\partial N_0}{\partial t} &= -\frac{\sigma_{01} I}{\hbar\omega} N_0 + \frac{N_1}{\tau_{10}}, \\
\frac{\partial N_1}{\partial t} &= \frac{\sigma_{01} I}{\hbar\omega} N_0 - \frac{N_1}{\tau_{10}} - \frac{\sigma_{12} I}{\hbar\omega} N_1 + \frac{N_2}{\tau_{21}}, \\
\frac{\partial N_2}{\partial t} &= \frac{\sigma_{12} I}{\hbar\omega} N_1 - \frac{N_2}{\tau_{21}},
\end{aligned} \tag{2}$$

where $N_{0,1,2}$ are the respective level population densities that are functions of the time t and the propagation distance z; $N_0 + N_1 + N_2 = N$, $I(z,t)$ is the irradiance of the incident pulse, $\sigma_{j\,j+1}$ and $\tau_{j+1\,j}$ are the corresponding absorption cross-sections and lifetimes, respectively (Figure 2.1). The population densities determine the spatial pulse evolution via the propagation equation [9,30,31,32,33,34]:

$$\frac{\partial I}{\partial z} = -I\left[\sigma_{01}N_0 + \sigma_{12}N_1 + \sigma_{23}N_2\right]. \tag{3}$$

It is easier to deal with the above set of equations both numerically and analytically if we recast them into a dimensionless form. First we represent the input irradiance as $I(0,t) = I_0 f(t)$ where I_0 is the peak irradiance and $f(t)$ is a dimensionless function with unit amplitude that reflects the temporal shape of the pulse (e.g., flat-top, Gaussian, hyperbolic secant, etc.). Next we introduce a dimensionless variable that is proportional to the total fluence of the pulse $A = \sigma_{01} I_0 \tau_p / \hbar\omega$ and scale time by the pulse width τ_p, i.e., $T = t/\tau_p$. We also introduce absorption cross-section ratios $\alpha = \sigma_{12}/\sigma_{01}$ and $\beta = \sigma_{23}/\sigma_{01}$ and dimensionless ratios $T_{10} = \tau_p/\tau_{10}$, $T_{21} = \tau_p/\tau_{21}$. Finally, we normalize the level population densities by the total population, $n_j = N_j/N$, where j goes from 0 to 2. Substituting the above definitions into the rate equations (eqn. 1), we arrive at the following set of dimensionless rate equations:

$$\begin{aligned}
\frac{\partial n_0}{\partial T} &= -\Phi n_0 + T_{10} n_1, \\
\frac{\partial n_1}{\partial T} &= \Phi n_0 - \left[\alpha\,\Phi + T_{10}\right] n_1 + T_{21} n_2, \\
\frac{\partial n_2}{\partial T} &= \alpha \Phi n_1 - T_{21} n_2,
\end{aligned} \tag{4}$$

where $\Phi = A f(T)$. Further, we define a normalized variable that represents linear absorption $Z = \sigma_{01} N z$ [39], and express the propagation equation as

$$\frac{\partial \Phi}{\partial Z} = -\Phi\left[n_0 + \alpha n_1 + \beta n_2\right]. \tag{5}$$

In section 2.4 we approximately solve the system of partial differential equations (PDEs) given by Eqs. (4) and (5) and verify the results by direct numerical integration.

2.4 Solution to the Rate Equations and Nonlinear Absorption of the Material

To analytically solve the system of Eqs. (4) and (5) we follow the reasoning of Refs. [9,34,37,38] and treat the rate and propagation equations separately. The rate equations can be solved assuming constant irradiances and their solution substituted into the propagation Eq. (4). Subsequent integration of both sides of the propagation equation with respect to time will result in the spatial evolution equation for the pulse fluence $F = \int_{-\infty}^{+\infty} \Phi dT$ [34,37,38].

It can be expected that, as in the five-level model used for describing the propagation of nanosecond pulses in RSA materials [9], the functional dependence of the population dynamics on the input fluence does not depend strongly on the pulse shape if the medium is excited by short pulses [39]. Below we will show that the flat-top pulse approximation $I(t) = I_0,\ 0 < t < \tau_p$ [9,37,38] provides a reasonably accurate description of the propagation of realistic laser pulses in many RSA materials, while greatly simplifying the analysis. For the normalized units used in this work the pulse shape results in $f(T) \equiv 1,\ 0 < T < 1$ and Eqs. (4) become a system of ODEs with constant coefficients that are easily solvable.

The standard procedure consists in equating the corresponding determinant of Eqs. (4) to zero in order to find the eigenvalues. Since the order of the system (Eqs. 4) equals 3, we obtain a third-order polynomial whose roots can be found explicitly. One of the roots is equal to zero, while the other two are

$$\lambda_{\pm} = \tfrac{1}{2}[-(\alpha + \varepsilon + q + 1) \pm \sqrt{D}] < 0, \tag{6}$$

where we have denoted

$$D = \alpha^2 + 2\alpha(q-1+\varepsilon) + (q-1-\varepsilon)^2 \tag{7}$$

and $\varepsilon = T_{10}/A$, $q = T_{21}/A$.

With eigenvalues known, one can easily find the corresponding eigenvectors, and using the initial conditions for the medium before excitation $n_0 = 1$, $n_1 = 0$, $n_2 = 0$, obtain the solution to system (4) as

$$\begin{pmatrix} n_0 \\ n_1 \\ n_2 \end{pmatrix} = C \begin{pmatrix} q & -\dfrac{(\lambda_- + q)\lambda_+}{\sqrt{D}(\lambda_- + 1)} & \dfrac{(\lambda_+ + q)\lambda_-}{\sqrt{D}(\lambda_+ + 1)} \\ \dfrac{q}{\varepsilon} & -\dfrac{(\lambda_- + q)\lambda_+}{\sqrt{D}\varepsilon} & \dfrac{(\lambda_+ + q)\lambda_-}{\sqrt{D}\varepsilon} \\ \dfrac{\alpha}{\varepsilon} & -\dfrac{\alpha\lambda_+}{\sqrt{D}\varepsilon} & \dfrac{\alpha\lambda_-}{\sqrt{D}\varepsilon} \end{pmatrix} \begin{pmatrix} 1 \\ \exp(\lambda_- AT) \\ \exp(\lambda_+ AT) \end{pmatrix}, \tag{8}$$

where

$$C = \frac{(\lambda_+ + 1)(\lambda_- + 1)}{\lambda_+ \lambda_- (q-1)}. \tag{9}$$

It is important to note that the solution remains continuous with $T_{21} = A$, i.e. $q = 1$ because both the numerator and denominator in (9) approach zero. In the limit $q = 1$ Eq. (8) simplifies to

$$\begin{pmatrix} n_0 \\ n_1 \\ n_2 \end{pmatrix} = \begin{pmatrix} \dfrac{\varepsilon}{\alpha+\varepsilon+1} & \dfrac{\varepsilon}{(\alpha+\varepsilon+1)(\alpha+\varepsilon)} & \dfrac{\alpha}{\alpha+\varepsilon} \\ \dfrac{1}{\alpha+\varepsilon+1} & -\dfrac{1}{\alpha+\varepsilon+1} & 0 \\ \dfrac{\alpha}{\alpha+\varepsilon+1} & \dfrac{\alpha}{(\alpha+\varepsilon+1)(\alpha+\varepsilon)} & -\dfrac{\alpha}{\alpha+\varepsilon} \end{pmatrix} \begin{pmatrix} 1 \\ \exp(-[\alpha+\varepsilon+1]AT) \\ \exp(-AT) \end{pmatrix}.$$

To study the spatial evolution of the pulse, the solution (8) has to be substituted into the propagation equation (Eq. 5). The resulting equation is too cumbersome to work with analytically. However, we can significantly simplify the exact solution to the rate equations (Eqs. 8) without any substantial reduction in accuracy by examining typical RSA material parameters.

For a typical RSA material the lifetime of the first excited state (τ_{10}) is on the order of a nanosecond, while τ_{21} is several picoseconds [24,29,30]. This means that the parameter $\varepsilon < 10^{-2}$ is small compared to both q and α ($\alpha > 1$ for RSA materials). Hence we can make a series expansion with respect to ε and write (6), (7), and (9) as

$$\lambda_+ \approx -1 + \varepsilon \frac{1-q}{\alpha + q - 1},$$

$$\lambda_- \approx -\alpha - q - \varepsilon \frac{\alpha}{\alpha + q - 1}, \tag{10}$$

$$\sqrt{D} \approx \alpha + q - 1 + \varepsilon \frac{\alpha - q + 1}{\alpha + q - 1}, \tag{11}$$

$$C \approx \frac{\varepsilon}{\alpha + q}, \tag{12}$$

respectively. Substituting Eqs. (10)-(12) into the simplified version of Eq. (8) results in the approximate solution to the rate equations. Furthermore, we take advantage of the fact that the solution found for the population densities has two very different characteristic times, which are proportional to the eigenvalues λ_+ and λ_-. As can be recognized from Eq. (9), $|\lambda_-| >> |\lambda_+|$, so it is possible to neglect the transient processes that vary as $\sim \exp(\lambda_- AT)$. As a result, the approximate solution for the population densities can be expressed in the form

$$n_0(T) \approx \exp(-AT), \tag{13}$$

$$n_1(T) \approx \frac{q}{\alpha + q} + \frac{1-q}{\alpha + q - 1} \exp(-AT), \tag{14}$$

$$n_2(T) \approx \frac{\alpha}{\alpha + q} - \frac{\alpha}{\alpha + q - 1} \exp(-AT). \tag{15}$$

To check the accuracy of the approximate solutions to the rate equations we compare (13)-(15) with the exact solutions Eqs. (7). The results are shown in Figure 2.3 for two RSA materials - HITCI and PD3. It can be clearly seen from Figure 2.3 that formulas (13)-(15) accurately describe the population dynamics. The slight initial deviation for n_1 and n_2 is due to the discarded terms proportional to $\sim \exp(\lambda\_AT)$. This small deviation will not have a significant effect on the propagation equation because the excited state populations (n_1 and n_2) are small for $T < 0.05$.

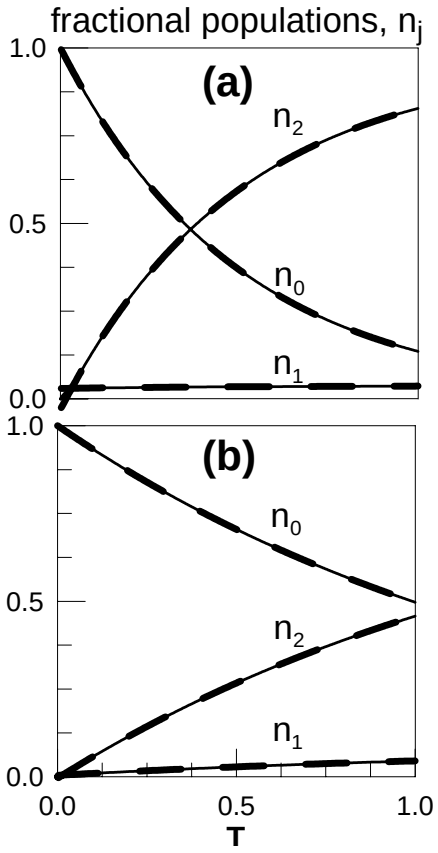

Figure 2.3: Population dynamics of two RSA materials excited by a temporal flat-top pulse with a pulse width of τ_p = 25 ps (FWHM). The results are obtained using the exact analytical solution to the rate equations (8) (solid lines) and the approximate analytical solution (13)-(15) (dashed lines). The parameters are (a) HITCI: A = 2, α = 32, β = 0.1, τ_{10} = 1.7 ns, τ_{21} = 10 ps; (b) PD3: A = 0.7, α = 200, β = 2, τ_{10} = 1 ns, τ_{21} = 1.9 ps. Each material has a linear transmittance of .905 (Z = 0.1).

To validate the use of a flat-top pulse we examine the propagation of a pulse through the two RSA materials shown in Figure 2.3 and compare the output fluence as a function of propagation distance for the flat-top and Gaussian pulse shapes. From Figure 2.4 we can conclude that attenuation of the total fluence F is nearly the same for both the flat-top and

Gaussian pulses. Thus, using a flat-top shape in solving the rate equations is appropriate, and accurately predicts the transmitted fluence of the corresponding short pulses.

Integrating Eq. (5) with Eqns. (13)-(15) we obtain the propagation equation for the normalized fluence

$$\frac{dF}{dZ} = \left[\alpha \frac{(\beta - \alpha)F}{(\alpha - 1)F + T_{21}} + \alpha - 1 \right] \left(1 - e^{-F}\right) - \alpha \left[1 + \frac{(\beta - \alpha)F}{\alpha F + T_{21}} \right] F = -\sigma_{eff}(F)\, F\,, \qquad (16)$$

where $F = \int_{-\infty}^{+\infty} \Phi dT$ and $\sigma_{eff}(F) = \frac{1}{F}\int_{0}^{F} (n_0 + \alpha\ n_1 + \beta\ n_2) dF$ is the effective fluence cross-section [34,39]. It is important to note that this single differential equation now includes both the set of rate equations and the propagation equation. Equation (16) cannot be solved analytically, but its numerical solution represents a much easier task compared to the solution of the full system (4), (5) for every value of input fluence. The results of numerical integration of Eq. (16) are shown in Figure 2.4 by the solid curves.

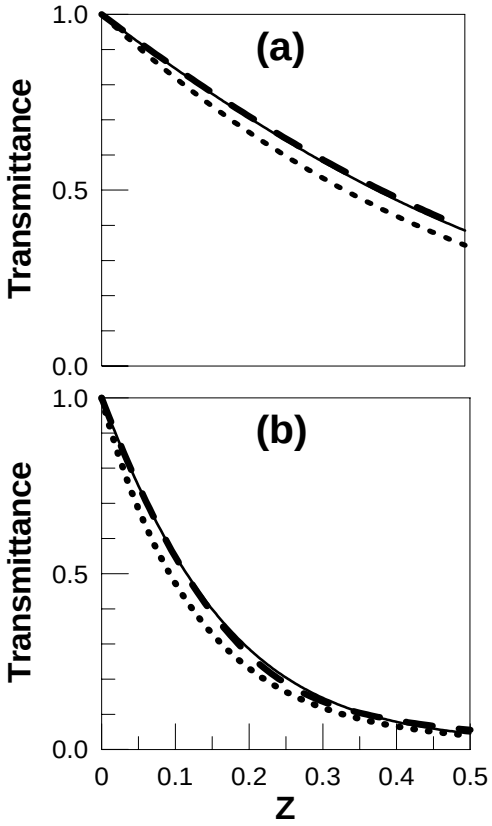

Figure 2.4: Transmittance (F_{out} / F_{in}) as a function of normalized propagation distance $Z = \sigma_{01} N\ z$ for the dyes in Figure 2.3: (a) HITCI, (b) PD3. The dotted and dashed lines represent the numerical solution to Eqs.. (4) and (5) for a Gaussian and flat-top pulse shape, respectively. The solid line is the numerical solution to the ODE (16).

We also computed limiting curves (transmittance vs. input fluence) for HITCI and PD3 as shown in Figure 2.5. We compared the numerical solution to Eq. (16) to the full set of rate and propagation Eqs. (4) and (5) for a flat-top and Gaussian input pulse. The solution to Eq. (16) almost coincides with the numerical solution to the original system with the flat-top input and it

is also close to the numerical solution for a corresponding (equal total fluence and peak irradiance, ratio of pulsewidths: 0.56) Gaussian pulse (Figure 2.5).

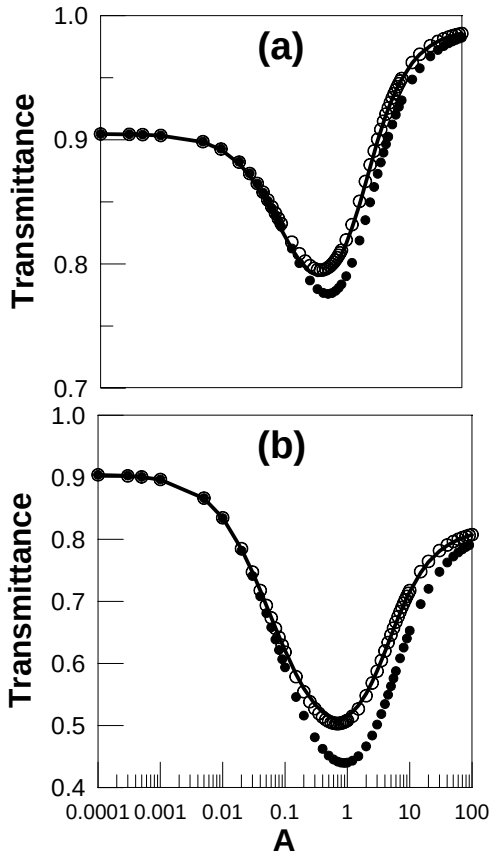

Figure 2.5: Transmittance (F_{out} / F_{in}) as a function of normalized input fluence for the dyes in Figure 2.3; (a) HITCI, (b) PD3. The solid line is a limiting curve calculated using the numerical solution to the ODE Eq. (16). The empty and filled circles are limiting curves calculated from the full system of PDEs (4) and (5) for the flat-top and Gaussian pulses, respectively

The important feature to notice in the limiting curves is the effect of turnover from RSA to SA [30,31]. As can be seen from Figure 2.5 the turnover predicted by Eq. (16) occurs at

slightly lower fluences than that given by the numerical solution to the original system (4) and (5) for a Gaussian pulse. Thus, our solution predicts a lower limit of the input fluence for when this turnover occurs for a more realistic pulse shape. An approximate condition for the turnover point (F_{to}) in terms of the material parameters can be obtained as a solution to $d\sigma_{eff}(F)/dF = 0$ [31]. This criterion provides good accuracy only for low linear losses (less than 10%) and can be expressed in terms of the transcendental equation

$$\begin{aligned}&\alpha(\beta-\alpha)T_{21}F^2(\alpha F - F + T_{21})^2 + T_{21}F(\alpha F + T_{21})^2(1-e^{-F})(\alpha^2-\alpha\beta)\\&+((F+1)e^{-F}-1)(\alpha F - F + T_{21})(\alpha F + T_{21})^2((2\alpha-\alpha\beta-1)F-(\alpha-1)T_{21}) = 0\,,\end{aligned} \tag{17}$$

whose numerical solution F_{to} gives the turnover fluence.

To complete our analysis, we compare our results with those obtained previously [30, 31] that exploit the steady-state solution to the rate equations (4). Using the normalization procedure from Section 2.3 we arrive at the following propagation equation obtained using the stationary population densities [31]

$$\frac{d\widetilde{A}}{dZ} = \frac{-\widetilde{A}(V + \alpha\widetilde{A} + \beta\alpha\widetilde{A}^2)}{V + \widetilde{A} + \alpha\widetilde{A}^2} \tag{18}$$

where $\widetilde{A} = \dfrac{\sigma_{01}I_0\tau_{21}}{\hbar\omega} = \dfrac{A}{T_{21}}$ and $V = \dfrac{\tau_{21}}{\tau_{10}}$. In Figure 2.6 we have plotted the limiting curve for HITCI calculated from the dynamical propagation Eq. (16) and from the steady-state Eq. (18). It is clear that the latter predicts much stronger limiting and an even earlier turnover from RSA to SA than that predicted by the dynamical model Eq. (16). As can be inferred from Figure 2.6 the shape of the limiting curve predicted by the steady-state model strongly differs from the results of the dynamical analysis. It can be expected that the steady-state model predicts a much lower

transmittance at higher input fluences, but what is surprising is the value of the fluence at the minimum in transmittance (the turnover point) is in most cases an order of magnitude less than that given by the dynamical model.

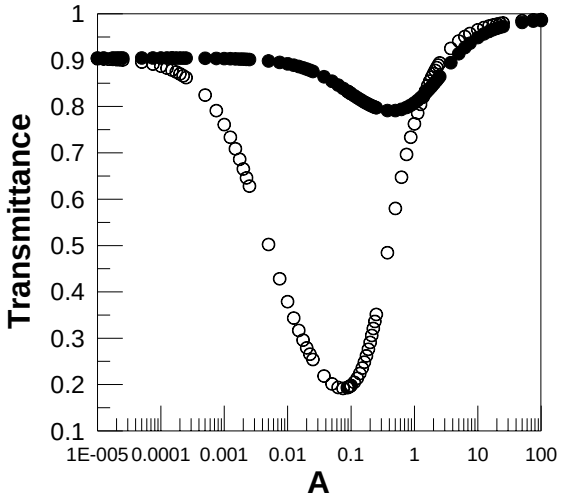

Figure 2.6: Limiting curves calculated for HITCI using the numerical solution to Eq. (16) derived from the dynamical solution to the rate equations (filled circles) and using the numerical solution to Eq. (18) derived from the steady-state solution to the rate equations (empty circles). Pulse width (FWHM) is 25 ps.

2.5 Experimental Results and Discussion

In the previous sections of this chapter we used the materials HITCI and PD3 to compare the theoretical and numerical results. We experimentally studied these two materials along with the phthalocyanine dye chloro-aluminum phthalocyanine (CAP). With the exception of HITCI [29] we could not find any references to measured values of the second excited state cross-section σ_{23}. Therefore, we performed the experiment on HITCI to compare to previous results [29, 30] and on PD3 and CAP to determine σ_{23} from fitting the experimentally measured

limiting curve. Also, the experimentally determined value of the fluence at the turnover point can be compared to that predicted by the dynamical and steady-state solutions. It will be seen that HITCI and PD3 fit our model quite well, but CAP does not.

The results of the optical limiting experiments for HITCI and PD3 are shown in Figure 2.7a and 2.7b, respectively. The experimental results are plotted along with the limiting curves produced by the numerical solution of Eqs. (4) and (5) for a Gaussian pulse and the solution to the ODE (16). The best fit parameters for HITCI ($\sigma_{01} = 2.5\cdot10^{-17}$ cm^2, $\sigma_{12} = 87.5\cdot10^{-17}$ cm^2, $\sigma_{23} = 1.5\cdot10^{-17}$ cm^2, $\tau_{10} = 1.7\cdot10^{-9}$, $\tau_{21} = 2.2\cdot10^{-12}$, $Z = 0.091$) and PD3 ($\sigma_{01} = 1.03\cdot10^{-18}$ cm^2, $\sigma_{12} = 2.21\cdot10^{-16}$ cm^2, $\sigma_{23} = 5.2\cdot10^{-20}$ cm^2, $\tau_{10} = 1.0\cdot10^{-9}$, $\tau_{21} = 6.0\cdot10^{-12}$, $Z = 0.089$) are in good agreement with previously reported results [30] (HITCI) and [24,40] (PD3). We then determined the fluence at the turnover point from Figure 2.7a and 2.7b for the experiment and the two fitting curves. We also calculated the fluence at the turnover point using the transcendental Eq. (17) and the numerical solution to the steady-state propagation Eq. (18). The values for the fluence at the turnover point for both HITCI and PD3 obtained with all the methods described above are listed in Table 2.1. As can be seen from Figure 2.7 and Table 2.1 all the predictions for the fluence at the turnover point are lower than the experimental results. It has been shown (HITCI [29,30] and PD3 [24,40]) that to explain nonlinear absorption in these materials a more detailed model structure needs to be used. For HITCI, Hughes et. al. [30] and Swatton et. al. [29] have shown that their experimental data could be fit accurately if they accounted for a finite intraband vibrational lifetime. As for PD3, Lim et. al. [24, 40] showed that an all singlet state five-level model, which includes reorientational processes in the first excited state, would accurately fit their experimental data. Even neglecting these details our dynamical solution approximately

predicts the fluence at the turnover point to the same order of magnitude. For the material CAP our model could not fit the data (Figure 2.8) and therefore does not make accurate predictions of the fluence at the turnover point. Wei et. al. [6] had to invoke both two-photon absorption (2PA) and excited state absorption to accurately fit their data. So in this case the 2PA is large enough that it can't be neglected.

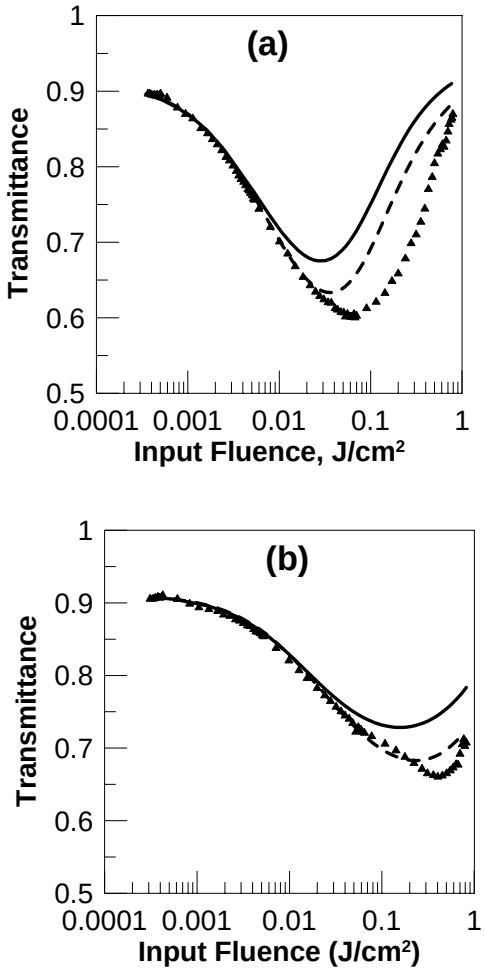

Figure 2.7: Experimentally measured limiting curve (triangles) for (a) HITCI and (b) PD3 with the best fit material parameters used in the numerical solution to Eq. (16) (solid line) and the full system of PDE. (4) and (5) for a Gaussian pulse (dashed line).

Table 2.1 Turnover Fluence (mJ/cm^2) Determined from Experimental and Numerical Results

Material	Eq. (18)	Eq. (17)	Eq. (16)	Eqns. (4), (5) Gaussian Input	Experiment
HITCI	3	13	27	36	84
PD3	55	76	155	232	414

Below we briefly explain how the material parameters affect the behavior of the limiting curve. First, we consider the normalized time parameters T_{21} and T_{10}. As T_{21} becomes larger (longer pulses or shorter lifetime of the second excited state) the limiting curve becomes deeper and the turnover from RSA to SA shifts to higher fluences. On the other hand, a change in T_{10} of up to an order of magnitude barely affects the nonlinear absorption of the material. As for the excited state cross section parameters α and β, a larger α (larger first excited state cross-section or smaller ground state cross-section) produces a deeper limiting curve, but the turnover from RSA to SA does not shift to higher fluences as was seen with an increase in T_{21}. Parameter β is the most sensitive material parameter for determining when the turnover from RSA to SA will occur. As β increases the limiting curve becomes slightly deeper and the turnover point shifts to higher input fluences. It is important to note that all these tendencies rely on the assumption of sufficient linear absorption to populate the first excited level.

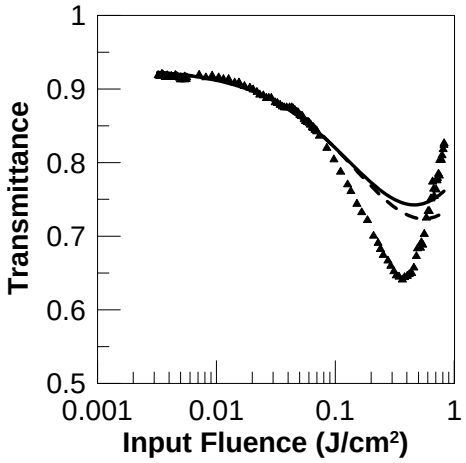

Figure 2.8: Experimentally measured limiting curve (triangles) for CAP with best fit material parameters used in the numerical solution to Eq. (16) (solid line) and the full system of PDE Eqs. (4) and (5) for a Gaussian pulse (dashed line).

Our theoretical results can also be used to analyze the output fluence at high input fluence levels (F>>1). In this case, an exponential term in Eq. (16) can be dropped and the asymptotic behavior of the output fluence can be obtained from the condition

$$u(F_{out}) \approx u(F_{in}) \exp\left[-\alpha(\beta + T_{21})Z\right], \tag{19}$$

where

$$u(F) = (F-1)^{T_{21}+\alpha}\left[F + \frac{T_{21}}{\beta}\right]^{T_{21}(\alpha-\beta)/\beta}. \tag{20}$$

For instance, the output becomes clamped at the maximum allowable energy, e.g., 1μJ can be achieved for 25 ps pulses using a polymethine dye [24,40] with 80% linear transmittance and $\alpha = \sigma_{12}/\sigma_{01} = 50$ if $\beta = \sigma_{23}/\sigma_{01} > \beta_{cr} \approx 28$.

An important conclusion to make is that for high input energies with sufficient linear absorption the key parameter that influences optical limiting is the ratio of the second excited state absorption cross-section to the ground state absorption cross-section. In the above example the output energy is merely changed with the increase in α from 50 to 200. Therefore, from the viewpoint of efficient picosecond optical limiting, there is no advantage in having a very large first excited state absorption cross-section with a small second excited state absorption cross-section because the latter will act as a bottleneck to the optical limiting process. Recently synthesized polymethine dyes that have a very large first excited state absorption cross-section are quite poor optical limiters in the picosecond regime because of a low value of β. This consideration needs to be taken into account when synthesizing new materials for picosecond optical limiting. The qualitative basis for practical estimates can be gained from Eq. (19).

2.6 Conclusion

In the picosecond regime the steady-state solution to the rate equations does not always provide a reasonably accurate description of the nonlinear absorption in RSA materials, whereas numerical treatment of the full system of PDEs remains time-consuming. We have developed an approach that accounts for the dynamical behavior of the population densities and optical propagation, but only requires numerical solution of a single ODE. We have shown that the specific pulse shape has little effect on the nonlinear absorption of the pulse so that a flat-top pulse shape can be used that greatly simplifies and expedites modeling of beam propagation through RSA materials with picosecond pulses. We have obtained an approximate criterion for the turnover from RSA to SA to rapidly calculate the turnover point from the photophysical

properties of the material. The dynamical equation for fluence allows us to determine the critical values of material parameters to achieve the output energy clamping at the desired level. This approach can be straightforwardly extended to the case of arbitrary initial conditions to study the absorption properties of the material by double pump-probe measurements [46,47]. Additionally, the results of picosecond optical limiting experiments can be used to determine material parameters that in turn can then be used to predict the outcome of nanosecond optical limiting.

CHAPTER 3: EXCITED-STATE ABSORPTION DYNAMICS IN POLYMETHINE MOLECULES DETECTED BY POLARIZATION-RESOLVED PUMP-PROBE METHODS

3.1 Introduction

Polarization-resolved excitation-probe measurements are performed for a subset of the dyes (PD2350, PD2351, PD2335, PD2338, PD824, PD2332, and PD2257) shown in Figure 1.4 in three solvents (ethanol, ethylene glycol, and methylene chloride) and a polyurethane acrylate elastopolymer (PUA). In work by Negres et. al. [48] the prediction and observation of two additional ESA bands in the near infrared region was reported, also in this work the transition modeling based on a study of the steady-state fluorescence excitation anisotropy and quantum-chemical calculations was proposed. Analyzing the theoretical predictions and experimental data it was concluded that the most intense ESA broadband spectrum in the visible is connected with the $S_1 \rightarrow S_5$ transition. It should be noted at this time that under current quantum-chemical theories the $S_1 \rightarrow S_5$ transition would be forbidden. This issue is discussed in Section 3.4. Two other bands are connected with the much less intense $S_1 \rightarrow S_2$ and $S_1 \rightarrow S_4$ allowed transitions. The $S_1 \rightarrow S_3$ transition is forbidden and was not observed experimentally. The orientation of the dipole moments for the ESA transitions and their intensities has not been investigated as thoroughly. In references [49,50] the orientations of the transition dipole moment for the ESA band in oxazine dyes (Acridine Orange, Nile Blue & Cresyl Violet) and Rhodamine 6G were measured with a picosecond pump-probe technique. In all cases the ESA ($S_1 \rightarrow S_n$) and ground-state absorption ($S_0 \rightarrow S_1$) transition dipole moments were found to be parallel. These measurements and their analysis for PDs had yet to be performed prior to this work.

In the pump-probe experiments, we observe a strong angular dependence of the RSA decay kinetics upon variation of the angle between the pump and probe polarizations. This is known as anisotropy. The difference in absorption anisotropy kinetics in the solvents and PUA is detected and analyzed. We describe our experimental studies and give an analysis of the nature of the rotational motions of excited molecules and the orientation of the excited-state transition dipole moments relative to transition dipole moments from the ground state. Picosecond pump-probe methods have been extensively used to measure ground or excited-state decay kinetics for solutions of many organic molecules since the 1970-80s. In the series of articles by Lessing and Von Jena [51,52,53] it was shown both theoretically and experimentally that transient absorption measurements yield kinetics of both electronic level decay and rotational relaxations. It will be shown in this chapter how these quantities can be separated using the pump-probe measurements.

Thus, in this chapter, we describe experimental studies and give the analysis for the subset of PD molecules that aid in the understanding of the:

(1) Nature of the rotational motions of excited molecules in several host materials.

(2) Orientation of the ESA transition dipole moments between the $S_0 \rightarrow S_n$ (n = 1, 2, 3 …) levels and the fluorescence emission dipole moment for the $S_1 \rightarrow S_0$ transition.

(3) Orientation of the ESA transition dipole moments between the $S_0 \rightarrow S_n$ (n = 1, 2, 3 …) levels and the excited state transition dipole moments for the $S_1 \rightarrow S_n$ (n = 2, 3, 4 …) transitions.

The experimental techniques used to investigate the PD molecules are:

(1) Linear absorption spectral measurements.

(2) Steady-state excitation anisotropy measurements.

(3) Picosecond polarization-resolved pump-probe measurements.

(4) Femtosecond polarization-resolved pump-probe measurements.

The analysis includes:

(1) Molecular volume calculations in van der Waals model using the HyperChem software package.

(2) Numerical fitting of the pump-probe measurements.

3.2 Experimental Methods

3.2.1 Steady State Fluorescence Excitation Anisotropy Method

Steady-state fluorescence spectra (using low concentration ~ 10^{-6} M/l liquid dye solutions to avoid reabsorption of the fluorescent light) as well as anisotropy excitation spectra (using high viscosity solvents to avoid reorientation) were obtained with a PTI Quantamaster Spectrofluorimeter. A simplified schematic for the fluorescence measurements is shown in Figure 3.1. Excitation anisotropy measurements give us information about the spectral position and orientation of the transition dipole moments from the ground to first and higher excited states $S_0 \rightarrow S_n$ (n = 1, 2, 3…) relative to the emission dipole moment orientation. The excitation anisotropy spectrum, R_{Fl} (λ), was calculated as a function of the excitation wavelength λ at a fixed emission wavelength (usually near the fluorescence maximum) after appropriate background subtraction on each component. R_{Fl} (λ) is defined as

$$R_{Fl}(\lambda) = \frac{I_{vv}(\lambda) - G(\lambda) I_{vh}(\lambda)}{I_{vv}(\lambda) + 2G(\lambda) I_{vh}(\lambda)}, \tag{21}$$

where $G(\lambda) = \frac{I_{hv}(\lambda)}{I_{hh}(\lambda)}$ and $I_{vv}(\lambda)$, $I_{hv}(\lambda)$, $I_{vh}(\lambda), I_{hh}(\lambda)$ are the polarized fluorescence intensities at the excitation wavelength λ. The first and second subscripts refer to the orientation (*v* for vertical and *h* for horizontal) of the excitation and emission polarizations, respectively [54]. The angle between the absorption and emission transition moments can be determined from the anisotropy by:

$$R_{Fl} = \frac{2}{5}\left(\frac{3Cos^2(\beta_{Fl}) - 1}{2}\right) \tag{22}$$

where β_{Fl} is the angle between the absorption transition moment and the emission transition moment [54]. A derivation of the anisotropy equation based on reference [55] is given in Appendix B. The anisotropy can take on values between 0.4 to -0.2, where the maximum refers to parallel transition moments and the minimum for perpendicular transition moments [54]. The results of the steady-state excitation anisotropy measurements are presented below.

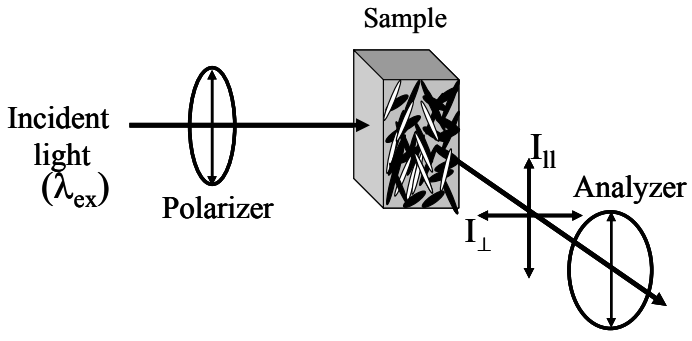

Figure 3.1: Simplified schematic of spectrofluorimeter. As shown polarizer for excitation source and analyzer for emission are in vertical positions (*v*) resulting in the $I_{vv}(\lambda)$ measurement.

3.2.2 Picosecond Polarization-Resolved Pump-Probe Method

As stated in the introduction to this chapter the pump-probe experiment can measure both lifetime decay and reorientational diffusion kinetics. The way to separate these two effects is important not only for the work in this chapter, but for most of the work in this dissertation. So it will be discussed in detail.

In both the solvent and polymeric hosts the molecules are in an isotropic distribution in the ground state. Under excitation of a linearly polarized pump beam the molecules with their transition dipole moments aligned parallel to the pump polarization are most likely to be excited, thus producing an anisotropic distribution in the excited-state (S_1). In the fluorescence experiments discussed in section 3.2.1 this distribution is probed by monitoring the polarized fluorescence intensities. The pump-probe experiment monitors the distribution of the excited-state population by the absorption of a weak probe beam. It has previously been shown by Lessing and Von Jena [51] that the excited-state population density is proportional to the change in the normalized probe transmittance ($\Delta T / T_L$) for relatively small changes (> 30%). Decay kinetics, as measured by probe polarizations parallel and perpendicular to the pump, are biexponential since they include rotational motions as well as decay of the excited state (S_1). Also, the change in transmittance of the probe has been shown in the literature [56] to be given as:

$$\Delta T_{\parallel}(t) = \Delta T_{ma}(0) \cdot Exp(-t/\tau_F) \cdot [1 + 2R_{pp}(0) \cdot Exp(-t/\tau_R)] \tag{23}$$

$$\Delta T_{\perp}(t) = \Delta T_{ma}(0) \cdot Exp(-t/\tau_F) \cdot [1 - R_{pp}(0) \cdot Exp(-t/\tau_R)] \tag{24}$$

where τ_F is the excited state decay time, τ_R is the reorientational diffusion time, and

$\Delta T_{ma}(0)$ and $R_{pp}(0)$ will be defined shortly. The parallel and perpendicular measurements can be used to define an ESA anisotropy, which is monoexponential, just as the fluorescence anisotropy was defined in the previous section. It is given as:

$$R_{pp}(t) = \frac{\Delta T_{\parallel} - \Delta T_{\perp}}{\Delta T_{\parallel} + 2\Delta T_{\perp}} = R_{pp}(0) Exp(-t/\tau_R) \tag{25}$$

where $R_{pp}(0)$ is the anisotropy at zero time delay between the pump and probe and gives us information about the angle between the pump and probe absorption transition dipole moments as:

$$R_{pp} = \frac{2}{5}\left(\frac{3Cos^2(\beta_{pp}) - 1}{2}\right) \tag{26}$$

where β_{pp} is the angle between the pump and probe absorption transition dipole moments. A monoexponential decay rate can be observed directly for a specific angle between the pump and the probe polarization referred to in the literature as the "magic angle" [54]. The term "magic angle" was coined because for the relative polarization between the pump and the probe of 54.7° the probe senses only the lifetime decay of the excited state and is insensitive to orientational diffusion effects. This angle is the 3-dinensional equivalent of 45 degrees in 2 dimensions and comes from the average value of $\cos^2(\theta) = 1/3$. The change in transmittance for a probe beam polarized at the magic angle w.r.t the pump is given as:

$$\Delta T_{ma}(t) = \Delta T_{ma}(0) \cdot Exp(-t/\tau_F) \tag{27}$$

where $\Delta T_{ma}(0)$ is the change in transmittance of the probe at zero time delay between the pump and probe.

Thus, the transient pump-probe anisotropy method can be used to separate the population decay kinetics from the reorientational dynamics. In concentrated dye solutions the anisotropy decay kinetics may be affected by resonance energy transfer among molecules. This effect occurs if the distance, r, between molecules is close to a characteristic distance, the so-called Forster distance, R_0, which is typically equal to 4 nm for these types of molecules [54]. In our experiments the concentration of dyes both in ethanol and PUA does not exceed 10^{-3} M/l. Therefore, the average distance between molecules (r) is at least 12 nm (3 R_0). In this case the energy transfer efficiency, given by $E = R_0^6/(R_0^6 + r^6)$ [54], is less then 0.14%, which is a negligible value.

These measurements were conducted using the same laser described in section 2.2.1. The experimental set-up is shown in Figure 3.2. The pump and probe beams are generated from the same laser (532 nm) and are separated with a beam splitter with the majority of the energy going into the pump beam and only a small percentage (at least 200 times less) going into the probe beam. The energy range of the pump beam was 0.2-7 μJ. The pump and probe beams are focused to waists of radius 100 μm and 18 μm (Half Width $1/e^2$ Maximum), respectively. The pump beam is larger than the probe beam to ensure that the probe beam senses a uniform excitation region in the sample. The pump irradiance was at least an order of magnitude larger than that of the probe (except in the case of PD 2350 where the ratio was 7). The probe beam could be temporally delayed with respect to the pump beam up to 7 nanoseconds, and its irradiance was kept low so as not to induce any nonlinearity in the sample. The pump and the probe beams are overlapped at a small angle (~ 5°) within the sample so the probe beam can be separated after the sample from the pump as shown in Figure 3.2. The polarization of the probe is fixed and a

polarizer placed after the sample is aligned parallel with the probe polarization. The pump polarization is adjusted with a half-wave plate and can be set to any angle with respect to the probe polarization. The probe beam is monitored before and after the sample using large area silicon photodiodes.

In this type of experiment it is very important to know the position of zero delay. This is done by performing a pump-probe experiment using CS_2, which, due to its finite relaxation time and the fact that the laser pulses are slightly chirped, produces a two-beam coupling effect in the sample that allows us to easily determine zero delay [57].

To achieve a time delay of 7 nanoseconds between the pump and the probe an optical delay of 210 centimeters has to be realized. To do this we use a translation stage that has a range of 27 centimeters and align the probe beam to strike each corner cube 4 times resulting in a multiplication factor of 8 in the distance the stage scans. Some alignment tips will be given since the process is fairly difficult:

(1) Align the probe beam and stage to be parallel. To do this take two identical apertures in two identical holders and attach them to the table at the front position of the stage and the back position of the stage a set distance from the edge of the table. Align the probe beam through the two apertures. Next attach the corner cube to the translation stage and set the stage so the probe beam strikes the edge of the corner cube, as shown in the inset of Figure 3.2, and then use a ruler to make sure the stage is parallel to the edge of the table. Remove the corner cube and insert an aperture and make sure the beam goes through the center of the aperture over the entire range of the stage. The stage and probe beam are now aligned.

(2) Inserting the second corner cube. This corner cube should be attached to a three dimensional stage to allow for easy adjustments. The key with this step is to insure the correct height of both the corner cubes. First put the corner cube back in that is attached to the stage, and set the height so that the beam strikes the three faces symmetrically. Next position the second corner cube so the beam strikes the corner cube on the opposite face towards the center, as shown in Figure 3.2. Adjust the height of this corner cube so it again makes a symmetric pattern on the three faces. The horizontal position of the corner must now be adjusted so the beam strikes the corner cube attached to the stage towards the center of the mirror, as shown in Figure 3.2. Both corner cubes should now be aligned correctly.

(3) Inserting the mirror which is at the output of the second (stationary) corner cube. This mirror should be in a holder with three degrees of freedom and a holder which is open on the side of the corner cubes due to the fact that the beam passes very close to the mirror. Use this mirror to align the probe beam back through the corner cubes so it traces the exact same path it took. Once you get this close you should see a back reflection on the first aperture you inserted and center the beam on this aperture. The system should now be aligned.

(4) Check the alignment by scanning the stage the entire range and recording the ratio of the signal to reference detectors. If the stage is properly aligned this ratio should be less than 1 percent. If the error is larger repeat the steps for a mistake.

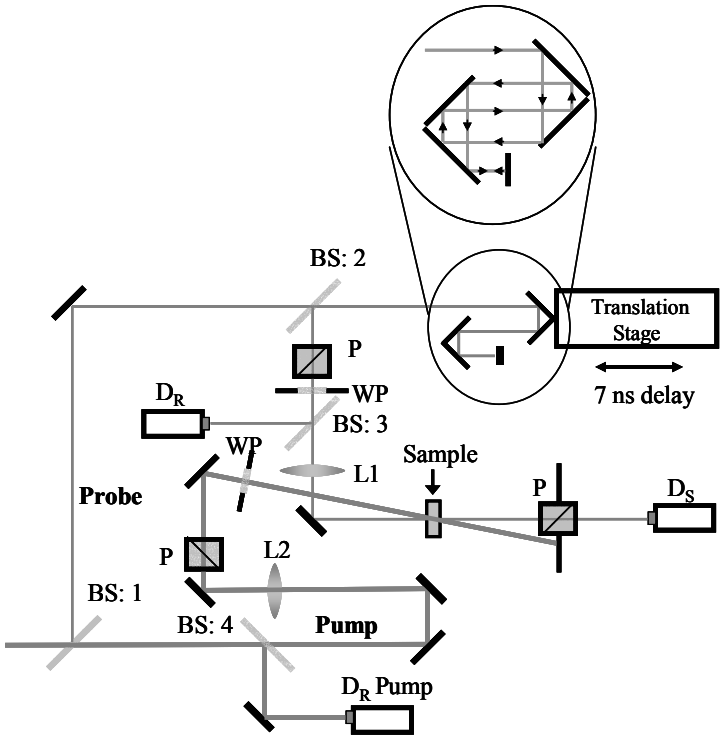

Figure 3.2: Pump-probe experimental set-up, with inset showing path through corner cubes.BS:1,3,4: glass plates w/ one side AR-Coated, BS:2: 50:50 beam splitter, P: polarizer, WP: half-waveplate, L1: 15 cm focal length lens, L2: 75 cm focal length, D_R,D_S: reference and signal detectors for probe, respectively, D_R Pump: Energy reference detector for pump.

3.2.3 Two-Color Femtosecond Polarization-Resolved Pump-Probe Method

The laser system used for these experiments was a Clark-MXR 2001 Ti:sapphire amplified, frequency-doubled, erbium-doped fiber ring oscillator system pumping two optical parametric generator/amplifiers, OPG/A (Light Conversion Ltd., model TOPAS), providing 100 - 120 fs (FWHM) pulses with independently tunable wavelengths from 0.55-2.2 μm. The general experimental set-up is shown in Figure 3.3. A more detailed description of this experiment can be found in Ref. [48]. The pump beam was either the output of the OPG/A which has pulse

energies of tens of microjoules or the output of the Clark-MXR 2001 directly (775 nm) or its second harmonic (388 nm). The probe beam was either the output of the OPG/A or a subpicosecond white-light continuum (WLC) generated by focusing a ~1μJ pulse from an OPG/A at a wavelength of 1400 nm into a 2 mm thick sapphire plate [58]. Depending on the probe wavelength used, two different detection systems were used. In the visible region, large area Si photodiodes were used with narrow-band filters with a bandwidth of 10 nm to select a portion of the transmitted WLC probe beam. At wavelengths longer than 1000 nm the probe beam was derived directly from the OPG/A and was detected with germanium photodiode detectors. The probe can be delayed with respect to the pump beam up to 1 nsec, which is not sufficient to measure excited state or reorientation decay times, but the purpose of these experiments was to measure the nonlinear transmittance as a function of the relative polarization of pump and probe. These experiments were carried out for fixed delays of 0.6 picoseconds and 30 picoseconds.

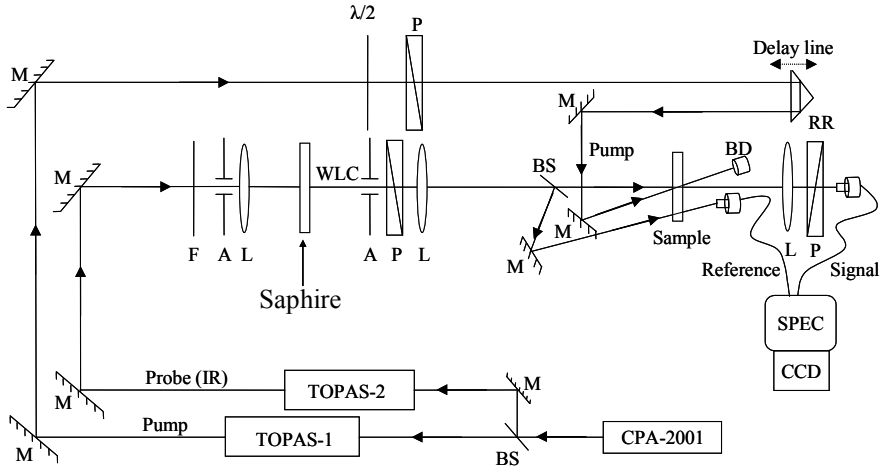

Figure 3.3: Schematic of femtosecond pump-probe setup. BS-60/40 beam splitter, M: mirror, λ/2: half waveplate, P: polarizer, RR: retro-reflector, BD: beam dump, L: lens, F: neutral density filter, NBF: narrow band filter, SPEC, fiber input spectrometer, CCD: CCD dual diode array for spectrum visualization.

3.3 Experimental Results

3.3.1 Steady-State Fluorescence Excitation Anisotropy Results

It is well-known that the absorption spectra in the visible and near IR region for PDs are characterized by a strong single band, $S_0 \rightarrow S_1$, with a typical FWHM = (750 - 950 cm^{-1}) - see Figure 1.5. A small vibrational maximum due to carbon-carbon deformational vibrations is situated about 1200 cm^{-1} above the main absorption peak. The absorption spectra in the short wavelength region are characterized by small intensity and strongly overlapped bands, which correspond to transitions from the ground to the higher excited states. In order to distinguish between different $S_0 \rightarrow S_n$ (n = 2, 3…) transitions, we performed excitation anisotropy

measurements. In these measurements, the fluorescence intensity near the peak fluorescence wavelength, resolved into components parallel ($I_{\parallel}$) and perpendicular ($I_{\perp}$) to the excitation polarization, was measured as a function of excitation wavelength (λ). The steady-state anisotropy excitation spectra, $R_{Fl}(\lambda)$ for PD 2338 and PD 2335 in glycerol are presented in Figures 3.4(a)-3.5(a). Measurements in ethanol show the same positions in anisotropy peaks but with smaller anisotropy values (maximum 0.06 - 0.07) due to the fast reorientation times that depolarize the fluorescence. In high viscosity glycerol solutions the rate of reorientational motions in the excited state is much slower than in ethanol and anisotropy values within the first absorption band are high and close to the theoretical limit of 0.4 [54].

(a)

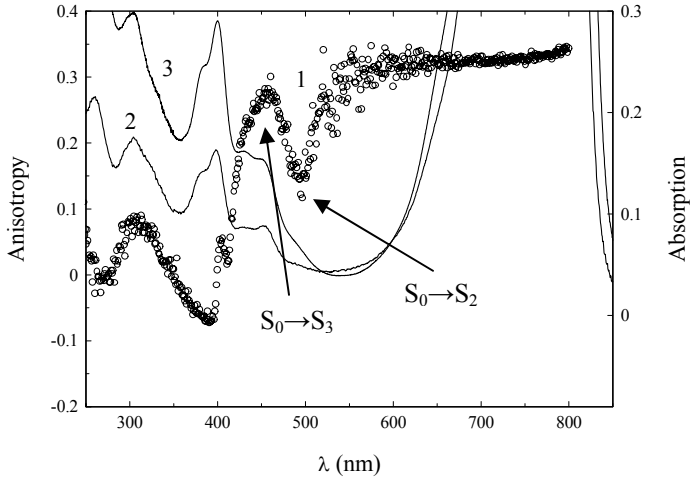

(b)

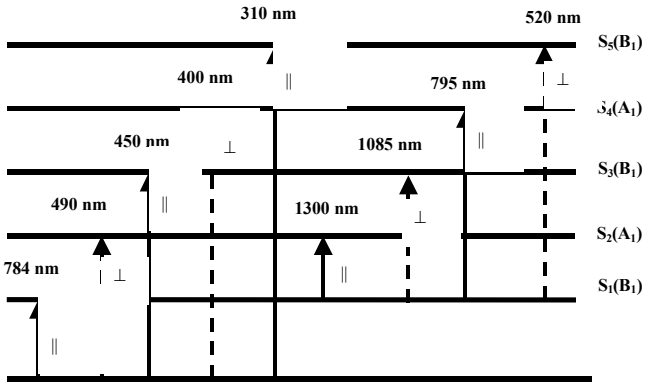

Figure 3.4: (a) Excitation anisotropy (1), left axis, and linear absorption spectra in ethanol (2) and glycerol (3), right axis, for PD 2338; (b) Simplified transition modeling for PD 2338.

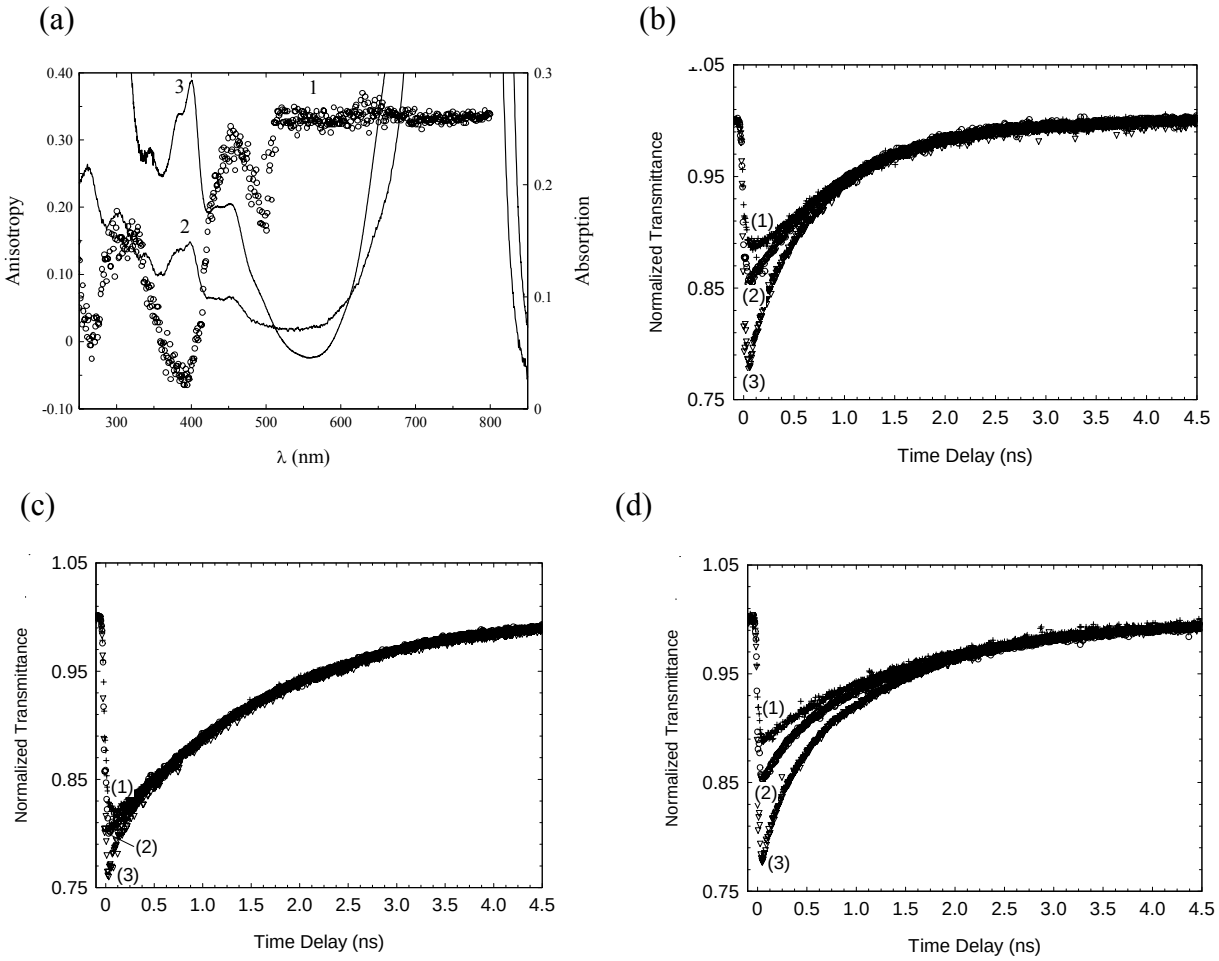

Figure 3.5: (a) Steady-state excitation anisotropy (1), left axis, and linear absorption spectra in ethanol (2) and glycerol (3) for PD 2335, right axis. Pump-probe results for PD 2335 in ethanol (b), methylene chloride (c), and PUA (d) for the pump polarization perpendicular (1), at the magic angle (2), and parallel (3) w.r.t the probe.

The results for the location of the excited-state energy levels, maximum anisotropy, and the orientation of the transition dipole moments from Figures 3.4(a)-3.5(a) are summarized in Table 3.1. The main results are that both dyes have a similar energy level structure with the

transition dipole moment with the largest angle relative to the $S_0 \rightarrow S_1$ transition associated with the $S_0 \rightarrow S_4$ transition ($60^0 - 65^0$) and the smallest with the $S_0 \rightarrow S_3$ transition ($15^0 - 20^0$). For comparison, the absorbance is plotted together with the anisotropy in Figures 3.4(a)-3.5(a). There is a correlation between the position of the $S_0 \rightarrow S_n$ transitions found from the anisotropy excitation spectrum and the position of the short wavelength absorption bands for both dyes. For example, PD 2338 has a low intensity shoulder in the absorption spectrum near 490 nm that may be connected with the $S_0 \rightarrow S_2$ transition. More intense bands around 450 nm and 400 nm are related to $S_0 \rightarrow S_3$ and $S_0 \rightarrow S_4$ transitions, respectively.

Table 3.1: Results for the steady-state fluorescence anisotropy measurements for PD 2338 and PD 2335.

Energy Transition	Spectral Peak of Anisotropy (nm)	Maximum Anisotropy	Transition Moment Orientation
PD 2338			
$\mathbf{S_0 \rightarrow S_2}$	490	0.12 – 0.16	$39^0 - 43^0$
$\mathbf{S_0 \rightarrow S_3}$	450	0.26 – 0.29	$25^0 - 29^0$
$\mathbf{S_0 \rightarrow S_4}$	410	-0.05 – -0.08	$60^0 - 63^0$
$\mathbf{S_0 \rightarrow S_5}$	310	0.06 – 0.1	$45^0 - 49^0$
PD2335			
$\mathbf{S_0 \rightarrow S_2}$	500	0.16 – 0.20	$35^0 - 40^0$
$\mathbf{S_0 \rightarrow S_3}$	450	0.27 – 0.31	$23^0 - 28^0$
$\mathbf{S_0 \rightarrow S_4}$	390	-0.04 – -0.07	$59^0 - 63^0$
$\mathbf{S_0 \rightarrow S_5}$	310	0.12 – 0.18	$37^0 - 43^0$

The spectral peak of anisotropy gives the location of the excited-state energy levels. The maximum anisotropy refers to the anisotropy at the peak spectral position. The transition moment orientation (β_{Fl}) is relative to the emission dipole moment and is calculated using the maximum anisotropy and Eq. 22.

The next step of in the investigation was to estimate the position of the $S_1 \rightarrow S_n$ (n = 2, 3 and higher) transitions using a methodology based on the steady-state anisotropy measurements and quantum-chemical calculations as described in Negres, et. al. [48] for similar dyes. As an example of this modeling, the results for transitions in PD 2338 are presented in Figure 3.4(b). Excited-state absorption bands $S_1 \rightarrow S_2$ and $S_1 \rightarrow S_5$ were observed experimentally as described in reference [48].

3.3.2 Polarization-Resolved Pump-Probe Results

To further our understanding of the nature of ESA in these dyes we have undertaken a detailed investigation of their excited-state dynamics using the polarization-resolved pump-probe technique. As shown in section 3.2.2 this method can be used to separate the lifetime decay from the orientational diffusion kinetics, while also providing information about the orientation of the transition dipole moment between the pump and probe transitions. The results for the normalized transmittance versus time delay for several PDs in different media are shown in Figures 3.5-7. Figures 3.5 (b, c, d) and 3.6 (a, b, c) show the experimental data for PD 2335 in ethanol, methylene chloride and PUA. Figure 3.7 (a, b, c) shows the data for PD 2351 in ethanol.

(a)

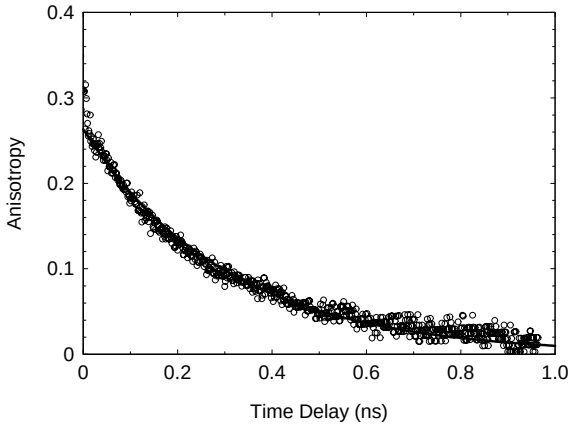

(b)

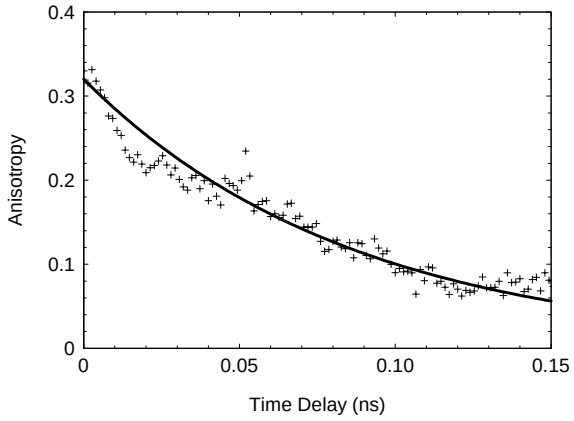

(c)

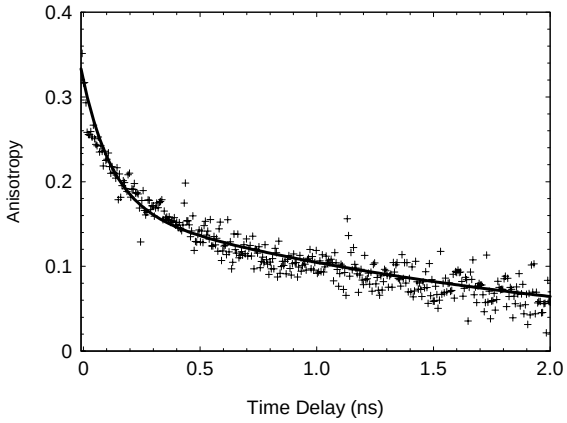

Figure 3.6: (a). Anisotropy results with best-fit curve for PD2335 in ethanol. (b) Anisotropy results with best-fit curve for PD 2335 in methylene chloride. (c) Anisotropy results with best-fit curve for PD 2335 in PUA.

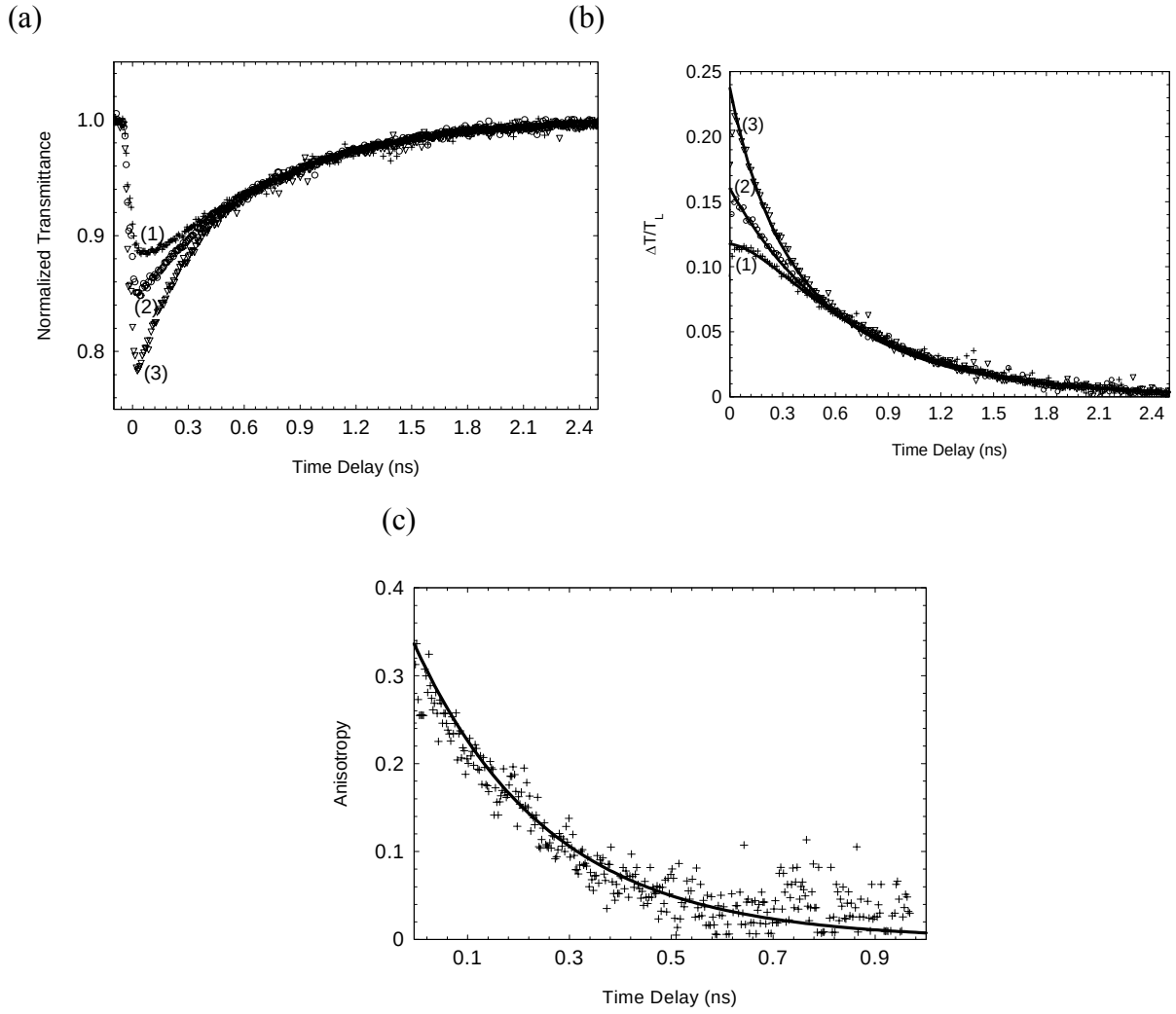

Figure 3.7: (a) Results for PD 2351 in ethanol: Normalized probe transmittance for pump polarization perpendicular (1), magic angle (2), and parallel (3) with respect to the probe beam. (b) Results for PD 2351 in ethanol: Change in transmittance ($\Delta T / T_L$) with best fits for pump polarization perpendicular (1), magic angle (2), and parallel (3) with respect to the probe beam. (c) Anisotropy data with best fit.

From the magic angle and anisotropy curves we can determine the excited-state decay time τ_F, the rotation time τ_R, and the maximum anisotropy, R_{pp}. The values for τ_F and τ_R for all

the dyes investigated are presented in Table 3.2 and the analysis of these results is given in the next section. Determination of R_{pp} can become complicated for some molecules by the influence of the coherent beam-coupling effect [57] which obscures the values of ΔT when the beams are overlapped due to the exchange of energy between the pump and probe. This occurred for PD2350 and was corrected for by taking the value of the anisotropy directly after the coupling signal. Accurate values of R_{pp} can be obtained with a short time delay pump-probe measurements taking special care to determine the zero delay position as described previously in Section 3.2.2. This data is shown in Table 3.3.

Table 3.2: Calculated (τ_R^C) and experimental (τ_R) rotation times in different host media.

Dye	Solvent	η mPa*s	Δf	T_L	C (x10^4) M	τ_F (ps)	τ_R (ps)	$\tau_R{}^C$ (ps)	V (Å)	m
824	ETH	1.074	0.29	0.83	1	145	330	130	490	12
824	ETG	16.1	0.27	0.8	1	140	2100	2000	490	0-1
2257	ETH	1.074	0.29	0.87	3	40	-	150	550	-
2350	ETH	1.074	0.29	0.81	2	800	200	100	390	6
2350	ETG	16.1	0.27	0.81	1.7	1200	-	1600	390	-
2351	ETH	1.074	0.29	0.79	0.5	660	260	110	400	9
2351	ETG	16.1	0.27	0.78	0.5	760	2700	1600	400	4
2332	ETH	1.074	0.29	0.71	3.5	110	650	150	570	30
2332	ETG	16.1	0.27	0.71	3.5	90	-	2300	570	-
2335	ETH	1.074	0.29	0.88	3	880	300	165	620	10
2335	PUA	-	-	0.78	5	1500	130 2600	-	620	-
2335	MCL	0.413	0.21	0.82	4	1560	85	65	620	2
2338	PUA	-	-	0.78	25	1300	200 2100	-	580	-
2338	ETH	1.074	0.29	0.88	12	900	400	160	580	15

η and **Δf** are parameters of the solvent (viscosity and orientation polarizability). $\mathbf{T_L}$ and **C** are experimental values of linear transmittance and concentration. Sample thickness is 1 mm. **V** and **m** are calculated molecular volume and number of the solvent molecules in the shell. The error bars are estimated to be 10% for τ_F and 15% for τ_R.

Table 3.3: Maximum anisotropy values $R_{pp}(0)$ and calculated angles between pump and probe absorption transition dipole moments for PDs in different media: ethanol (ETH), ethylene glycol (ETG), methylene chloride (MLC) and PUA.

Dye	Solvent	$R_{pp}(0)$	β_{pp}
824	ETH	0.22	33^0
824	ETG	0.25	30^0
2257	ETH	0.26	29^0
2350	ETH	0.38	10^0
2350	ETG	0.4	0^0
2351	ETH	0.34	18^0
2351	ETG	0.4	0^0
2332	ETH	0.3	24^0
2332	ETG	0.28	26^0
2335	ETH	0.32	20^0
2335	PUA	0.35	17^0
2335	MCL	0.33	20^0
2338	PUA	0.32	21^0
2338	ETH	0.34	18^0

The error bars were estimated for $R_{PP}(0)$ to be ±15 %

A more detailed investigation of the orientation of the ESA transition dipole moments was performed by measuring the transmission of the probe beam at a fixed time delay as a function of the angle between the pump and probe polarization. Using this technique with a tunable laser system as described in Section 3.2.3 it may be possible to determine the orientations of all the transition dipole moments in the molecule. The results for PD 2338 in ethanol are shown in Figures 3.8(a, b) and they are discussed in the next Section.

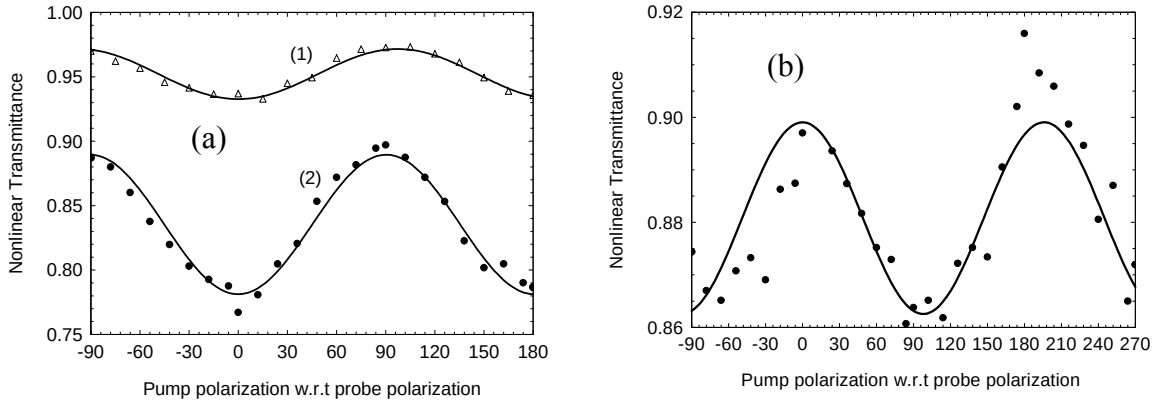

Figure 3.8: Femtosecond pump-probe results for PD 2338 for (a) Excitation with 640 nm into S_1 and probing with 1300 nm (1) into S_2 and probe with 532 nm (2) into S_5; (b) Excite with 388 nm into S_4 and probe with 532 nm into S_5 after ultrafast $S_4 \rightarrow S_1$ relaxation.

3.4 Discussion

3.4.1 Excited-State Dynamics

To study the nature of rotational motions in the excited-states of PDs, we performed polarization-resolved pump-probe measurements in several solvents of different viscosity (η) and polarity as well as in the polymeric medium PUA. The polarity of the solvents can be characterized by their orientational polarizability, which is given by

$$\Delta f = \frac{(\varepsilon - 1)}{(2\varepsilon + 1)} - \frac{(n^2 - 1)}{(2n^2 + 1)} \tag{28}$$

where ε is the static dielectric constant and n is the refractive index of the solvent [54]. The values for η and Δf of all solvents are given in Table 3.2.

The anisotropy decay for all the dyes in all solvents is found to be monoexponential with decay times τ_R shown in Table 3.2. The largest lifetime values of 1300 - 1560 ps were obtained for the dyes in PUA and methylene chloride. Reorientation times in ethanol are in the range of 200 – 650 ps; in ethylene glycol: 2100 – 2700 ps and in methylene chloride ~ 75 ps (the shortest τ_R). No correlation was found between the rotational reorientation time and the viscosity of the solvents. To get a basic understanding of this discrepancy we used the simplest possible model, which is the Stokes-Einstein-Debye (SED) model, and PD molecular volumes calculated using the HyperChem software package [59] to predict the rotational reorientation time. The SED model relates the rotational correlation time to the molecular and solvent parameters as:

$$\tau_R^C = \frac{\eta V}{kT} \tag{29}$$

where V is the molecular volume of the rotating units, k is the Boltzman constant and T is the temperature. As can be seen from Table 3.2, all calculated τ_R^C in ethanol are 2-3 times less than the measured τ_R, meaning that the actual volumes of the rotating units are much larger than the corresponding van der Waals volumes. This difference may be attributed to the interaction between the dye and solvent leading to the formation of a solvent shell. We calculated the number of solvent molecules forming this shell by taking the difference between the van der Waals volume of the molecule and volume predicted the experimentally measured τ_R. In Table 3.2 we list the number of solvent molecules (m) forming the surrounding solvent shell. The ethanol corresponds to a "stick" rotation condition [54] with the number of molecules forming the solvent shell ranging from six to thirty. PD2335 in methylene chloride corresponds to more of a "slip" rotation condition [54].

Anisotropy decay in PUA is described by two quite different exponential decay times. We first reported the measurement of a double exponential decay of polymethines in PUA in reference [59]. In this work we proposed the coexistence of two different decays may be explained by the restriction of the fast decay process (190-200 ps) in the polymer leading to only partial depolarization of the excited state. Complete loss of anisotropy was observed as a result of the slower decay process (2100-2600 ps). This explanation is based on the formation of microcavities of free volume due to the photopolymerization process. The fast rotational component may be connected with the rotation of molecular fragments, which are limited by the free volume of the microcavities. The slower rotational component is probably connected with the rotation of the entire molecule. Due to the viscoelastic properties of PUA (glass transition temperature is ~ -50 ^{0}C) this material at room temperature is characterized by a faster segmental dynamics and microscale fluctuations of density compared to the glassy state. From our experimental results we can conclude that complete depolarization in the nanosecond time scale is a property of the highly elastic state of the polymeric host. Therefore, the polarization-resolved pump-probe technique may be successfully used to study the microstructure and microviscosity of polymeric materials.

3.4.2 Orientation of Excited-State Transition Dipole Moments

The orientation of the $S_1 \rightarrow S_n$ (n = 2, 3 and higher) transition dipole moments is connected to the maximum anisotropy value R_{pp}, from which the angle β_{PP} can be calculated as described in Section 3.3.2. These values for all the PDs studied are presented in Table 3.3. One of our goals is to compare the excited-state transition dipole moment orientations ($S_1 \rightarrow S_n$)

measured using picosecond and femtosecond pump-probe experiments to those orientations calculated from the difference in angular orientation of the $S_0 \rightarrow S_n$ and the $S_0 \rightarrow S_1$ transition dipole moments determined from the steady-state fluorescence anisotropy measurements. We performed our investigation in the following two ways. First, we selected PDs which differ by the spectral position of the linear absorption band relative to the 532 nm pump beam. For PDs 2351, 2350, 2335, and 2338 the pump beam is within the $S_0 \rightarrow S_1$ band, for PDs 2257 and 824 – within the $S_0 \rightarrow S_2$ band and for PD 2332 – within the $S_0 \rightarrow S_3$ band. The probe beam of the same wavelength (532 nm) is absorbed by the $S_1 \rightarrow S_5$ transition as was determined from the transition modeling of all the dyes.

Let us analyze the experimental data shown in Table 3.3. The largest anisotropy values of 0.4 (theoretical limit) have been obtained for PDs 2350 and 2351 in ethylene glycol and slightly reduced values of 0.38 and 0.34 – in the ethanol solution. For PDs 2335 and 2338 anisotropy values are in the range of 0.32 - 0.35, meaning that for the dyes excited directly into the $S_0 \rightarrow S_1$ band (or high vibrational levels of this band) the $S_1 \rightarrow S_5$ transition moment is oriented nearly parallel to the ground-state absorption dipole moment ($< 20^0$). The smallest anisotropy values of 0.22 – 0.26 (and the largest angles 29^0 - 33^0) have been obtained for PDs 824 and 2257 excited into the $S_0 \rightarrow S_2$ band, which correlates well with the steady-state excitation anisotropy measurements. The intermediate values in anisotropy 0.28 -0.3 have been obtained for PD 2332, which is excited into the $S_0 \rightarrow S_3$ band.

The second set of measurements was performed for PD 2338 using the femtosecond polarization resolved pump-probe setup as described in Section 3.2.3. We tested two excited-state absorption bands, the $S_1 \rightarrow S_5$ and the $S_1 \rightarrow S_2$ by pumping into the main absorption (640

nm) band $S_0 \rightarrow S_1$. Anisotropy values were measured at two time delays: 0.6 ps and 30 ps. We found that R(t=0.6 ps) = 0.36 and R(t=30 ps) = 0.32 for both transitions, see Figure 3.8 (a). This means that both the excited-state transitions are oriented almost parallel to each other as well as to the $S_0 \rightarrow S_1$ transition. A slight decrease in anisotropy from 0.36 to 0.32 is indicative of a $\sim 3^0$ reorientation during the 30 ps time delay. After that we tuned the pump wavelength to 380 nm ($S_0 \rightarrow S_4$ transition) and fixed the probe wavelength at 532 nm ($S_1 \rightarrow S_5$ transition). As can be seen from the steady-state excitation anisotropy measurements shown in Figure 3.4 (a), the $S_0 \rightarrow S_4$ transition forms the largest angle ($\sim 65^0$) with the ground-state dipole moment orientation; therefore the anisotropy should be strongly affected. The experimental pump-probe data is presented in Figure 3.8 (b). The calculated anisotropy value of R(t=30 ps) = -0.1. That means that the angle between the $S_0 \rightarrow S_4$ and $S_1 \rightarrow S_5$ transition dipole moments is approximately 65^0. The same angle was found for the relative orientation of the $S_0 \rightarrow S_1$ and $S_0 \rightarrow S_4$ transitions from the steady-state measurements.

Thus, we can conclude that the two measurement techniques give the same results, indicating that after excitation the molecule's ultrafast relaxation processes do not appreciably change the transition dipole moment direction. From our point of view further work in this direction could lead to the development of a methodology, which can be applied to cases in which the steady-state measurements cannot be used, for example in cases of nonfluorescent molecules or solvents with low viscosity etc. This technique will be discussed in the next chapter.

However, we still do not fully understand several of the experimental results relating to the strength and orientation of the transitions. It is well known that the orientation of the

transition dipole moment is determined by the wavefunctions of the states involved and the molecular structure. The symmetry of the PDs studied is C_{2V} (existence of the axis and plane of symmetry) leading to the symmetry representation of the energy states given in Figure 3.4 (b). The direction of the $S_0 \rightarrow S_n$ transition moment in the Parr-Pariser-Pople (PPP) quantum-chemical calculations with the approximation of a symmetric charge distribution [48], may be parallel to the polymethine chromophore principle axis ($S_0 \rightarrow S_1$, $S_0 \rightarrow S_3$, $S_0 \rightarrow S_5$ …) or perpendicular to it ($S_0 \rightarrow S_2$, $S_0 \rightarrow S_4$ …). Typically for PDs only the orientations of the $S_0 \rightarrow S_1$ and $S_0 \rightarrow S_4$ transition moments are close to the calculated directions. Others show substantial differences. For example, for PD 2338 (Figure 3.4 (a)), the $S_0 \rightarrow S_5$ transition (parallel by calculations) is even more perpendicular than the $S_0 \rightarrow S_2$ transition. In the literature this disagreement is usually explained by invoking extra processes such as deformational and torsion vibrations in excitation, relaxation and emission processes [50]. The orientation of the $S_1 \rightarrow S_n$ transition calculated by standard AM1 and PPP quantum-chemical methods [48] is also shown in Figure 3.4 (b). According to the symmetry selection rules, the $S_1 \rightarrow S_2$ and the $S_1 \rightarrow S_4$ transitions should be allowed and oriented parallel to the $S_0 \rightarrow S_1$ transition, which is in agreement with the measurements. Transition $S_1 \rightarrow S_3$ was never observed experimentally. Transition $S_1 \rightarrow S_5$, which is responsible for the large broadband ESA in the visible region should also be forbidden and oriented perpendicular to the $S_0 \rightarrow S_1$ transition according to the symmetry assignment. Therefore, we consider these results as an indication of strong symmetry breaking for the symmetric PDs that have a relatively long polymethine chromophore. Evidence for symmetry breaking in some PDs was discussed in [60], where “totally symmetric and

nontotally symmetric" path mechanisms were proposed. Our understanding is that the development of a new approach in quantum-chemical calculations based on nontotally symmetric charge distributions in structurally symmetric PDs would lead to an understanding of the strength and orientation of the $S_0 \rightarrow S_n$ and the $S_1 \rightarrow S_n$ transitions. The concept of symmetry breaking in polymethines will be further discussed in Chapter 5.

3.5 Conclusion

Picosecond and femtosecond polarization-resolved pump-probe measurements give a variety of information about lifetimes, molecular motions, anisotropy decays and transition orientations in different environments.

We have described a detailed investigation of the dynamics of a new series of PDs. From the anisotropy decay data we mesured orientational diffusion times in PUA and solvents and witnessed two different types decays. Reorientational decays in the solvents followed a single exponential behavior that is evidence for the allowed molecular motions leading to complete depolarization of the excited states. From the comparison of measured and calculated rotation times, we considered the solvent effects ("stick" and "slip" rotation conditions). In contrast to liquid solutions, decays in PUA followed a double exponential behavior with two very different rotation times. The fast rotational component may be connected with the rotation of molecular fragments, which are limited by the free volume of microcavities. The slower rotational component is probably connected with the rotation of the entire molecule due to the faster segmental dynamics and microscale fluctuations of density in viscoelastic PUA.

We have analyzed the maximum anisotropy values in the nonlinear response of PDs, which made it possible to calculate the angles between the excited-state (probe) and ground-state (pump) transitions. These results were compared to the steady-state fluorescence anisotropy measurements and excellent agreement was found between the experiments.

However, several experimental results relating to the strength and orientation of the transitions still remain unanswered. We expect that the development of a new approach in quantum-chemical calculations based on charge distributions that are not completely symmetric in structurally symmetric PDs would lead to progress in obtaining a deeper understanding of the nature of ESA transitions and to the prediction of the nonlinear optical properties of newly synthesized dyes. This effect will be discussed in chapter 5.

CHAPTER 4:ABSORPTION ANISOTROPY STUDIES OF POLYMETHINE MOLECULES

4.1 Introduction

A detailed investigation of the ESA dynamics and molecular motions in liquid solutions and in an elastic polymeric medium using a time-resolved induced anisotropy method was presented in the previous chapter. However, a comparison of these results with steady-state fluorescence anisotropy spectroscopy left some questions unanswered. In this chapter we describe experimental studies and give an analysis of the spectral position and the orientation of the transition dipole moments connected with the $S_0 \rightarrow S_n$ transitions (n=1,2,3...) in a set polymethine (PD 3428, PD 1952, PD 2410, PD 2338) molecules. The orientations of the $S_0 \rightarrow S_n$ transitions are commonly determined relative to the fluorescence transition dipole moment ($S_1 \rightarrow S_0$) using the fluorescence anisotropy method, as discussed in the previous chapter. We demonstrate for the first time an experimental technique which relies on the orientation of the ESA transition dipole moments $S_1 \rightarrow S_n$ (n = 2,3, 4...) to determine the spectral position and orientation of the transition dipole moments connected with the $S_0 \rightarrow S_n$ transitions (n=1,2,3...). We show for the essentially linear polymethine molecules that the ESA transition moments can be used for determining the orientation of the $S_0 \rightarrow S_n$ transitions instead of the fluorescence transition dipole moment ($S_1 \rightarrow S_0$). This important conclusion relies on the fact that the transition dipole moment of the most intensive $S_0 \rightarrow S_1$ absorption band, which is known to be parallel to the direction of the polymethine chain (or molecular backbone), is much larger (20 to 400 times) than for all higher transitions ($S_0 \rightarrow S_n,\ n > 1$). Based on these results we propose a

new approach for the investigation of the anisotropy properties of linear polymethine molecules, which can be applied to cases in which the steady-state measurements cannot be used, e.g. in cases of nonfluorescent molecules (e.g. IR-dyes), dyes with fluorescence that lies outside the spectral detection range of conventional spectrofluorimeters or solvents with low viscosity which decreases the anisotropy value due to reorientational diffusion.

The dyes PD 3428, 2338, 1952 & 2410 all have the same length of the polymethine chain (tricarbocyanines) (as seen in Figure 1.4). PD 3428 is unique in the fact that it has an unsubstituted (or unbridged) polymethine chromophore. Other tricarbocyanines differ by the nature of the bridge group: a 6-membered cycle (or trimethylene bridge) for PD 2338, a 5-membered cycle (or dimethylene bridge) for PD 1952 and a 5-membered cycle with an extra double bond (or vinylene bridge) for PD 2410. Therefore, using this series of dyes, we can study the effect of the bridge group on their spectroscopic and anisotropy properties. In chapter 6 we investigate the effect of the bridge structure on the nonlinear optical properties of the dyes.

The experimental techniques used in the investigations described in this chapter:

(1) Linear absorption spectral measurements.

(2) Steady-state excitation fluorescence anisotropy measurements.

(3) Two-color picosecond polarization-resolved pump-probe measurements.

The analysis includes:

(1) Quantum-chemical calculations.

(2) Numerical fitting of the pump-probe measurements.

4.2 Experimental Methods

4.2.1 EKSPLA Picosecond Laser System and OPG

The laser system used for these experiments is a 10-Hz *EKSPLA* PL2143 Nd:YAG laser and an *EKSPLA* PG401/DFG optical parametric generator (OPG) tunable from 0.42 to 2.3 μm. The laser system and OPG will be described below.

The laser system consists of a master and slave (regenerative) cavity to increase stability and power. The master oscillator employees an active-passive modelocking scheme using a flowing saturable absorber dye cell and an electro-optic modulator (Pockels cell) with negative feedback for the passive and active modelocking processes, respectively. This allows for a quasi-stationary operation in the cavity, which produces a very stable pulse (pulse width: ±1.0 %, pulse energy: ±1.5%). Once this quasi-stationary condition is reached the pulse is switched by a Pockels cell and polarizer, into a high Q regenerative amplifier cavity. This is done primarily so the pulse energy can be built up without degrading the saturable absorber dye quickly, which helps in the long term stability of the laser. A third Pockels cell and polarizer is used as a cavity dumper to switch out a single pulse that has energy of approximately 500 μJ. This pulse, after being spatially filtered, is sent through a double pass amplifier. The polarization of the input beam is rotated by 90 degrees between passes to extract the maximum amount of energy. The maximum energy pulse after this amplification stage is 50 mJs. The energy can be easily varied from 500 μJ to the maximum of 50 mJ by adjusting the time delay between the triggering of the oscillator and the amplifier flashlamps. After the amplifier are two KD^*P crystals for frequency generation, the first crystal for second harmonic generation (SHG) and the second for third

harmonic generation (THG). Dichroic beamsplitters are located before, between, and after the crystals to separate out the fundamental, SHG, and THG beams respectively. The THG beam, which has a maximum energy of ≈ 12 mJ, is used to pump an OPG.

The OPG unit is a combination OPG\A based on a beta-barium borate (BBO) crystal. The tuning range covers 420 nm to 2.3 μms with energies of several hundred μJs over the entire tuning curve. A typical turning curve is shown in Figure 4.1. The OPG uses a low energy seed beam split off from the 355 nm pump and passes twice through the BBO crystal. The idler wave is then separated from the generator beam using a long pass filter and the line width is narrowed using a grating and pinhole combination. This beam is then passed through the BBO crystal along with the intense pump beam to make up the OPA stage. This is also a double pass stage and the signal and idler outputs are separated with dichroic filters. The seed beam is also much smaller than the pump beam to produce a high quality spatial beam at the output. This beam however, still needs to be spatially filtered [61] after the OPG to get near diffraction limited behavior.

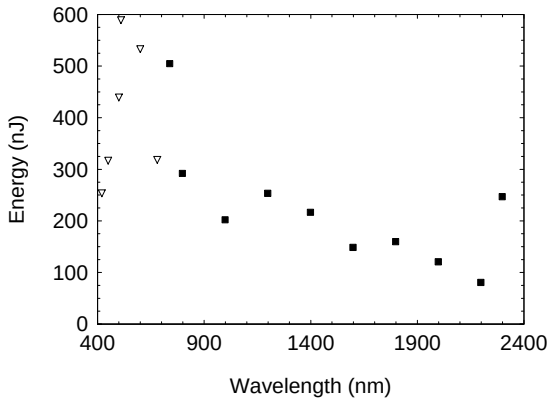

Figure 4.1: OPG tuning curve, signal (triangles), idler (squares).

4.2.2 Picosecond Two-Color Polarization-Resolved Pump-Probe Method

The second harmonic of the Nd:YAG laser with a pulse width of 24 picoseconds (FWHM) is used as the probe. The pump is the output of the OPG, tunable over the range of 420 to 900 nm. The experimental set-up is shown in Figure 4.2. The energy range of the pump beam is between 2-20 μJ, while the probe is held to approximately 1 nJ. The probe beam is focused to a waist of 30 μm (Half Width $1/e^2$ Maximum), while the pump beam's focused waist changes size based on wavelength from 120 to 250 μm (Half Width $1/e^2$ Maximum) over the range of 420 nm to 900 nm, respectively. The pump beam is much larger than the probe beam to ensure that the probe beam senses a region of uniform excitation in the sample. The pump irradiance is at least forty times larger than that of the probe and in most cases several hundred times larger. The probe beam can be temporally delayed with respect to the pump beam up to 15 nanoseconds and its irradiance is kept low so as not to induce any nonlinearity in the sample. The pump and the probe beams are overlapped at a small angle (~ 5°) within the sample so the probe beam can be separated after the sample from the pump as shown in Figure 4.2. The polarization of the probe is fixed and a polarizer placed after the sample is aligned parallel with the probe polarization. The pump polarization is adjusted with a half-wave plate and can be set to any angle with respect to the probe polarization. The probe beam is monitored before and after the sample using large area silicon photodiodes (1cm diameter).

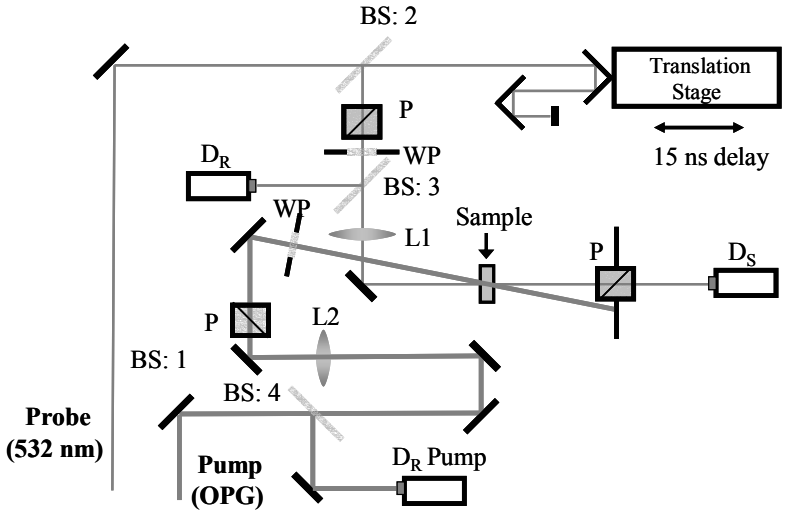

Figure 4.2: Pump-probe experimental set-up. BS:1,3,4: glass plates with one side AR-Coated, BS:2: 50:50 beam splitter, P: polarizer, WP: half-waveplate, L1: 15 cm focal length lens, L2: 75 cm focal length, D_R,D_S: reference and signal detectors for probe, respectively, D_R Pump: Energy reference detector for pump.

4.3 Experimental Results

4.3.1 Steady-State Fluorescence Anisotropy

The steady-state anisotropy excitation spectra, $R_{Fl}(\lambda)$, for PDs 3428, 2338, 1952 and 2410 are presented in Figure 4.3. All measurements were conducted in high viscosity glycerol solutions in which the rate of reorientation in the excited state is slow, and anisotropy values within the first absorption band are high. For some dyes the peak anisotropy is close to the theoretical limit of 0.4 [54], showing that absorption and emission dipole moments are parallel. Measurements were also performed in ethanol to check if any spectral shift in the position of the

excited states occurred in different solvents. No spectral shifts are observed, but the maximum value of anisotropy decreases to 0.06 - 0.07 due to reorientational diffusion effects. From the experimental results presented in Figure 4.3, we can locate the position of the $S_0 \rightarrow S_n$ transitions. For all dyes the highest anisotropy values are observed for the $S_0 \rightarrow S_1$ transition: 0.3 for PD 1952, 0.32 for PD 2338, 0.34 for PD 3428 and 0.38 for PD 2410. The smallest (negative values) are observed for PD 1952 for the $S_0 \rightarrow S_2$ transition and in PD 2338 for the $S_0 \rightarrow S_4$ transition. PD 2410 shows an unusual behavior of anisotropy within several $S_0 \rightarrow S_n$ bands, which will be discussed in more detail in Section 4.4. The positions of the $S_0 \rightarrow S_n$ transitions revealed from the anisotropy spectra, $R_{Fl}(\lambda)$, show good correlation with the positions of the short wavelength absorption bands for all dyes (see also analysis in [62]).

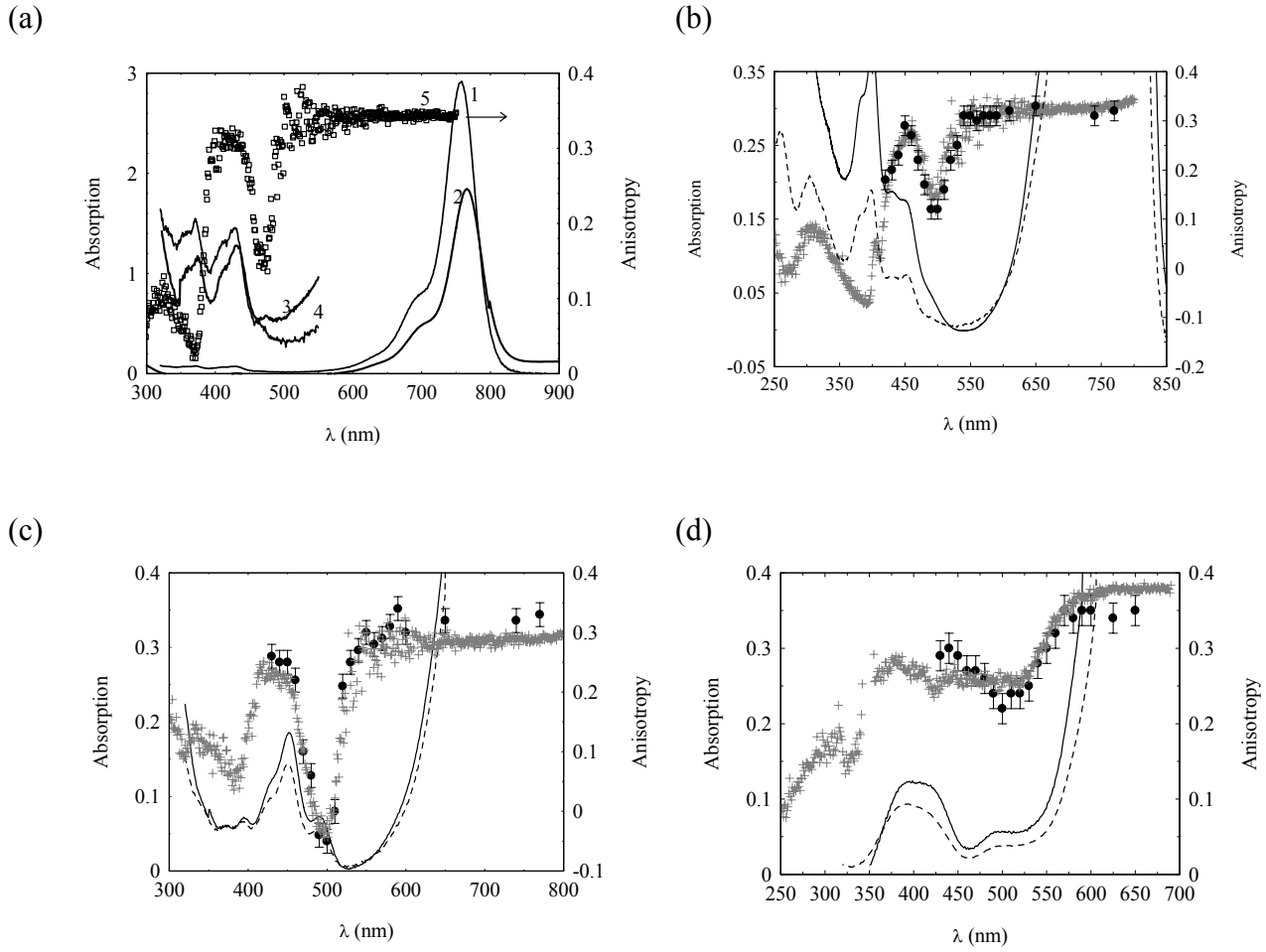

Figure 4.3: (a) Absorption (left axis) and steady-state anisotropy (right axis) for PD 3428 in ethanol and glycerol. Linear absorption in 1) ethanol, 2) glycerol, 3) and 4) are higher concentration samples of ethanol and glycerol, respectively, to show details of excited-states, 5) steady-state anisotropy in glycerol. For PD 2338 (b) 1952 (c) and 2410 (d) is shown the steady-state (+) and ESA (●) anisotropy (left axis) along with linear absorption (right axis) in ethanol (dotted line) and glycerol (solid line).

4.3.2 Two-Color Picosecond Polarization-Resolved Pump-Probe

The concept of this new two-color pump-probe anisotropy experiment is similar to that of the fluorescence anisotropy experiment, but instead of monitoring the excited-state population

density with the fluorescence intensity ($S_1 \rightarrow S_0$ transition) it is monitored by the absorption of a weak probe beam ($S_1 \rightarrow S_n$ transition). The change in transmittance of the parallel and perpendicular components of the probe polarization with respect to the pump is used instead of the fluorescence components ($I_{\parallel}$ and $I_{\perp}$) to determine the anisotropy. In this case the anisotropy measures the angle between the absorption transition dipole moment ($S_0 \rightarrow S_n$ transition) of the pump beam and the ESA transition dipole moment of the probe beam ($S_1 \rightarrow S_n$ transition) at time $t \sim 0$ (as compared to the reorientation diffusion time).

Figure 4.3 (b,c,d) shows the anisotropy spectra for PDs 2338, 1952 and 2410, calculated from the pump-probe experiments with the tunable pump from 420 nm to 900 nm, along with the anisotropy curves measured using the steady-state fluorescence method. There is excellent correlation between these two methods. Both pump-probe and fluorescence methods can resolve all the features in the anisotropy data for the tricarbocyanine dyes; however, the pump-probe method has the distinct advantage of being applicable to a wider range of molecules (e.g. nonfluorescent molecules). On the other hand, the pump-probe experiment takes considerably more time to perform and requires short pulse tunable sources.

We applied this method to study the anisotropy of the tetracarbocyanine dye PD 2332. Because of its long wavelength spectral position, the fluorescence quantum yield is very small and we could not perform the steady-state fluorescence measurements using the existing PTI Quantamaster Spectrofluorimeter. Pump-probe anisotropy results for this dye are shown in Figure 4.4 along with its absorption spectrum in this region. The following four electron transitions could be resolved from this data. As can be seen, the anisotropy values are relatively high (≈ 0.3) and constant over the $S_0 \rightarrow S_1$ transition and exhibit a significant drop (to 0.13) over

the second band ($S_0 \rightarrow S_2$ transition) with the peak position around 570 nm. The next increase in the anisotropy value reveals the position of the $S_0 \rightarrow S_3$ transition (470 nm- 520 nm) which is nearly parallel to the $S_0 \rightarrow S_1$ transition dipole moment. The next drop in anisotropy (to 0) corresponds to the position of the $S_0 \rightarrow S_4$ transition (near 450 nm) and indicates a significant angle relative to the $S_0 \rightarrow S_1$ transition dipole moment.

These ESA anisotropy measurements represent a very useful approach which can be applied to cases in which the steady-state method cannot be used, for example in cases of nonfluorescent (or low fluorescence quantum yield) molecules or solvents with low viscosity which decreases the anisotropy value due to reorientational diffusion.

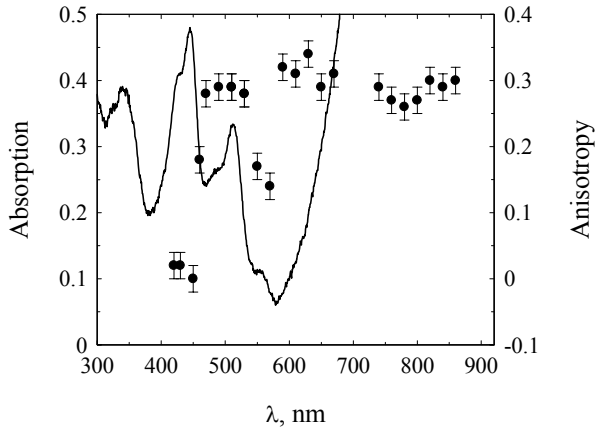

Figure 4.4: ESA-anisotropy (left) for PD 2332 along with linear absorption (right) in ethanol.

4.4 Discussion

In this section the quantum chemical calculations, which were performed by Olga Przhonska and colleagues at the Institute of Physics and the Institute of Organic Chemistry, National Academy of Sciences, are summarized. A complete treatment of the quantum chemical calculations can be found in reference [63]. The intent of this section is to demonstrate the impact of the experimental results on the understanding of the nature of the transitions in polymethines.

4.4.1. Methodology of quantum-chemical calculations

The equilibrium molecular geometry and the electron charge distribution for the dyes in the ground and excited states were performed employing the semi empirical AM1 method (MOPAC package, gradient < 0.01 kcal/mol). It was demonstrated previously that the charges and C-C bond lengths calculated in this method are in good agreement with the corresponding values obtained in the ab-initio approximation [64,65]. The optimization of the geometry in the excited state was calculated taking into account the changes in the bond lengths and valence angles (optimization of the torsion angles is not considered). This approximation is valid since the steady-state anisotropy measurements were performed in a highly viscous glycerol solution preventing torsional deformations, and the ESA anisotropy experiments were measured at time t ≈ 0 before large changes in the torsion angles could occur. See details below. The wave function of the excited state is expressed as the expansion of the excited configurations corresponding to all the possible electron transitions from the three highest occupied molecular orbitals (HOMO) and the two lowest unoccupied molecular orbitals (LUMO).

4.4.2. Quantum-chemical calculation. Molecular geometry and electron density distribution

Quantum-chemical calculations were performed with the goal of understanding the features of the electron density distribution in the ground and excited states as well as the changes in the molecular geometry of PDs under excitation to explain the maximum anisotropy values experimentally measured. The quantum-chemical calculations examine the alternation of the charge magnitudes at the neighboring atoms, which is referred to as a charge wave. The charge wave is directly connected with the alternation of the lengths of the neighboring C-C bonds [64,65]. It has previously been shown [64,66] that the meaningful quantity is the difference in bond lengths between neighboring C-C bonds, which is given by the bond length alternation as $\Delta l = \left| l_{n,\, n+1} - l_{n+1,\, n+2} \right|$, where $l_{n,\, n+1}$ is the bond length between two neighboring n and n+1 carbon atoms (π-centers). Similarly, the differential property of the charge wave can be described by the amplitude of charge alternation, $\Delta q = \left| q_n - q_{n+1} \right|$, where q_n and q_{n+1} are the charges at the two neighboring n and n+1 atoms [65,67,68].

The quantum chemical analysis was performed for a model chromophore, which does not have end groups or any type of bridge structure, and the tricarbocyanine PDs 3428, 2338, 1952, 2410 and the tetracarbocyanine PD 2332. The model structure is given as:

$$\mathbf{H_2C^+ - (CH = CH)_{10} - CH = CH_2}$$

The comparison between the model chromophore and the polymethines provide insights into the effects of bridge structure and terminal groups on both the charge and the length amplitude alternation functions. In addition to the analysis of the ground-state Δl and Δq functions for the polymethines the excited-state Frank-Condon and relaxed state functions were also examined.

The salient points of the quantum-chemical analysis of the charge distribution and optimal geometries for the polymethines are summarized below:

(1) All features of the electron density distribution and molecular geometry in the ground and first excited state, S_1, can be explained using the two functions of amplitude of the charge alternation (Δq) and bond length alternation (Δl).

(2) Introduction of the terminal groups to the model polymethine chromophore causes a deformation in the shape of the charge wave leading to an increase in the amplitude of the charge wave near the nitrogen atoms of these terminal groups.

(3) The $S_0 \rightarrow S_1$ excitation leads to a considerable decrease in the amplitude of the charge alternation. Also in the S1-state the charge wave exhibits two degenerate minima, which become more pronounced and asymmetric in the relaxed geometry.

(4) Cyclization of the part of the polymethine chromophore by a 6-membered cycle (trimethylene bridge) does not cause considerable distortion of the ground-state Δq- and Δl-functions with respect to the unsubstituted chromophore. The distortion of the equilibrium geometry of the polymethine chain in PDs due to a 5-membered cycle (dimethylene bridge) is substantial. This distortion occurs even in the ground state of the molecule which leads to an increase in the ground state absorption cross-section.

(5) Deformations in the molecular geometry under excitation (from Franck-Condon to relaxed state), accompanied by changes in the valence angles and bond lengths, are responsible for the reduction in the anisotropy of the $S_0 \rightarrow S_1$ transition from the theoretical value of 0.4 to the experimentally measured values of 0.30 to 0.38 (depending on the dye).

4.4.3. Quantum-chemical calculation. Electron transitions and effect of the cyclization by hydrocarbon bridge group

The goal of the quantum-chemical calculations performed in this section is to understand both the effects of charge redistribution under excitation and cyclization on the strength and spectral position of the ground and excited-state transitions. To study the effect of charge redistribution on the strength of the ground state transition the quantity $Q = \left|\Delta q^* - \Delta q^0\right|$ is defined, where Δq^0 and Δq^* are Δq-functions in the ground and excited S_1-states respectively. From the quantum chemical calculations it was found that the molecules with the largest Q-value had the largest ground state cross-sections.

The effect of cyclization on the spectral position of the absorption band can be interpreted within the framework of perturbation theory [69]. The change in the energy of the i-th molecular orbital upon cyclization may be described by the general formula:

$$\Delta\varepsilon_i = (\varepsilon_i - \varepsilon_j)^{-1}\left(\sum_n \sum_m C_{in} C_{jm} \beta_{nm}\right)^2 \qquad (30)$$

where ε_i and C_{in} are the energy and coefficients of the i-th molecular orbital of the unsubstituted dye molecule; ε_j and C_{jm} are the energy and coefficients of the j-th molecular orbital of the bridge; β_{nm} is the resonance integral of the bonds formed upon cyclization, which characterizes the interaction between the n-th atom of the chain and the m-th atom of the bridge. It is important to note that $j = 1$ because only the first MO of the bridge affects the energy position of the molecule. From this analysis it was found that the 6-membered cycle (trimethylene bridge) in PD2338 and the 5-membered cycle (dimethylene bridge) in PD1952 only weakly influence the electron transfer along the polymethine chain. In both dyes this weak interaction results in a

redshift of the absorption peak compared to the unbridged dye (PD3428) and has no effect on orientation of the transition dipole moments. The 5-membered vinylene cycle (Vinylene bridge) in PD2410 is a conjugated bridge and strongly effects the electron transfer along the polymethine chain. The effect on the peak spectral position is a blueshift, which is opposite to that of PD2338 and PD1952. The effect on the orientation of the transition dipole moments is even more dramatic, which leads to the unusual anisotropy shown in Figure 4.3d. From the quantum-chemical calculations it was found that the energy levels of the vinylene bridge influence the orientation of the transition dipole moments for all even transitions ($S_0 \rightarrow S_2$, S_4) and not the odd transitions ($S_0 \rightarrow S_3$, S_5) in such a way that the orientation of the transition dipole moments for all the excited states is the same.

4.4.4. Anisotropy in Excited-State Absorption Transitions

We have shown in Section 4.3.2 that in all polymethine molecules the ESA transition dipole moments (the most intense $S_1 \rightarrow S_5$ transition was used in these cases) can be used for determining the orientation of the $S_0 \rightarrow S_n$ transitions as opposed to the fluorescence transition dipole moment ($S_1 \rightarrow S_0$). This important result can be explained using the following three concepts. *First*, polymethine molecules are linear conjugated molecules, so the most intense absorption band occurs for the transition in which all π-electron centers are involved in the transition and the transition dipole moment is parallel to the direction of the polymethine chain (or molecular backbone), which is the $S_0 \rightarrow S_1$ transition. This well-known conclusion is based on the analysis of the linear absorption ($S_0 \rightarrow S_n$) spectra and quantum-chemical theories [70,71].

Our calculations show that for all the PDs studied the $S_0 \rightarrow S_1$ transition dipole moment is much larger (20 to 400 times) than all higher transitions ($S_0 \rightarrow S_n,\ n > 1$). *Secondly*, the most intense excited-state transitions are parallel to the polymethine chain [48, 62], again due to the fact that these molecules are linear conjugated molecules. These transitions, which are parallel to the polymethine chromophore, are the only observable $S_1 \rightarrow S_n$ transitions. The small percentage of the population in the excited-state (N_1) makes it difficult to observe weak excited-state transitions. From our calculations the largest percentage of molecules in the excited-state is 15 percent of the total population. All excited-state transitions which are oriented at a relatively large angle to the molecular backbone are weak and are thus unlikely to be observed. In the ground state the weak transitions ($S_0 \rightarrow S_n,\ n > 1$) are observable due to the high concentration of molecules in the ground state ($N_0 \approx N$, where N is the total population). This large difference in population between the ground and excited state ($N_0 >> N_1$) is the reason why only strong excited-state transitions oriented parallel to the polymethine chromophore are observable. *Finally*, the energy level that both the ESA and fluorescence processes probe is the same relaxed S_1-state that is formed from the Franck-Condon excited state after vibrational relaxation. Our experiments, performed previously with the femtosecond nonlinear spectrometer [48], have shown that the formation of the vibrational structure of the ESA-spectrum in the visible region for typical PDs is complete in approximately 1 to 1.5 picoseconds. Therefore, this time can be considered as the time of excited-state geometry optimization adapting to the new excited-state charge distribution. During this time the valence angles and bond lengths can change their initial values leading to a change in the orientation of the polymethine chromophore. As a result, all

excited-state molecules are aligned parallel to this new orientation of the polymethine chromophore affecting both ESA ($S_1 \rightarrow S_n$) and fluorescence ($S_1 \rightarrow S_0$) transitions.

These three reasons explain why the anisotropy of the ground to excited-state transitions in PDs can be monitored by the ESA of a probe beam instead of being monitored by the fluorescence intensity. As for molecules that are not linear and possess more than one intense ground state transition (i.e. phthalocyanines or porphyrins) the analysis is not so straightforward and is currently being investigated.

4.5. Conclusion

We have described a detailed investigation of the fluorescence and ESA anisotropy spectra for a series of polymethine molecules with different substitutions of the polymethine chromophore and different lengths of the chain. It is found that in all polymethine molecules studied the excited-state transition dipole moments can be used for determining the orientation of the $S_0 \rightarrow S_n$ transitions instead of the fluorescence transition dipole moment ($S_1 \rightarrow S_0$ transition). The two-color polarization-resolved pump-probe ESA method allows us to resolve all features in the anisotropy behavior for polymethine dyes. Therefore, we conclude that the ESA anisotropy method represents a useful approach for linear conjugated molecules like the polymethine, which can be applied to cases in which the steady-state fluorescence anisotropy measurements cannot be used, for example, in cases of nonfluorescent (or low fluorescence quantum yield) molecules, which is typical for long wavelength absorbing dyes, or for solvents with low viscosity which decrease the anisotropy value due to reorientational diffusion. We are currently investigating if this method is applicable for other types of molecules.

A detailed quantum-chemical analysis of the changes in molecular geometry and electron density distribution in the ground and excited state has been performed and the key results were summarized. It was found from the quantum-chemical analysis that the deformations in the molecular geometry under excitation (from Franck-Condon to relaxed), accompanied by the changes in the valence angles and bond lengths, are responsible for the anisotropy changes from the theoretical value of 0.4 to the range of values of 0.3 - 0.38 for the $S_0 \rightarrow S_1$ transition (depending upon the dye). The conjugated vinylene bridge strongly affects the nature of the higher electron transitions leading to the unusual behavior of the excitation anisotropy function in PD2410.

CHAPTER 5:NATURE OF THE ELECTRONIC TRANSITIONS IN THIACARBOCYANINES WITH A LONG POLYMETHINE CHAIN

5.1. Introduction

In the past decades there have been several approaches developed to aide in the understanding of the nature of the electronic transitions in PDs. The first and simplest quantum-chemical theories, the Huckel molecular orbital method and the Kuhn free-electron or "metallic model", were modified to explain the deep color of PDs containing an extended chain of methine groups as the main component [72,73,74]. These theories were based on an alternation of the charge density along the chain, which was proposed by Konig [75]. The first experimental proof of this hypothesis was provided in 1963 by nuclear magnetic resonance spectroscopic measurements [76]. In 1966 all existing approaches were unified by S. Daehne into a theoretical concept of the existence of three ideal states of unsaturated organic compounds, the so called triad principle [77,78,79]. According to this principle, all conjugated organic compounds can be characterized by three ideal states: the aromatic, the polyene and the polymethine state.

It is known that polymethine molecules can be represented by two dominant resonance forms with positive charges at opposite ends of the chain. Therefore, each carbon-carbon (CC) bond can be characterized as a single bond in one form and a double bond in the other, which leads to the formation of a non-alternating structure in which each bond is considered a 1.5 instead of a 1 (single bond) or a 2 (double bond). Systematic x-ray structure analysis confirmed the predicted equalization of CC bond lengths [80]. According to the triad theory, there are two distinguishing properties of PDs: first of all, equalization of the single and double bond lengths and secondly the appreciable alternation of the positive and negative charges at the carbon

atoms. Excitation leads to a substantial change of the atomic charges, while the CC bond lengths remain practically unchanged. These structural features of the PDs are responsible for the strong first electronic transition $S_0 \rightarrow S_1$, which is accompanied by a considerable π-electron density transfer from the carbon atoms in odd positions to ones in the even positions. Therefore, PDs combine a maximum $S_0 \rightarrow S_1$ transition probability with relatively low transition energy. The absorption and fluorescence bands of polymethines can be shifted from the visible to the IR-region by lengthening of the polymethine chain or by introducing specific terminal groups which possess their own large π-electron systems. Currently, the long wavelength limit for the peak of the absorption in PDs is approximately 1600 nm [81].

In contrast to PDs, the related neutral polyenes represent another type of linear conjugated system that is characterized by considerable alternation of the CC double and single bond lengths and an equalization of the π-electron density along the conjugated chain. Excitation leads to a substantial change of CC bond lengths, while the atomic charges remain practically unchanged. Therefore, lengthening of the chain in the polyenes is accompanied by a much smaller red shift of their spectral bands as compared to PDs, so that their spectral limit is ~700-800 nm, which depends slightly on the constitution of the terminal groups [82].

Many experimental and theoretical studies have confirmed the triad theory which has led to a deeper understanding of the main photophysical and photochemical properties of unsaturated organic compounds, in particular PDs [83]. Also, this theory is the basis for studying structure-property relationships. However, the triad theory predicted for symmetric PDs with an infinite chain length that the bandgap should vanish and the molecules should exhibit metallic behaviour. The linear behaviour of the bandgap on the “effective” number of double bonds (including the

influence of the terminal groups) has been demonstrated by Bredas et. al. [84] and by Tolbert and Ogle [85] for short conjugated systems only. It was shown experimentally that by lengthening the polymethine chromophore the intensity of the $S_0 \rightarrow S_1$ transition decreases regularly and the bandwidth increases progressively. This effect for cyanine dyes was first reported by Brooker [86]. The structureless shape of the broad absorption band for other long polymethines was described by Tolbert and Zhao [87]. They assumed that the properties of the long conjugated linear systems could not be extrapolated from the short analogues, and that this spectral phenomenon is connected with the collapse of ground-state symmetry. The fundamental quantum-chemical investigation of the symmetry breaking phenomenon was performed by Hush et. al. for the simplest cyanines, the so called Brooker ions [64,65]. Their explanation was based on the formation of charged mobile defects (also referred to as solitons) in the doped linear conjugated polymers [88,89].

It was found by numerous investigators, both theoretically and experimentally, that the total charge (positive and negative) in the charged π-electron system is not delocalized uniformly along the polymethine chain, but instead is distributed at the π-centers as a wave of alternating positive and negative partial charges, i.e. as a soliton of the electron or hole type, respectively [64,65,90,91,92]. ^{13}C nuclear magnetic resonance spectroscopy measurements confirmed the π-electron density localization in the center of the chain with a decrease of the charges at the ends [90,91]. Quantum-chemical calculations performed for the linear conjugated molecules show that the width of the charge wave is of finite size, approximately 15-17 carbon atoms for an unsubstituted polymethine chain [64,65]. The peak of the soliton always corresponds to the region of equality of the CC bond lengths and is placed on this “geometrical” or “topological”

defect. Under certain conditions, if the width of the π-conjugated chromophore of the real molecule becomes comparable (or longer) than the width of the soliton, the charge maximum of this molecule, accompanied by a geometrical defect, could be shifted to one of the terminal groups. As a result, a symmetry breaking occurs leading to dramatic changes in the absorption spectrum, such as band broadening and a decrease in the intensity of the transition [87]. Recently Tolmachev et. al. investigated this effect for a series of thiacarbocyanines (from monomethine to hexamethine) and confirmed that the main reason for band broadening is the intramolecular charge transfer from one side of the dye molecule to the other [93].

Thus, there is not a simple correlation between the dependence of the spectral characteristics on the chain length. For a relatively short chromophore (inside of the cyanine limit) many properties of these molecules are well understood, but little is known about the nature of the transitions beyond the cyanine limit. Therefore, one of the goals of this chapter was to study the nature of the $S_0 \rightarrow S_1$ electronic transitions for near-IR absorbing PDs. For this purpose we performed a detailed experimental investigation and quantum-chemical analysis of PDs with different chain lengths, in particular, the tri- (PD2501) and penta-thiacarbocyanines (PD1659). PD1659 is shown in Figure 1.4 and PD2501 is shown below in Figure 5.1. PD2501 was synthesized for this work to have a shorter chain than PD1659, but to have identical benzothiazolium terminal groups unlike the other polymethines in this study. The chemical name of PD2501 is 3,3-dimethylthiatricarbocyanine p-toluenesulfonate.

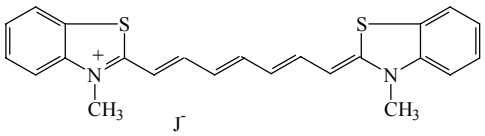

Figure 5.1: Molecular structure of PD2501

The experimental techniques used to investigate the PD molecules are:

(1) Linear absorption spectral measurements in solvents of different polarity.

(2) Femtosecond tunable polarization-resolved pump-probe measurements.

(3) ESA-spectrum and ESA- anisotropy measurements.

The analysis includes:

(1) Numerical fitting of the pump-probe measurements.

5.2. Excited-State Absorption Spectrum and Anisotropy Measurements

To measure the ESA spectrum of PD 1659 the femtosecond laser system described in Section 3.2.3 was used. The pump was set at 900 nm and the white-light continuum was measured from 400 – 800 nm with (signal) and without (reference) the pump to determine the nonlinear absorption signal. The probe was set at approximately a 13 picosecond delay to that of the pump beam, which is longer than the vibrational relaxation time, but shorter than the excited-state lifetime. The analysis to extract the absolute cross-section and shape of the ESA spectrum from the continuum spectrum with and without the pump is given in Reference [48], but will be

reviewed here. The linear (T_L) and nonlinear (T_{NL}) transmittance of the continuum is given by the following equations:

$$T_L(\lambda) = \exp[-\sigma_{01} NL] \tag{31}$$

$$T_{NL}(\lambda) = \exp[-\sigma_{01} N_0 L - \sigma_{1i} N_1 L] \tag{32}$$

where L is the sample length and σ_{01} and σ_{1i} are the ground- and excited- state cross-sections, respectively. N is the total population, which is the sum of the ground (N_0) and excited (N_1) state populations. The absolute cross-section was determined near the peak of the ESA spectrum (630 nm) using the open aperture Z-scan technique [43] using the EKSLPA picosecond laser system and OPG described in Section 4.2.1. This absolute cross-section can then be used to calibrate the ESA spectrum using the following equation:

$$\sigma_{1i}(\lambda) = \sigma_{01}(\lambda) - (\sigma_{01}(630nm) - \sigma_{1i}(630nm)) \frac{\ln[T_{nl} / T_l]\big|_{\lambda}}{\ln[T_{nl} / T_l]\big|_{630\,nm}} \tag{33}$$

where $\sigma_{01}(\lambda)$ is the ground-state cross section as a function of wavelength, $\sigma_{1i}(630)$ is the excited-state cross section obtained from the fitting of the open aperture Z-scan data. The ratio of the white-light continuum measurements as a function of wavelength is $\ln[T_{nl} / T_l]\big|_{\lambda}$ and $\ln[T_{nl} / T_l]\big|_{630}$ is this ratio at 630 nm. Equation (33) is derived by solving two forms of Eq. (32) simultaneously, the first as a function of wavelength and the second for the fixed wavelength of 630 nm (at which the Z-scan was taken) and solving for $\sigma_{1i}(\lambda)$.

The ESA anisotropy measurements were conducted using the technique developed in chapter 4. This method is ideal for the long chain polymethines due to the low fluorescence quantum yield. The lifetime of the first excited-state was measured with the femtosecond

polarization-resolved pump-probe technique to be approximately 60 picoseconds. The probe was at a wavelength of 620 nm and the pump was tuned over the range of 560 – 960 nm.

5.3. Experimental Results

5.3.1. Absorption Properties

Linear absorption spectra for PDs 2501 and 1659 in five solvents of different polarity: methanol, acetonitrile (ACN), ethanol, methylene chloride and o-dichlorobenzene are presented in Figure 5.2. As can be seen from this figure, PD 2501 exhibits a relatively narrow absorption band in all solvents, while the width of the band increases progressively as a function of polarity for PD 1659. This increase is mainly connected with the appearance of a broad shoulder on the short wavelength side of the absorption band. Also, the intensity of the long wavelength band decreases substantially with an increase of the chain length: extinction coefficients in ethanol are 21.3×10^4 $M^{-1}cm^{-1}$ (at peak position 761 nm) for PD 2501 and 6.6×10^4 $M^{-1}cm^{-1}$ (at 997 nm) for PD 1659. The polarity of the solvents can be characterized by their orientational polarizability (Eq. 28). Calculated Δf values range from 0.208 for o-dichlorobenzene to 0.308 for methanol. The absorption and emission bands can be altered by a spectral shift (red or blue) or in intensity change due to the solvent nature or composition; this is called solvatochromism [54]. It is well known that relatively short wavelength absorbing PDs exhibit classic nonpolar solvatochromism, which is consistent with a symmetrical ground and excited state charge distribution and small permanent dipole moments [54]. Nonpolar solvatochromism implies only a small red shift in the absorption and fluorescence bands is expected as a function of the index of refraction. In

contrast, absorption spectra of PD 1659 (Figure 5.2b) demonstrates a strong dependence on solvent polarity. An increase in solvent polarity leads to a substantial band broadening represented by the growth of the short wavelength shoulder. This is a strong indication of polar solvatochromism, which is typical for dyes that exhibit charge localization and a large permanent ground-state dipole moment [94]. From the analysis of the spectral data we were able to infer that PDs with a polymethine chain containing at least five methine groups may exist in the ground state in two charged forms with symmetrical and asymmetrical distributions of the charge density. Quantum-chemical calculations presented in Section 5.2 will validate this hypothesis.

Based on this hypothesis of the coexistence of two charged forms in the ground state, we separated the absorption spectra of PD 1659 into two bands and compared the dependence of the peak spectral position of each form as a function of the solvent polarity. In order to separate these two forms, we first fit the absorption spectra for PD 2501 in different solvents making the assumption that the shape of the spectrum is that of the symmetric form of PD 1659. Secondly, this function was then used in the fitting procedure for PD 1659 to determine the asymmetric form. The result for the polar solvent ACN is shown in Figure 5.3a. In this case, the integral ratio between the absorption of the asymmetric and symmetric forms is 5 to 1. Quantum-chemical calculations show that the $S_0 \rightarrow S_1$ transition dipole moments for both forms are comparable. Therefore, we can assume that the absorption band's integral ratio approximately corresponds to their concentration ratio. Inhomogeneity in the solvent shell distribution around dye molecules may be connected with the different permanent ground-state dipole moments for symmetric (0.7 D) and asymmetric (17.5 D) forms.

(a)

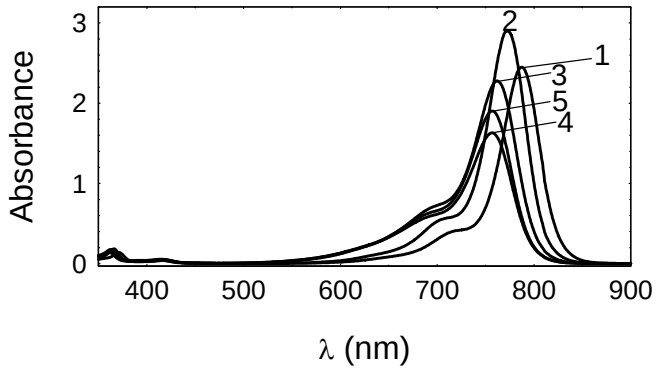

(b)

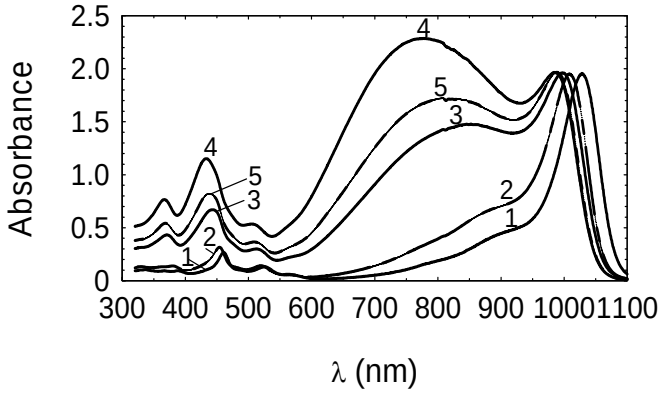

Figure 5.2: Absorption spectra for PD 2501 (a) and PD 1659 (b) in o-di-chlorobenzene (1), methylene chloride (2), ethanol (3), acetonitrile (4) and methanol (5).

The dependences of the peak spectral position as a function of solvent polarity for PD 2501 and for both forms of PD 1659 are shown in Figure 5.3b. As can be seen, for the symmetric form the spectral shift is only 300-500 cm^{-1} and for the asymmetric form is much larger, up to 1600 cm^{-1}. This solvent dependency reinforces the hypothesis that the absorption spectrum of PD 1659 consists of two charged forms with a symmetrical and asymmetrical charge distribution.

However, these measurements do not rule out the possibility that the short wavelength shoulder could be connected with a higher excited-state transition, for example the $S_0 \rightarrow S_2$ transition, thus disproving our hypothesis. The next section will discuss experiments which show that the broad absorption band in the range 600 – 940 nm is connected with only the $S_0 \rightarrow S_1$ transition.

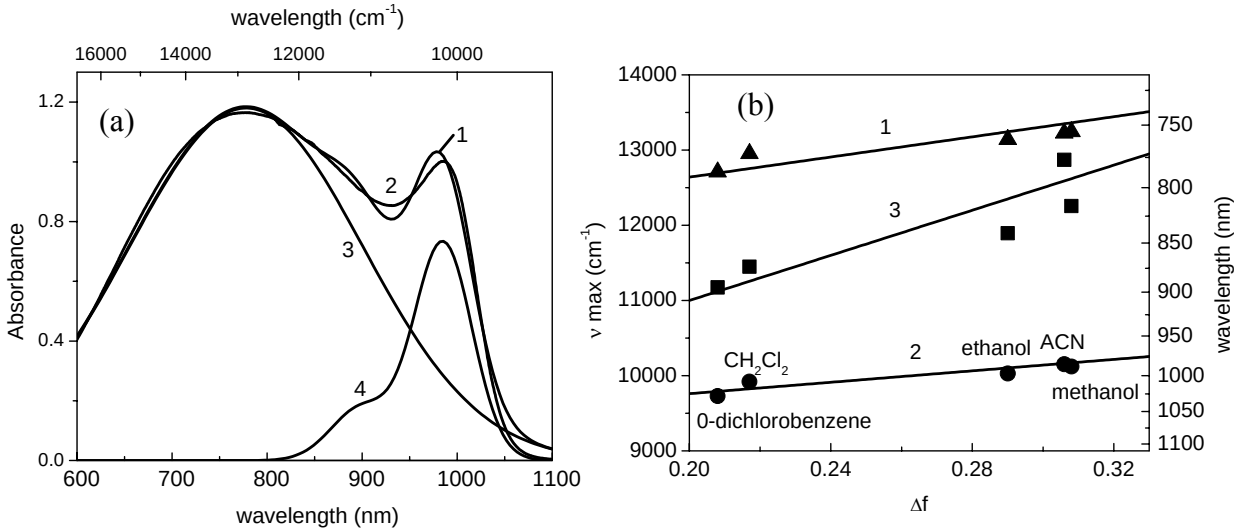

Figure 5.3: (a) Separation of the absorption spectra of PD 1659 in ACN on two absorption bands: 2 – experiment; 1 – fitting curve: $y=1.18\exp[-0.0000331(x-778)^2)+0.73\exp(-0.000531(x-985)^2]+0.175\exp[-0.00049(x-899)^2]$; 3 – asymmetric form $y=1.18\exp[-0.0000331(x-778)^2]$ and 4 – symmetric form $y=0.73\exp[-0.000531(x-985)^2]+0.175\exp[-0.00049(x-899)^2]$. (b) Dependences of peak positions on solvent polarity for PD 2501 (curve 1) and for both forms of PD 1654: symmetric form (curve 2) and asymmetric form (curve 3).

5.3.2. Excited-State Absorption and Anisotropy Properties

This method of determining the spectral position of the excited-states using a pump-probe method is based on the understanding that in polymethine molecules the ESA transition dipole moments (in particular, the most intense $S_1 \rightarrow S_5$ transition) can be used for determining the

orientation of the $S_0 \rightarrow S_n$ transitions instead of the fluorescence transition dipole moment ($S_1 \rightarrow S_0$) as discussed in chapter 4.

Figure 5.4 shows the ground state and ESA spectrum which was obtained with a 120 fs (FWHM) excitation pulse at 900 nm and a 117 fs (FWHM) white light probe pulse, delayed by 13 ps with respect to the excitation pulse, over the spectral range of 400 - 800 nm. For the first time we have observed an excited-state cross section that is larger (≈ 3 times) than that of the ground state at the peak spectral position, while the integrated areas of their absorption bands are nearly the same. This result needs additional investigation due to the fact that oscillator strength in the excited-state is nearly equivalent to that in the ground state, and its implications for nonlinear optical applications such as optical limiting. Also, it is important to note that the excited-state cross-section is 6.3×10^{-16} cm^2 at 615 nm (peak ESA position), which is comparable to the largest measured results obtained by us [24] and described in the literature [95]. Figure 5.4 also shows the ESA anisotropy spectrum which gives us information about the orientation of the ESA transition dipole moment relative to the polymethine chromophore (or $S_0 \rightarrow S_1$ transition). As seen from the figure, the anisotropy value R_{PP} is relatively high: $R_{PP} = (0.32 \pm 0.07)$ and approximately constant over the spectral range of 600 - 920 nm. This indicates that there are no transitions oriented at a large angle (> 20°; typically for polymethines the $S_0 \rightarrow S_2$ transition is oriented at an angle of greater than 50° [62]) to the polymethine chromophore within this spectral range. Therefore, we can conclude that this broad absorption band is connected only with the $S_0 \rightarrow S_1$ transition along the molecular backbone.

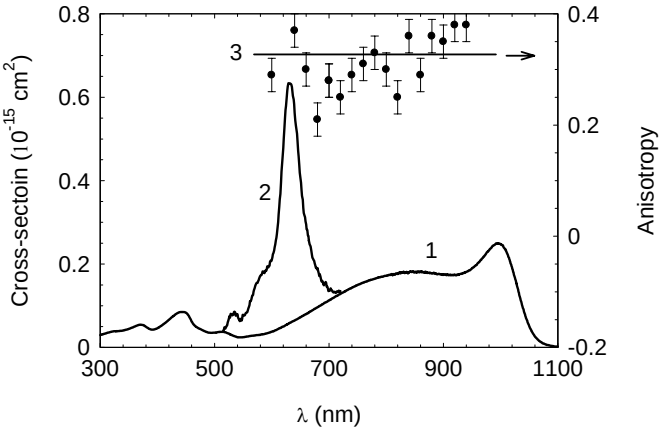

Figure 5.4: Ground state absorption (1), ESA-spectrum (2) and ESA-excitation anisotropy spectrum (3) for PD 1659 in ethanol.

5.4. Discussion

As in Chapter 4, this section will summarize the quantum chemical calculations, which were performed by Olga Przhonska and colleagues at the Institute of Physics and the Institute of Organic Chemistry, National Academy of Sciences. A complete treatment of the quantum chemical calculations can be found in reference [96]. The intent of this section is to demonstrate the impact of the experimental results on the understanding of the nature of the transitions in thiacarboycanines and particular the symmetry breaking effect.

5.4.1. Methodology of Quantum Chemical Calculations

Quantum-chemical calculations were performed with the goal of understanding the main features of the electron density distribution in the ground and excited states for the thiacarbocyanines of different chain lengths.

The equilibrium molecular geometry in the ground state and the charge distribution for the dyes in the ground and excited states is performed employing the semi empirical AM1 method (MOPAC package, gradient < 0.01 kcal/mol and gradient values of 2-3 kcal/mol). Additionally, the charge distribution and electron transition energies were calculated in INDO/S and PPP (Parr-Pariser-Pople) approximations (with spectral parameterization) using the 100 lowest singly excited configurations. It was found that the calculated amplitudes of the charge waves are different for different methods (AM1, ZINDO/S or PPP). However, all methods predict similar trends for the behavior of the charge waves as described below.

5.4.2. Quantum Chemical Calculations for the Model Chromophore and the Simplest Polymethine Molecule

In this section we describe the quantum-chemical calculations on the ground state electronic properties for the model chromophore and the simplest polymethine molecule (Brooker ion). The model structure is given as:

$$\mathbf{H_2C^+ = CH– (CH = CH)_{20} –CH_2} \tag{34}$$

and the simplest PD, the so called Brooker ion, with the same chain length is:

$$\mathbf{H_2N^+ = CH– (CH = CH)_{20} –CN_2} \tag{35}$$

The charge wave and bond lengths are calculated for the model chromophore and Brooker ion for two reasons. The first reason is to compare our quantum-chemical calculations to previous published results. Secondly, the results from the model chromophore provide information about the width of the solitonic wave, as defined in the introduction. By comparing the width of the solitonic wave to the width of the charge distribution in the carbocyanine molecules we can

determine if symmetry breaking will occur. The main result from the quantum-chemical calculations for the model chromophore is that length of the soliton is the same chain length of 15-17 carbon atoms as predicted previously [64,65]. The main result for the Brooker ion is that its' π-conjugated chain becomes comparable (or longer) than the length of the soliton leading to the possibility of a symmetry breaking effect.

5.4.3. Quantum Chemical Calculations for the Thiacarbocyanines

Quantum-chemical calculations were performed with the goal of understanding symmetry breaking effects in the electron density distribution in the ground and excited states of thiacarbocyanines, which have chain lengths from monomethine (n = 1) to hexamethine (n = 6).

In order to model the coexistence of two forms in the quantum-chemical analysis the following procedure was performed. First, the optimization process was performed for all the dyes of various chain lengths at gradient values < 0.01 kcal/mol starting from the initial ideal molecule with equalized CC-bonds. This gives a single solution having only one form with the symmetrical distribution of the electron density for molecules up to tetracarbocyanine (n = 1 – 4). For the longer PDs (n = 5, 6) this procedure led regularly to the formation of a more stable form of the electron density, which was asymmetrical. Secondly, in order to model the formation of the symmetric form for PDs with n = 5, 6 the optimization process was performed with relatively large gradient values of 2-3 kcal/mol. This allowed us to get a solution for the symmetrical charge distribution form for the long PDs. For the quantum-chemical calculations of the excited-state electron density distribution only the Frank-Condon state was considered.

The calculated Δq-functions for the series of thiacarbocyanines in the ground and first excited state are presented in Figure 5.5a (n = 1 - 4) and Figure 5.5b (n = 5, 6).

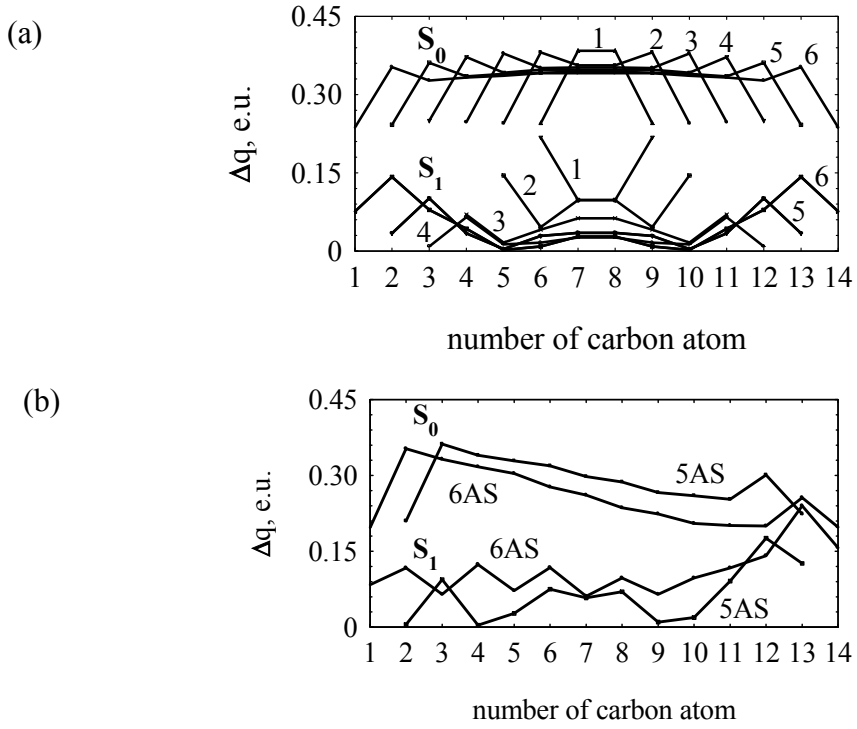

Figure 5.5: (a) Ground- (S_0) and excited-state (S_1) Δq-functions for the series of the thiacarbocyanines with the different chain lengths (n = 1 – 6), symmetric forms only. (b) Ground- (S_0) and excited-state (S_1) Δq-functions for the thiacarbocyanines with the chain length n = 5 – 6, asymmetric forms only. S and AS are related to symmetric and asymmetric forms.

The salient points of the quantum-chemical analysis of the charge distribution of the thiacarbocyanines dealing with symmetry breaking are summarized below:

(1) Symmetry breaking for the thiacarbocyanines in the ground state occur at n = 5. For the Brooker ion, the calculations show the appearance of the asymmetrical form in the

ground state only when $n \geq 8$, i.e. symmetry breaking depends not only on the chain length itself, but on the total "effective" length of the chromophore, including the π-electron systems of both the terminal groups.

(2) Symmetry breaking for the thiacarbocyanines in the excited-state can occur for relatively short chain lengths as compared to the ground state symmetry collapse due to the appearance of two minima in the symmetric molecular form (as seen in Figure 5.5a for n=2 and higher) that can lead to instability in the charge wave.

(3) The magnitude of the amplitudes of the Δq-function in the excited state is appreciably lower than in the ground state for the entire series including the asymmetric forms. And the shape of the bond alternation is substantially distorted when $n \geq 5$. It is important to note that the Δl functions for the asymmetric forms can reach a considerable magnitude (≈ 0.08 Å), which is close to the amplitude of the bond length alternation in polyenes [92]. Quantum-chemical calculations performed in the framework of the Huckel approximation results in the reverse of the π-electron density at the carbon atoms, i.e. the sign of the charge in the excited state is opposite to that of the ground state

(4) The most important point is that the symmetric form does not show a saturation effect even for hexacarbocyanine ($n = 6$), while the asymmetric form saturates at $n = 4$. These calculations show the trend of band broadening and a decrease in the intensity of the transition, which was observed experimentally.

5.5. Conclusion

We have performed a detailed experimental investigation and quantum-chemical analysis of PDs with different chain lengths, in particular, the tri- (PD 2501) and penta- (PD 1659) thiacarbocyanines. It is found that the relatively short wavelength absorbing PD 2501 exhibits classic nonpolar solvatochromism, consistent with symmetric ground and excited state charge distributions and small permanent dipole moments. In contrast, the absorption spectrum of PD 1659 demonstrates a strong solvent dependence. An increase in solvent polarity leads to substantial band broadening represented by a growth of the short wavelength shoulder. This is a strong indication of polar solvatochromism, which is typical for dyes that exhibit charge localization and a large permanent ground-state dipole moment. Exited-state anisotropy measurements confirmed that this broad absorption band is connected with only the $S_0 \rightarrow S_1$ transition. For the first time we have observed an excited-state cross-section that is larger (≈ 3 times) than the ground state cross-section at the peak spectral position.

The analysis of the spectral data enabled us to infer that the PDs with the long polymethine chain may exist in two charged forms in the ground state with symmetrical and asymmetrical distributions of the charge density. The quantum-chemical calculations provide an additional basis for this hypothesis. Experiments show that the less polar solvent, o-dichlorobenzene, primarily stabilizes the symmetric form. An increase of solvent polarity leads to an increase in the concentration of the asymmetric form. In the most polar solvent used in this study, ACN, both the asymmetric and symmetric forms can co-exist, and from our calculations exist in the concentration ratio of 5 to 1.

A detailed quantum-chemical analysis performed by Olga Przhonska and colleagues was performed with the goal of understanding the main features of the electron density distribution in the ground and excited states for the thiacarbocyanines with different chain lengths. We have come to the conclusion that an increase in the length of the polymethine chromophore leads to symmetry breaking and the appearance of an asymmetric form. For thiacarbocyanines the symmetry breaking effect was predicted and observed at n = 5. Our explanation is based on the previously proposed theoretical concept of the formation of a solitonic wave in the linear conjugated polymethine chromophores. We assume that if the width of the solitonic wave (15-17 carbon atoms) exceeds the dimensions of the dye molecule, then only the symmetric charge distribution can be detected. In this case, PDs show the typical spectral behavior such as a narrow and intense absorption band, nonpolar solvatochromism, a red shift of the band with lengthening of the chain, etc. If the width of the soliton becomes comparable to the length of the polymethine chain then both the symmetrical and asymmetrical charge distribution can be detected as a function of the solvent properties. This leads to dramatic changes in the spectral characteristics of the IR dyes. The nature of the $S_0 \rightarrow S_1$ transition for the symmetric form is connected with the charge transfer between neighboring atoms in the chain. The nature of the same transition for the asymmetric form is different. Due to charge localization it is connected mostly with the transfer process from one part of the chromophore to another and these dyes show limitations in the peak absorption positions.

CHAPTER 6: FEMTO- TO NANOSECOND NONLINEAR SPECTROSCOPY OF POLYMETHINE MOLECULES

6.1. Introduction

In this chapter we discuss experiments designed to determine key molecular parameters for nanosecond optical limiting applications. We have narrowed the set of polymethine molecules we are examining down to five that cover the di- to tetracarbocyanine chain length: PD2350, PD1952, PD2410, PD3428, and PD824 (shown in Figure 1.4). An emphasis is placed on the tricarbocyanines, which differ by the bridge structure, and were discussed in chapter 4. PD 3428 has an un-substituted (or un-bridged) polymethine chromophore. PD 1952 has a 5-membered cycle (or dimethylene bridge), and PD 2410 has a 5-membered cycle with an extra double bond (vinylene bridge). This subset of molecules will allow us to develop relationships between the ESA properties of the molecules and the conjugation length and bridge structure. Also, all molecules were studied in up to eight different host solvents (depending on solubility) to provide an adequate base to investigate specific and nonspecific solvent effects on excited-state absorption and dynamics. The eight solvents are comprised of four protic (hydrogen bond donors (HBD)) and four aprotic (non-HBD) solvents. The four protic solvents are the alcohols: ethanol, methanol, butanol, and pentanol. The four aprotic solvents are: N,N-dimethyl formamide (DMF), N-methyl formamide (MF), Dimethyl-sulfoxide (DMSO), and Propylene Carbonate (PC). The key parameters for each solvent are given in Table 6.1. A complete linear absorption analysis was performed for each molecule in all solvents. This analysis includes determining the molar extinction coefficient at the peak of the linear and nonlinear absorption spectrum, and solvatochromic shifts. An accurate measurement of these material parameters is

crucial for determining nonlinear optical parameters. The absorption and fluorescence experiments are discussed in Section 6.2.1.

Table 6.1: Solvent Parameters

Solvent	Viscosity (cp)	(τ_D) Dielectric relaxation time (ps)	n	ε_0	Δf
Protic					
Ethanol	0.55	56	1.326	32.6	0.310
Methanol	1.06	139	1.361	24.3	0.289
Butanol	2.59	482	1.399	17.4	0.263
Pentanol	3.51	727	1.410	14.8	0.252
Aprotic					
DMF	0.80	10	1.431	38.3	0.275
MF	1.65	170	1.432	181.6	0.289
DMSO	2.00	21	1.478	46.5	0.263
PC	2.53	43.1	1.419	65.0	0.287

n: index of refraction, ε_0: dielectric constant, Δf: polarity (defined by Eq. 28)

Making meaningful comparisons between the absorption properties of polymethine molecules of different conjugation lengths or bridge structures is not trivial. As can be seen from the linear absorption spectra shown in Figure 1.5, that a red shift of the linear absorption spectrum occurs as the conjugation length is increased or the bridge structure changed. Thus, it is inadequate to study the nonlinear absorption properties of polymethines at the same wavelength to be able to make direct comparisons between molecules of different conjugation lengths. It is necessary to measure the ESA spectrum of each molecule and conduct the nonlinear absorption measurements at the peak spectral position. This was achieved by using the technique discussed in Section 5.3.2 to measure the ESA spectrum of each molecule, and the results will be covered in Section 6.3.2.

In Chapter 3 the initial experiments on excited-state dynamics were discussed. In this chapter a more complete description is developed in Section 6.3.3 using the expanded solvent base. The expanded solvent base allows us to get a clear picture of the forces acting on the solute molecule, such as: hydrogen bonding [97], polarity [54], dielectric friction (related to dielectric relaxation time) [98], slip versus stick boundary conditions [97,99], and viscosity effects. The SED (Stokes-Einstein-Debye) model used in Chapter 3 also assumes a spherical shape for the molecules, which is not true for the polymethines. We will examine the modification to the SED model proposed by Perrin [100] that takes into account ellipsoid shaped molecules.

With the exception of Chapter 2 the previous work concentrated on using nonlinear optical experiments to measure linear molecular properties such as dynamics and spectral positions of excited state levels. The work in this chapter will focus on using the concepts developed in the previous chapters in conjunction with standard nonlinear optical measurement techniques such as picosecond and nanosecond Z-scans [43], along with picosecond and nanosecond optical limiting to form a complete picture of nonlinear absorption properties along with the excited-state dynamics. The Z-scan experiment will be described in detail in Section 6.2.3. The results of these experiments allow us to develop an energy level structure for the polymethines, which accurately predicts nonlinear absorption properties from the pico- to the nanosecond time regime. From this model we will be able to identify the key molecular parameters for improved nanosecond optical limiting. Furthermore, since each molecule will be studied at its peak nonlinear absorption spectral position, this allows for a meaningful comparison between the effects of conjugation length and bridge structure on these molecular parameters.

6.2. Experimental Methods

6.2.1. Linear Absorption and Fluorescence Measurements

The goal of the linear absorption measurements is to accurately determine the ground state cross-section (σ_{01}) at the peak spectral position and at the wavelength the nonlinear optical measurements will be conducted (peak ESA spectral position) for each molecule in every solvent. Due to the limited dynamic range of the spectrophotometer this cannot be accomplished in a single set of measurements.

The quantity measured by the spectrophotometer is the optical density (OD) of the sample, and is given by the following relationship:

$$OD(\lambda) = \log[1/T(\lambda)] = \varepsilon(\lambda) l C_{on} \tag{36}$$

where ε(λ) is the molar (decadic) absorption coefficient (in liters mol^{-1} cm^{-1}), C_{on} is the concentration (in mol $liters^{-1}$), and l is the path length. The ground state cross-section is related to the molar absorption coefficient by:

$$\sigma = \frac{2.303\varepsilon}{N_a} = 3.825 \cdot 10^{-21} \varepsilon \tag{37}$$

where N_a is Avogadro's number. This relationship comes from the fact that the OD and ε(λ) are derived from the decadic (i.e. $\log_{10}$) absorption coefficient and the ground state cross-section is defined by the Napierian (i.e. $\log_e$) absorption coefficient. Accurate measurements of ε(λ) at the peak spectral position are performed by measuring the optical density (OD) of a sample of known concentration. The sample of known concentration is prepared by dissolving a measured amount of dye powder into a given amount of solvent, which gives grams per liter. This is then

converted to moles per liter by dividing this quantity by the molar weight, which is given as the product of the molecular weight, atomic mass unit, and Avogadro's number. The molecular weight of the molecules includes the anion, and is calculated using the ISIS DRAW program. Secondly, the sample of known concentration is then measured by a dual arm (signal and reference) Varian Cary 500 spectrophotometer to determine the Optical Density (OD). From this first measurement three dilutions of the sample are produced to give ODs of approximately 0.1, 0.075, and 0.05 to avoid aggregation of the sample. These three measurements then give us three values of $\varepsilon(\lambda)$, and if all are within ten percent of each other we take the average for the final value of $\varepsilon(\lambda)$.

Once the ground state cross-section at the spectral peak is determined it is possible to determine the cross-section at the wavelength, λ_{meas}, at which the nonlinear optical measurements will be performed. Because the nonlinear optical measurements are performed at wavelengths that are several 100 nm from the peak spectral position the ground state cross-section at this wavelength is approximately three orders of magnitude smaller than at the peak. To get an accurate measurement of this cross-section a series of linear absorption measurements are performed. First, a sample with an OD at the peak spectral position of approximately 1 to 1.5 is produced. A second wavelength, between the peak and λ_{meas}, is chosen as a reference. The OD at the reference wavelength is conducted and the peak, which has an OD of about 0.1. A new sample, more concentrated, is then prepared that has an OD between 1 and 1.5 at this reference wavelength, which is then related to either a second reference wavelength or to λ_{meas} if it has an OD of at least 0.1. From this series of measurements the ground-state cross-section at the wavelength the nonlinear optical measurements will be conducted can be determined within an

accuracy of 5%, which is determined from repeated measurements. The results of these measurements will be discussed along with the picosecond measurements in Section 6.4.3.

The main goal of the fluorescence measurements is to study the solvent-induced shifts of the spectral position of the peaks of both the absorption and fluorescence spectra, which are known as solvatochromic shifts. Knowing how different solvents affect both the absorption and fluorescence spectrums gives us insight into the specific and nonspecific solvent effects, which are needed to make accurate predictions of the orientational diffusion times. If only nonspecific (Van der Waals) interactions are affecting the molecule, the solvatchromatic shifts should follow the Lippert-Mataga Eq. [54], which is given by:

$$\Delta v = \nu_a - \nu_f = \frac{2}{hc}(\Delta\mu_{eg})^2 a^{-3}\Delta f + const. \tag{38}$$

where h is Planck's constant, c is the speed of light, a is the Onsager cavity radius in which the solute resides, $\Delta\mu_{eg}$ is the change in the permanent dipole moment from the ground to excited state, Δf is the orientational polarizability of the solvent given by Eq. 28, and ν_a and ν_f are the peak spectral position of the absorption and fluorescence spectra in wavenumbers (cm^{-1}), respectively. If the shift ($\Delta\nu$) is a nonlinear function of polarity (Δf) then some type of specific solvent effect (e.g hydrogen bonding) is present, and since a broad range of solvents is being used it is possible to narrow down the type of effect. The results of these experiments along with the excited-state dynamics of the polymethines will be discussed in Section 6.4.2.

6.2.2. Z-Scan Technique

The Z-scan is a nonlinear optical experiment in which the irradiance (or fluence) is continuously varied from the linear regime of the sample to an irradiance high enough to induce nonlinear effects and then back to the linear regime. This is accomplished by translating the sample along the axis of a focused Gaussian beam as shown in Figure 6.1. For a given pulsewidth the peak irradiance is determined by the input energy and the beam waist. The size of the beam waist also determines the rate of change of the irradiance, which is proportional to (ω^{-2}(Z)), and is given as:

$$\omega^2(Z) = \omega_0^2(1 + (Z / Z_0)) \tag{39}$$

where Z_0 is the Rayleigh range and is defined as:

$$Z_0 = \frac{n\pi\omega_0^2}{\lambda_0} \tag{40}$$

where n is the index of refraction in the medium. The beam waist is measured using the techniques discussed in Section 2.2.2. A schematic of the Z-scan setup is shown in Figure 6.1. The input energy is varied using the half-waveplate and polarizer. A beam splitter (BS_1) placed before the first lens (L_1) redirects a portion of the energy to a reference detector (D_R) which has its voltage calibrated to the energy in front of the sample. A window (maximum and minimum allowed voltage the data acquisition system will accept) of approximately 5% is placed on the reference detector so that the fluctuation in the energy of the beam is known. The second lens (L_2) is 2 inches in diameter, which is used as a collection lens for the transmitted energy onto the signal detectors (D_{S1}, D_{S2}). After L_2 a second beam splitter (BS_2) which divides the energy between two signal detectors. Ratios of the signal detectors to the reference detector, are

recorded. Detector D_{S1} has an aperture placed in front of it, which clips some of the beam hitting the detector (transmits approximately 40 %), to record what is referred to as a closed aperture Z-scan. This type of Z-scan is sensitive to both nonlinear absorption and nonlinear refraction effects. Detector D_{S2} collects all the transmitted energy and is referred to as an open aperture Z-scan. Provided the sample is thin, [43] this type of Z-scan is only sensitive to nonlinear absorption effects, and is the method primarily used throughout this chapter. The results of the Z-Scans along with energy level models and fitting for the picosecond and nanosecond regime will be shown in Sections 6.3.3 and 6.3.4, respectively.

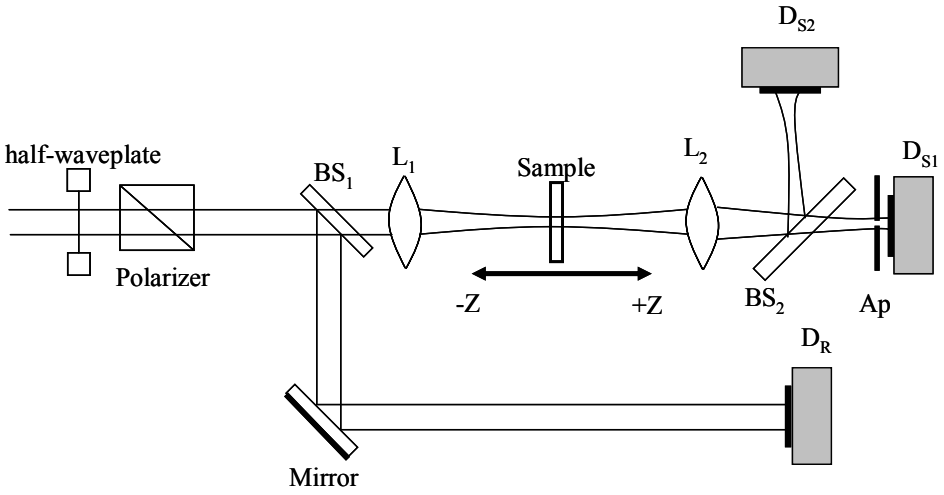

Figure 6.1: Schematic of Z-Scan experiment. BS_1 and BS_2: 50-50 Beam Splitter, L1: 1 inch 15 cm focal length lens, L2: 2 inch 10 cm focal length lens, Ap is the aperture closed to 40% of total energy. D_{S1} is closed aperture signal detector; D_{S2} is open aperture signal detector, and D_R is the reference detector. –Z to +Z describes the movement of the sample during a measurement.

The picosecond Z-scans are conducted with the laser system and OPG described in Section 4.2.1. The nanosecond measurements are performed with a Continuum Powerlite 9010, which is Nd:YAG, Q-switched by a Pockels' cell producing a 7ns (FWHM) pulsewidth operating at a 10 Hz repetition rate. The repetition rate can be changed by adjusting the switching of the pockels cell. Also, by altering the Q-switch the pulsewidth can be increased. A longer pulsewidth of 21 ns (FWHM) is used for a set of limiting experiments in order to study Trans-Cis state conformations, which will be discussed in Section 6.3.4. The laser also uses injection seeding with a diode laser to maintain a single longitudinal mode. The laser can be frequency-doubled to 532nm using a Type I KDP crystal, which reduces the pulsewidth to 5ns (FWHM), or frequency-tripled (355nm) using a second Type I KDP crystal for pumping an optical parametric oscillator (OPO). The OPO is a Continuum Sunlite EX, which is based on a BBO crystal pumped by the 355 nm light. There are also two BBO single-pass optical parametric amplifiers (OPA) that produce energies in the millijoule range over the tuning range. The OPO beam is spatially filtered both intracavity and externally to obtain a Gaussian beam profile. The OPO signal beam is tunable from 450nm to 710nm, and has a pulsewidth of 3-4ns (FWHM). The idler beam is tunable from 710nm to 1682nm.

6.3. Experimental Results

6.3.1. Excited-State Absorption Spectra

The ESA spectra for the five polymethine molecules studied in this chapter were measured using the same method and laser system described in Section 5.2. The ESA spectrum was measured for each molecule in every host solvent it was soluble in, except for PD2410 which was measured in only one solvent (methanol). The ESA spectra for PD2350 and PD824 in all solvents are shown in Figure 6.2. These experiments are the first to be performed to determine the peak in the ESA spectrum for the nonlinear optical characterization measurements (Z-scans). Two key observations can be made from Figure 6.2 concerning the nonlinear optical measurements. First of all, the ESA spectrum of both dyes exhibits two peaks, which means we have a choice of wavelengths at which to perform the nonlinear optical measurements. A possible explanation for the two peaks will be discussed in Section 6.4.1. We have chosen to always perform the measurements at the ESA peak closest to the linear absorption maximum due to the larger ground state cross-section. The second characteristic of the ESA spectrums is that no shift of the ESA spectra occurs as a function of solvent. Therefore, for a specific dye a single wavelength can be used for that dye in all the host solvents thus simplifying the nonlinear optical characterization measurements. PD3428 and PD1952 exhibit the same trend as shown in Figure 6.2. The analysis of the ESA spectra is given in Section 6.4.1.

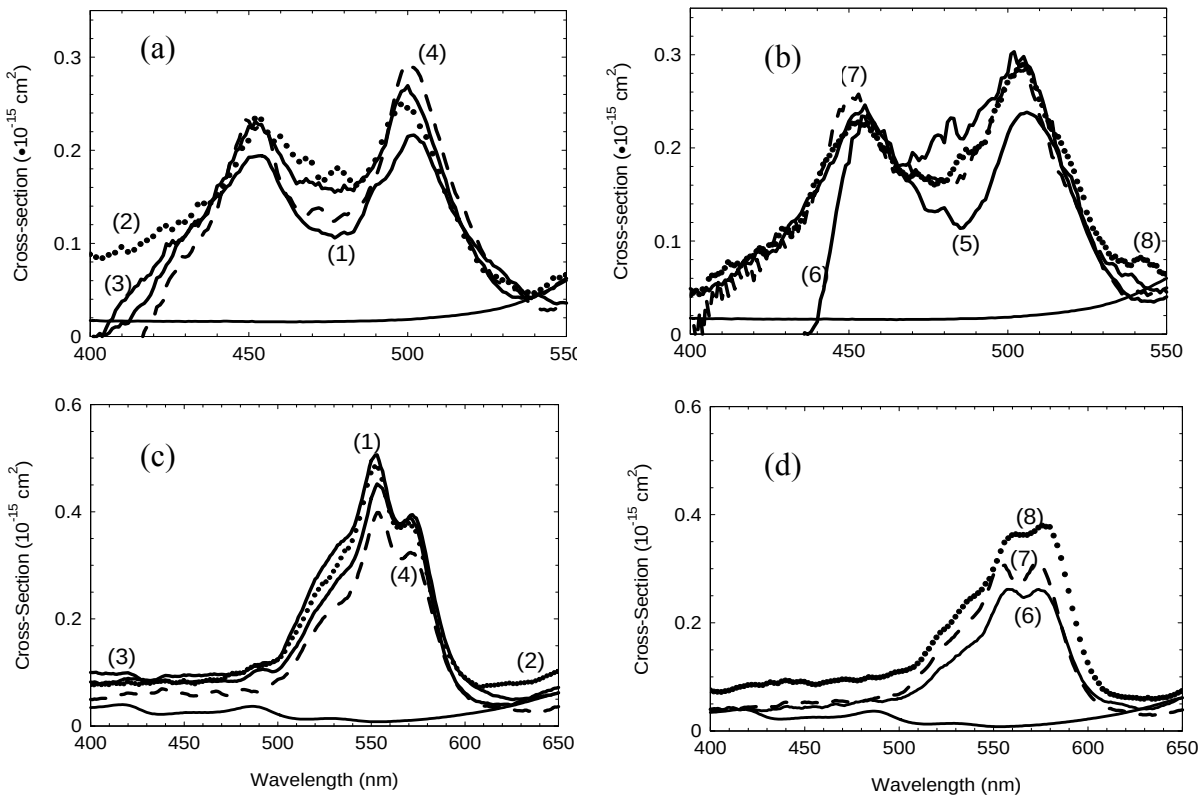

Figure 6.2: ESA Spectrafor PD2350 (shown in (a) and (b)) and PD824 (shown in (c) and (d)) in all soluble solvents: (1) methanol, (2) ethanol, (3) butanol, (4) pentanol, (5) MF, (6) DMF, (7) PC, (8) DMSO. The ESA cross-sections were determined from picosecond Z-scan measurements discussed in section 6.3.3.

6.3.2. Two-Color Picosecond Polarization Resolved Pump-Probe Method

In this section the excited state dynamics for the five polymethines in up to eight host solvents are discussed. This work builds on the initial ESA dynamic analysis performed in Chapter 3, and uses the same techniques but is performed with the two-color picosecond polarization-resolved pump-probe method described in Section 4.2.2. The two-color method is advantageous over the degenerate measurements because it is easier to produce large ESA

signals by tuning the pump wavelength into the linear absorption band while keeping the probe wavelength fixed (532 nm) near the ESA spectral peak. Also, the two-color method reduces or eliminates spurious signals which compromise the signal to noise ratio. The main factor which reduces the signal to noise is scattering of the intense pump beam into the weak probe, which can be eliminated using wavelength selective filters in front of the signal detector. The second noise factor which is experienced in the degenerate experiment arises when the pump and probe are temporally overlapped in the sample and coherent coupling [57] between the pump and probe occur. In the nondegenerate experiment the difference in the pump and probe wavelength is at least 100 nm, thus eliminating the coherent coupling effect.

The analysis performed in Chapter 3 compared the experimentally measured orientational diffusion times to those predicted by the SED model (equation 29) and the difference between experiment and theory was attributed to a solvent shell surrounding the solute molecule. But as noted in the introduction, only two and at most three solvents were investigated in this analysis, which is insufficient to determine if other solute-solvent interactions are responsible for this discrepancy. Therefore, we have expanded the solvent base to the ones discussed in the introduction, which will allow us to obtain a good grasp on the solute-solvent interactions.

We have also adopted a global fitting method [101] that fits all three experimentally measured curves simultaneously ($\Delta T_{\parallel}, \Delta T_{\perp}$, and ΔT_{ma}) using the software package Microcal™ Origin® Version 6. This has a distinct advantage over the previous method of fitting the curves individually not only in the reduction in error of the target variables, specifically the orientational diffusion time, but also in the amount of time it takes to perform the fitting. Figure 6.3 shows the experimental data with fittings for all five dyes in different host solvents.

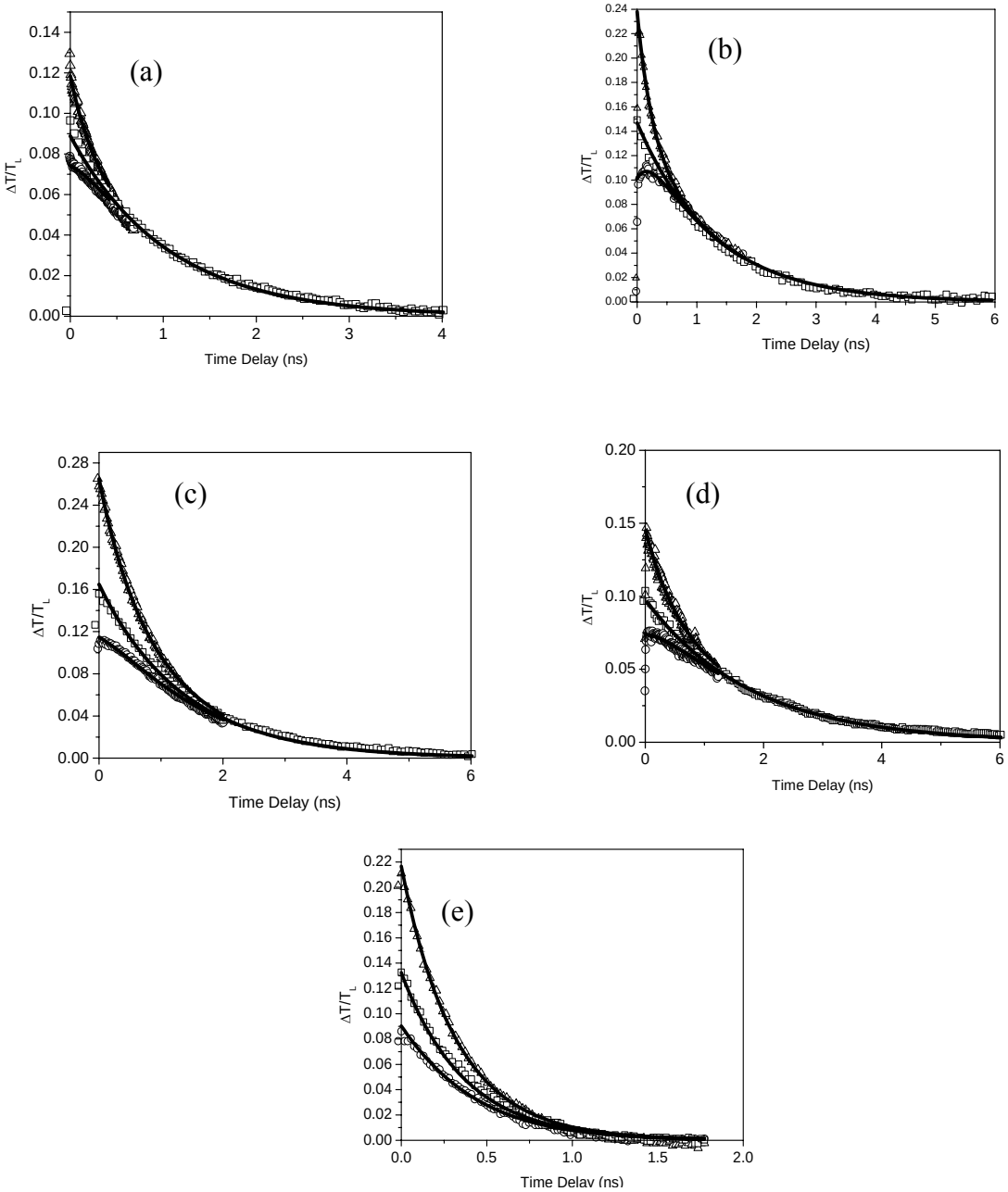

Figure 6.3: Pump-probe data and fittings for (a) PD2350 in ethanol, (b) PD1952 in DMF, (c) PD3428 in pentanol, (d) PD2410 in butanol, (e) PD824 in DMSO.

6.3.3. Picosecond Z-Scans and Optical Limiting Results

The goal of the picosecond experiments is to determine the molecular parameters which hinder optical limiting in the picosecond regime and how conjugation length and solvent affect these parameters. To do this, energy level models were developed which fit both the Z-scan and optical limiting experiments. These models may actually be the most important information gained from this section since they are the base model for the nanosecond experiments. In the nanosecond regime the models are inherently more complicated due to the long pulsewidth that is sensitive to nanosecond processes (such as triplet states and cis-trans conformations) in the polymethines, whereas the picosecond measurements are insensitive to these long processes. From the picosecond experiments we will determine the first and higher excited-state cross-sections along with higher excited-state dynamics of the five molecules under study. In this section we will describe the results of the experiments as well as the energy level models.

The first experiments carried out are low energy Z-scans in which a three-level all singlet energy level structure is used to model the results. This model is shown in Figure 1.1. The Z-scans are performed at the peak of the ESA spectrum, determined in Section 6.3.1, and from them we determine the excited-state cross-section (σ_{12}, or the ratio α defined in Chapter 2). Figure 6.4 shows the experimental results for the Z-scans of each molecule in a different host solvent with numerical fits using the three-level all singlet model. The linear transmission of all samples is between 80% and 90%. The measurements spanned an energy range of 7 nJ (Fluence: $1 \cdot 10^{-3}$ J/cm^2, Irradiance: 39.1 MW/cm^2) to 112 nJ (Fluence: $14.7 \cdot 10^{-3}$ J/cm^2, Irradiance: 127 MW/cm^2) and maximum change of transmission of 25%. The excited state cross-sections along

with all measured ground state cross-sections, from the linear absorption analysis, for every dye in all solvents are summarized in Table 6.4, which is discussed and shown in Section 6.4.3.

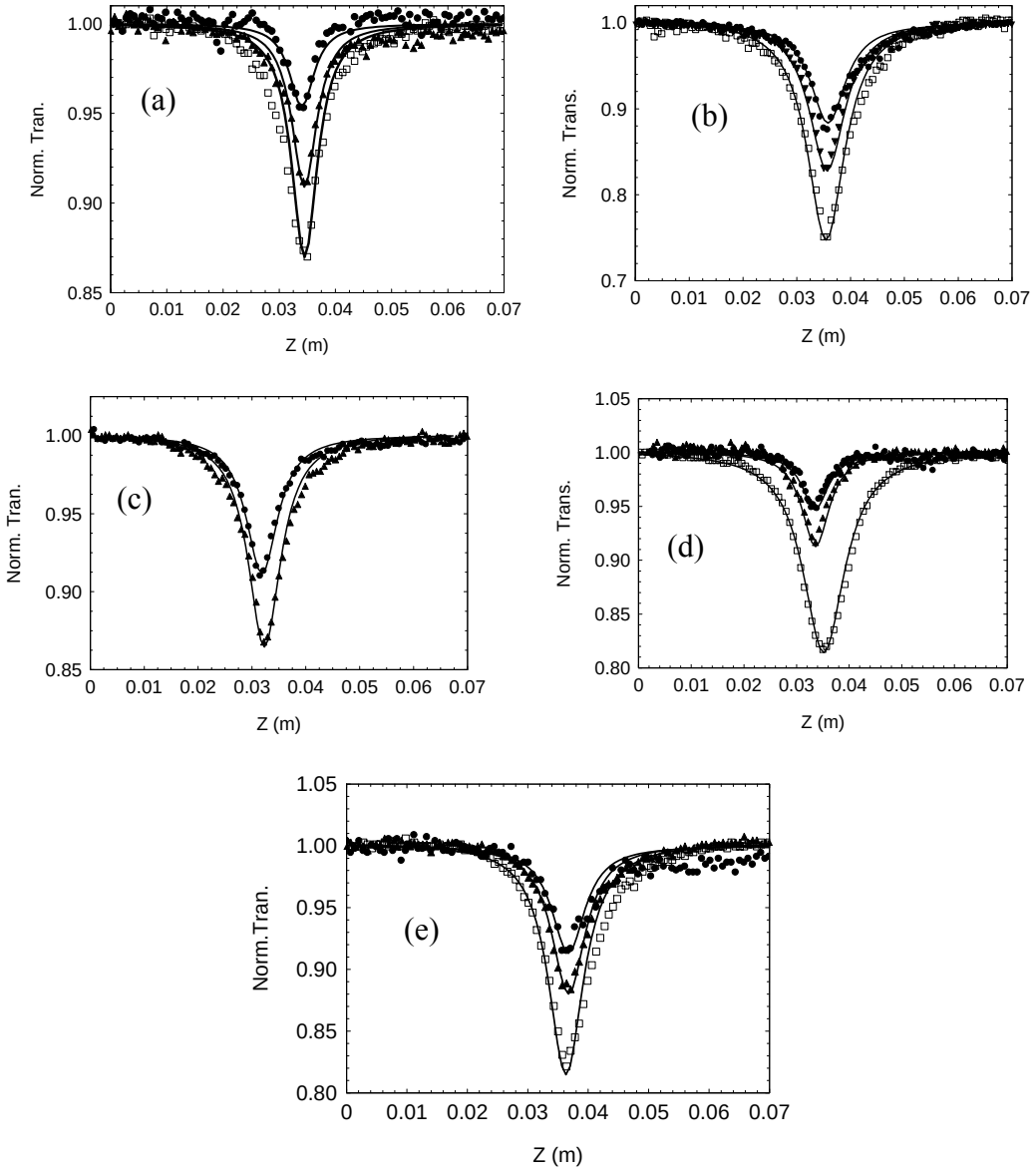

Figure 6.4: Z-scan results for (a) PD2350 in MF at fluences of $1\cdot10^{-3}$ J/cm^2 (circles), $2.2\cdot10^{-3}$ J/cm^2 (triangles), and $4.3\cdot10^{-3}$ J/cm^2 (squares); (b) PD1952 in ethanol at fluences of$2.9\cdot10^{-3}$ J/cm^2, $5.7\cdot10^{-3}$ J/cm^2, $9.8\cdot10^{-3}$ J/cm^2; (c) PD3428 in methanol at fluences of $2.2\cdot10^{-3}$ J/cm^2 (circles), $4.5\cdot10^{-3}$ J/cm^2 (triangles); (d) PD2410 in ethanol at fluences of $3.3\cdot10^{-3}$ J/cm^2, $6.6\cdot10^{-3}$ J/cm^2, $14.7\cdot10^{-3}$ J/cm^2; (e) PD824 in PC at fluences of $1.1\cdot10^{-3}$ J/cm^2, $2.2\cdot10^{-3}$ J/cm^2, $4.4\cdot10^{-3}$ J/cm^2.

The picosecond optical limiting measurements are performed to determine higher excited-state properties as discussed in Chapter 2 using the four-level all-singlet model shown in Figure 2.1. Figure 6.5a demonstrates the necessity of the four-level model by showing a fit of the picosecond optical limiting curve for PD1952 in methanol with both the three- (dashed line) and four-level (solid line) models. Primarily we are concerned with determining the higher excited-state cross-section (σ_{23}, or the ratio β defined in Chapter 2) and lifetime (τ_{21}) from the fitting of this data. All the optical limiting curves were performed at 532 nm (the second harmonic of the EKSLPA ND: YAG laser described in 4.2.1). The primary reason for this is that the limiting curves were taken at the peak of the ESA spectrum for a couple of dyes, but due to the instability of the OPG the data was extremely noisy at the high irradiance levels compared to that of the 532 nm data. When performing the fits on this data compared to the 532 nm data there were only slight differences in σ_{23} and no measurable differences in τ_{21}.

One issue that had to be addressed, which was not accounted for in the work in Chapter 2, is the photostability of the polymethines under high irradiance excitation. Figure 6.5b shows an optical limiting curve for PD1952 in methanol performed at repetition rates of 10 Hz (1), 5 Hz (2), and 1 Hz (3). Furthermore, to reduce degradation during the acquisition of the 1 Hz data the sample is moved between every shot to make sure a fresh part of the sample is irradiated. From Figure 6.5b it can be seen that the measurements at different repetition rates starts to diverge at a fluence of ~0.1 J/cm^2 (4.45 GW/cm^2), which demonstrates for fluences, or more correctly irradiances, lower than this value photodegradation is negligible.

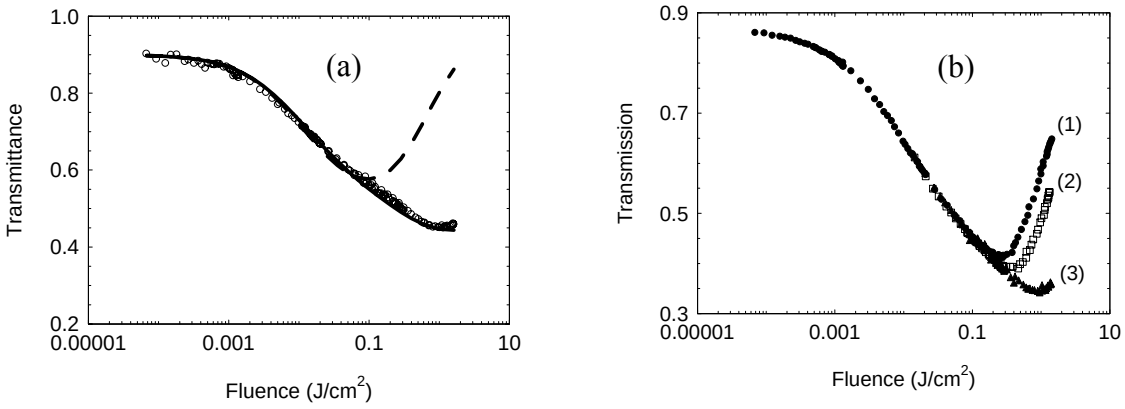

Figure 6.5: (a) Optical limiting curve of PD1952 at 1 Hz in methanol with a three-level model fit (dashed line) and the four-level model fit (solid line); (b) Optical limiting curve of PD1952 in methanol at different repetition rates; (1) 10 Hz, (2) 5 Hz, (3) 1 Hz to demonstrate photodegradation.

Based on the results of Figure 6.5b all limiting curves were taken at 10 Hz up to fluences of ~0.01 J/cm^2 at which point the data was taken at 1 Hz with the sample being moved between each shot. The results for each dye in a different host solvent are shown in Figure 6.6 along with the numerical fits using the four-level model. The quality of the fit shown for each dye is typical for that particular dye in all host solvents. The fits for all dyes do not fit well after the turning point, but it is more pronounced for the di- and tetra-carbocyanines (Figure 6.6a,e) due to the fact that their turnover point is at a much lower fluence. The higher excited-state cross-section along with the first excited-state cross-section determined from the Z-scan experiments for every dye in all solvents are summarized in Table 6.4, which is discussed and shown in Section 6.4.3. The higher excited state lifetimes are summarized in Table 6.2 along with the rest of the excited-state dynamic results, and will be discussed in Section 6.4.2.

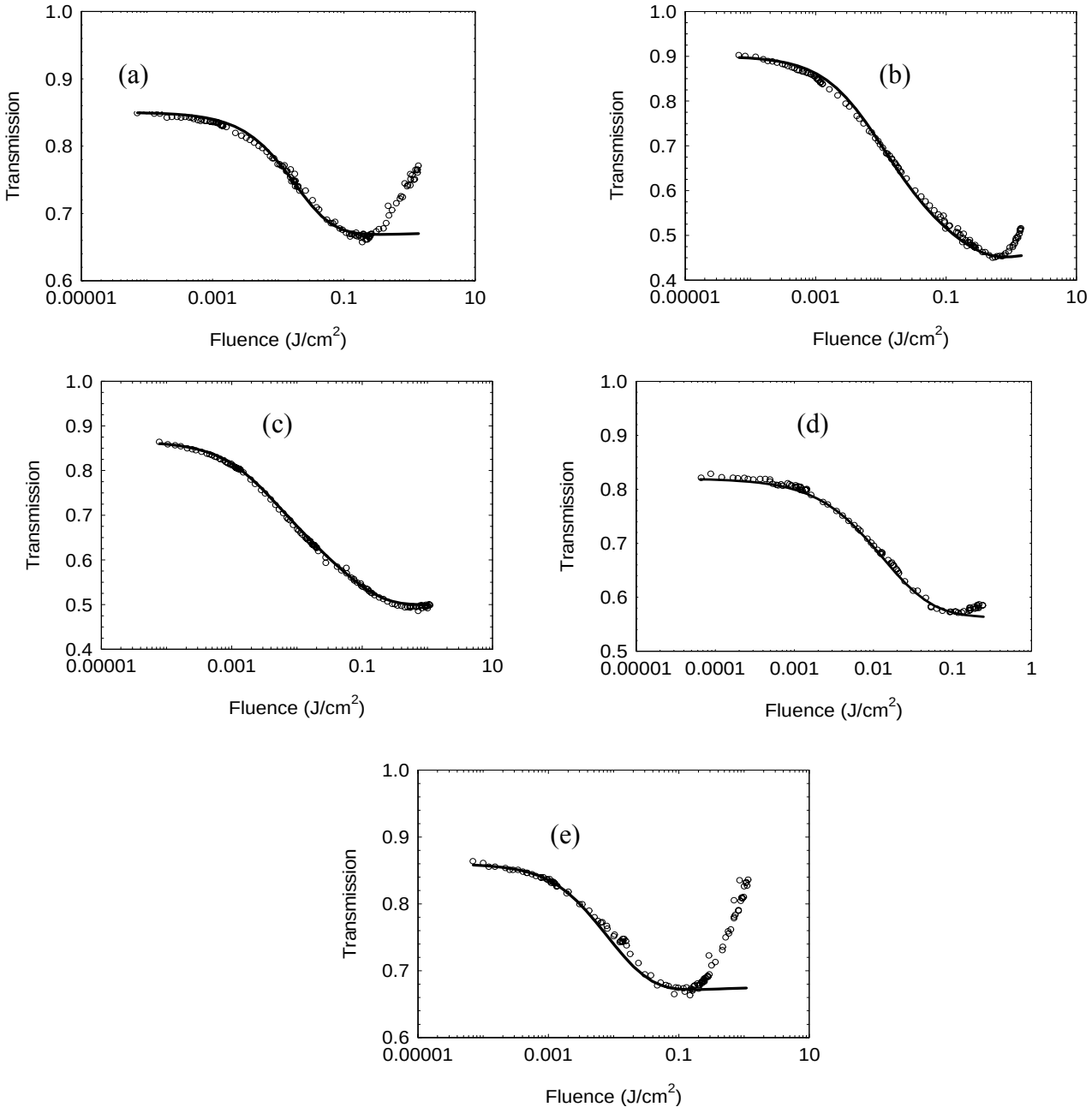

Figure 6.6: Picosecond optical limiting curves with fits using the four-level model shown in Figure 2.1 for (a) PD2350 in pentanol, (b) PD1952 in PC, (c) PD3428 in DMF, (d) PD2410 in ethanol, (e) PD824 in DMSO.

6.3.4. Nanosecond Z-Scans and Optical Limiting Results

Similar to those for the picosecond measurements, the goal of the nanosecond experiments is to determine the molecular parameters which hinder optical limiting in the nanosecond regime and how conjugation length and solvent affect these parameters. The energy level models developed from the picosecond regime are the starting point for developing models for the nanosecond regime that fit both the Z-scan and optical limiting experiments. In this section we will describe the results of the experiments as well as the energy level models.

The first experiments carried out are low energy Z-scans in which the same three level model and molecular parameters are used to fit the results. As with the picosecond Z-scans the nanosecond measurements are performed at the peak of the ESA spectrum for each dye. The linear transmission of all samples is between 80% and 90%. Figure 6.7a shows a typical result for the Z-scan experiment with fitting using the three-level all-singlet model. The measurements spanned an energy range of 26 nJ (Fluence: $3 \cdot 10^{-3}$ J/cm^2, Irradiance: 0.8 MW/cm^2) to 544 nJ (Fluence: $46 \cdot 10^{-3}$ J/cm^2, Irradiance: 7.4 MW/cm^2) and maximum change of transmission of 25%. Figure 6.7b shows the excited-state cross-section for PD1952 in all 8 host solvents determined from the picosecond (circles) and nanosecond (squares) Z-scan measurements. As can be seen by the quality of the fits and the prediction of similar excited-state cross-sections for both the picosecond and nanosecond results the three-level all-singlet model is valid for low energy nanosecond Z-scans. The nanosecond results are summarized with the picosecond results in Table 6.4, which is discussed and shown in Section 6.4.3.

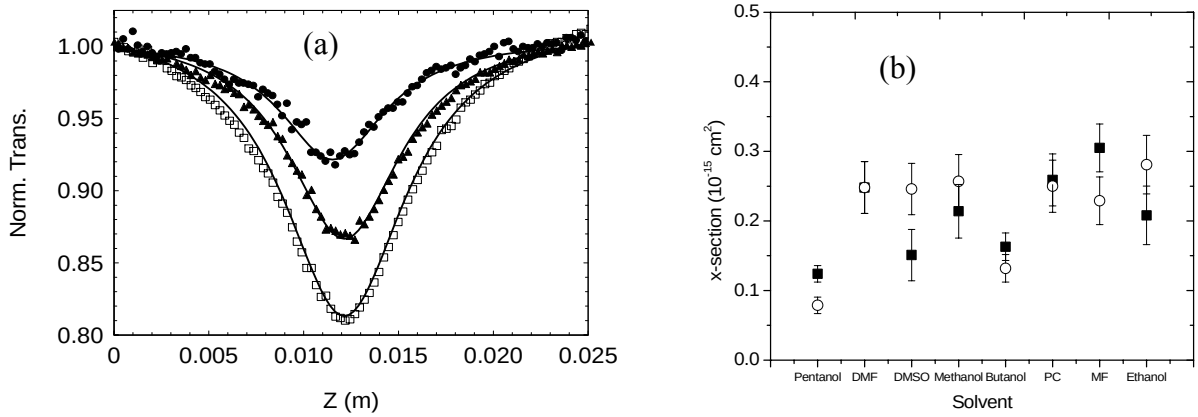

Figure 6.7: (a) Nanosecond Z-scan results for PD2410 in methanol at fluences of $5.8 \cdot 10^{-3}$ J/cm^2 (circles), $11.5 \cdot 10^{-3}$ J/cm^2 (triangles), and $23.1 \cdot 10^{-3}$ J/cm^2 (squares) ,(b) comparison of the excited-state cross-sections determined by the picosecond (open circles) and nanosecond (squares) Z-scans using the three-level all singlet model for pd1952.

The first issue to be addressed concerning the nanosecond optical limiting measurements is whether the four-level all-singlet model used in the picosecond regime is valid in the nanosecond regime. From the results of the nanosecond Z-scans it looked promising that the four-level model would adequately describe the optical limiting results. However, as can be seen in Figure 6.8a the four-level model (dashed line) overestimates the limiting in the nanosecond regime. Four out of the five dyes displayed this same trend, which demonstrates the necessity for a new level structure which must be congruent with the three- and four-level models already in use. The fact that the four-level model overestimates the nanosecond limiting results implies that molecules are decaying to a new state that is not accounted for by the current model. Also, by examining the picosecond limiting results (Figure 6.6) it is obvious that this new process must have a slow formation rate (> hundreds of picoseconds) since it does not affect the picosecond

limiting. These two characteristics lead us to believe that the polymethines undergo a photoisomerization process from the first-excited Trans-state (S_1) to a Cis-state (C_1) as shown in Figure 6.8b. It has been shown by several groups that carbocyanines readily undergo this photoisomerization process [60,102,103]. For the short pulsewidth limiting data we will neglect absorption from state C_1, so the only fitting parameters for this model are the formation (τ_{14}) and decay (τ_{40}) time of this new level. Up to this point we have assumed that the excited-state decay time (measured with the pump-probe experiment) was the only decay pathway, which implies every molecule that decays out of the first excited-state immediately returns to the ground-state. This is no longer the case, and the excited-state decay time (τ_{10}) must be divided between two pathways in the following manner:

$$\frac{1}{\tau_{10}} = \frac{1}{\tau_{14}} + \frac{1}{\tau_{gr}}. \tag{41}$$

Due to this relationship τ_{14} and τ_{gr} are only a single fitting parameter. The nanosecond optical limiting curves were performed at a short (3 ns HW $1/e^2$ M) and long (13 ns HW $1/e^2$ M) pulsewidth to try to access this Cis-State. The results of both experiments are shown below. As with the picosecond measurements all the optical limiting curves were performed at 532 nm, the second harmonic of the Continuum Powerlite 9010.

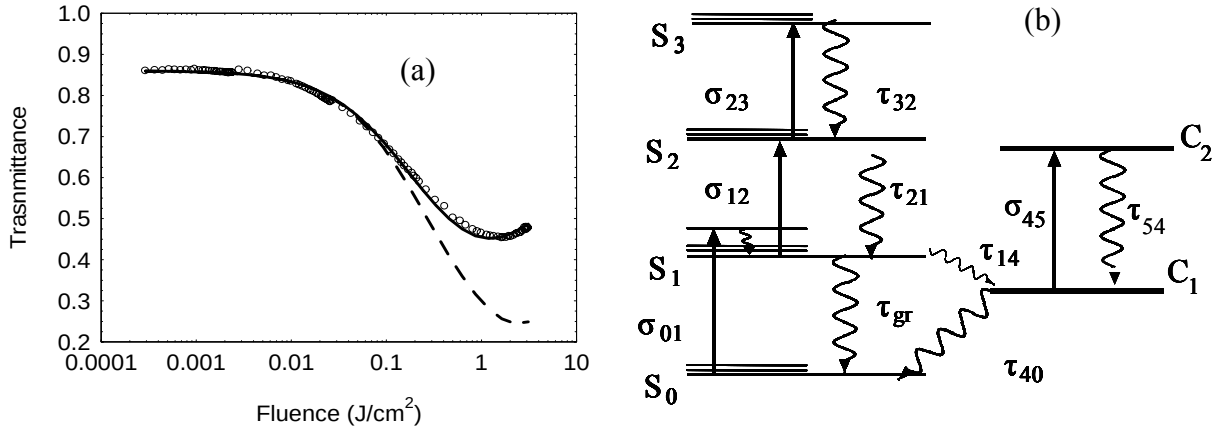

Figure 6.8: (a) Nanosecond optical limiting curves with fits using the four-level model (dashed line) and new five-level model (solid line) shown in Figure 6.8b for PD824 in PC. (b) Six-level model to fit nanosecond optical limiting curves comprised of the four-level model with a new decay pathway from the first excited-state to a Cis-state (C_1).

Photodegradation in the nanosecond regime is not as big of an issue as in the picosecond regime due to the lower irradiance. However, thermal nonlinearities are a concern in the nanosecond regime [104] and care must be taken to avoid thermal defocusing, which can interfere with experimental results in two ways. The most obvious way is that due to thermal lensing the light is defocused so that it is not all collected by the detectors, thus artificially reducing measured transmittance. Even if extra lenses are added to guarantee all light is collected, thermal defocusing can still affect the data analysis. If the thermal nonlinearity is large enough the beam size can change as it passes through the sample so the thin sample approximation is no longer valid [105], which is assumed in all modeling performed in this dissertation. Therefore, closed-aperture Z-scans were performed at low and high energies of the two pulsewidths used for the limiting experiments. From these experiments we found that at the

short pulsewidth the thermal nonlinearity was negligible, but for the long pulsewidth the thermal nonlinearity was substantial. To reduce the effect of the thermal nonlinearity at the long pulsewidth the spot size of the beam was increased to 90 μm from 21 μm. For this spot size the thermal nonlinearity is negligible even for the longer pulsewidth. This is because the response time of the thermal nonlinearity is determined by the ratio of the spot size and the speed of sound in the medium, which for methanol is 1000-1210 meters/second [104]. For the small spot size the response time of the thermal nonlinearity is 16 ns, and for the large spot size it is 75 ns.

The nanosecond limiting results using the short pulsewidth for each dye in a different host solvent are shown in Figure 6.9 along with numerical fits using the four-level model (dashed line) and the five-level model (solid line). Even though photodegradation is not a major issue the sample is still continuously moved, transverse to the beam axis, during the measurement. The fitting procedure for this data is to first determine the best fit parameters using the four-level model and then use these parameters as the starting point for the five-level model. The fits shown in Figure 6.9 are some of the better fits, and in general the data could not be fit as well as the picosecond limiting curves. One possible explanation for this will be given below and discussed in more detail in Section 6.4.3. The lifetimes for the Cis-state formation and decay are summarized in Table 6.2 along with the rest of the excited-state dynamic results, and will be discussed in Section 6.4.2.

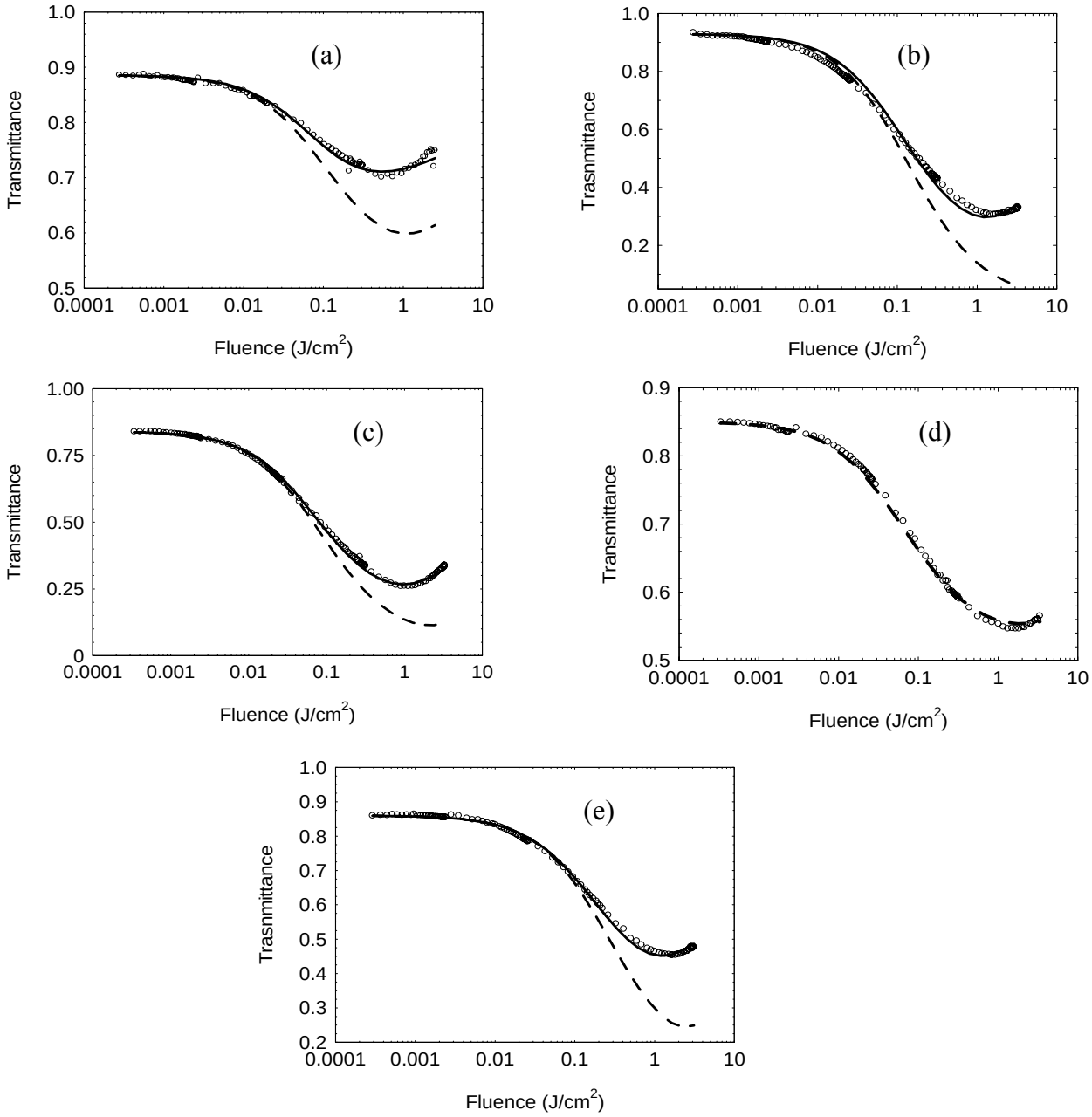

Figure 6.9: Nanosecond optical limiting curves with fits using the four-level model (dashed line) and six-level model (solid line) for (a) PD2350 in DMF, (b) PD1952 in ethanol, (c) PD3428 in butanol, (d) PD2410 in methanol, (e) PD824 in PC.

The long pulsewidth nanosecond limiting was performed for all dyes in methanol only. The six-level model with the Cis-state cross-section (σ_{45}) being zero used for the short pulsewidth data only fits the experimental results for the dicarbocyanine dye (PD2350, Figure 6.10a) and the conjugated bridge tricarbocyanine dye (PD2410, Figure 6.10d). In order to fit the limiting results for the other molecules absorption out of the Cis-state had to be included. The fits using the full six-level model with Cis-state absorption are only approximate, because currently not enough information about the nature of the Cis-state is known. The presence of this Cis-state plays a small roll in the short pulsewidth limiting measurements slightly altering the molecular parameters determined from those fits. With the Cis-State excited-state absorption cross-section and the lifetime of this state unknown the fits can only be approximated. The experimental data with fitting using the six-level model with σ_{45} being zero (solid line) and the six-level model with Cis-state absorption (dashed line) are shown in Figure 6.10. The characteristics of the Cis-state absorption properties are discussed and shown in Section 6.4.3. The data for the decay of the excited-state Cis-state is discussed in Section 6.4.2.

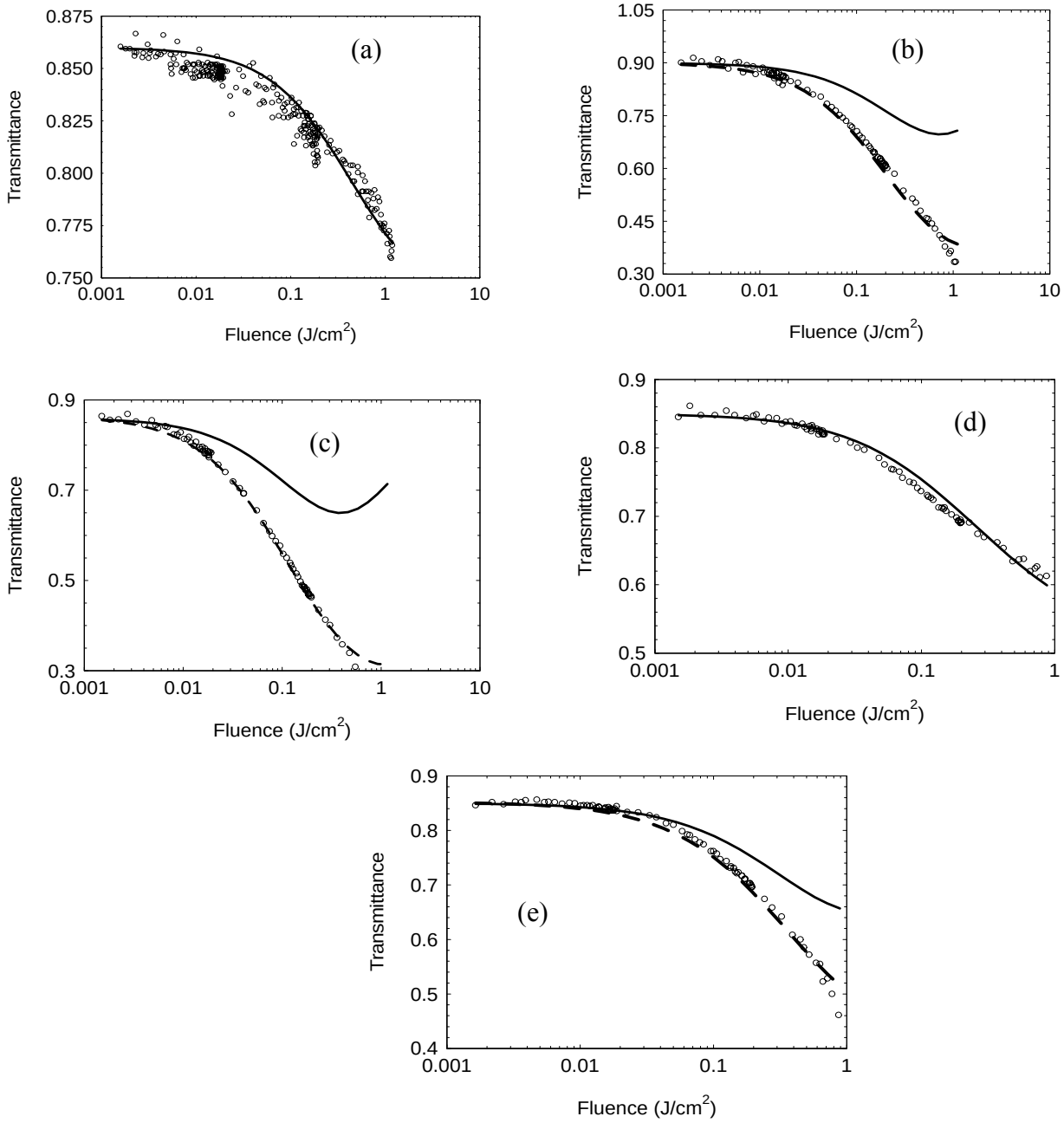

Figure 6.10: Nanosecond optical limiting curves using long pulsewidth with fits using the five-level model (solid line) and the five level-model with absorption out of the Cis state (dashed line) for (a) PD2350, (b) PD1952, (c) PD3428, (d) PD2410, (e) PD824 in methanol.

6.4. Discussion

6.4.1. Excited-State Spectra

The ESA spectra were initially performed only to determine the peak of the spectrum for the nonlinear optical characterization measurements. However, by examining these spectra key insights into the nature of ESA as a function of conjugation length and bridge structure are uncovered. The ESA spectrum along with the linear absorption spectrum for each of the five dyes, along with PD1659, in methanol is shown in Figure 6.11.

First we will examine how the bridge structure effects the ESA spectrum by comparing the spectra of PD3428 (unbridged, Figure 6.11c), PD1952 (dimethylene bridge, Figure 6.11b), and PD2410 (vinylene bridge, Figure 6.11d). The most obvious feature is that the bridged structures only have a single peak in the ESA spectrum, whereas the unbridged structure possess a double peak. Another important feature is the large red shift in the peak of the ESA spectrum (to ~590 nm) of the conjugated bridge (PD2410) whereas the unconjugated bridge (PD1952) peak remains at the same wavelength (~532 nm) as the unsubstituted chromophore (PD3428). It is interesting to note that while the shape of the ESA spectra has been altered due to the bridge structure the peak ESA cross-section of all three dyes are within 20 %.

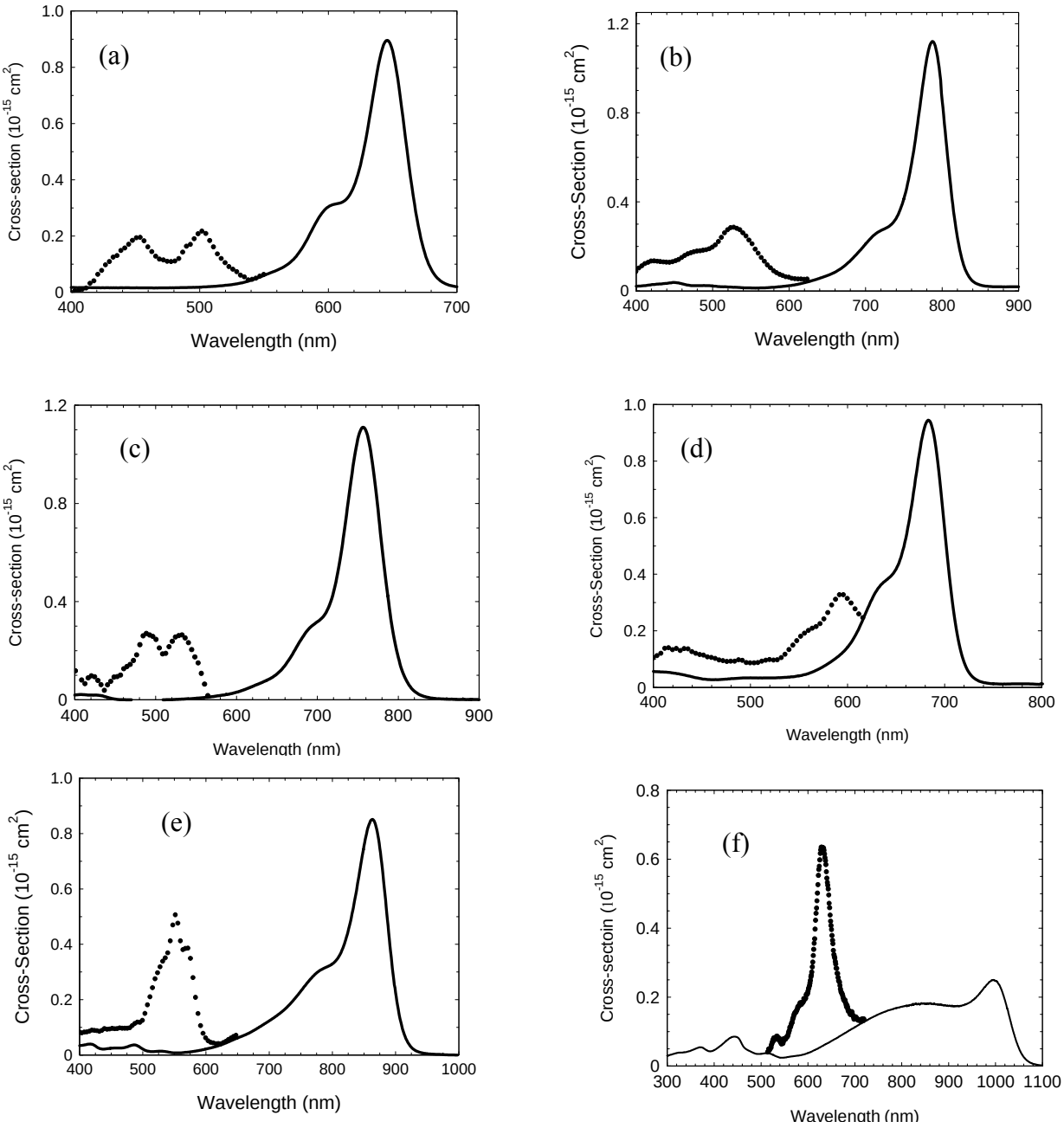

Figure 6.11: ESA Spectra for (a) PD2350, (b) PD1952, (c) PD3428, (d) PD2410, (e) PD824 in methanol, (f) PD1659 in methanol. Solid line is the linear absorption spectrum; dotted line is the ESA spectrum.

Next we will examine the ESA spectra of the unsubstituted di- and tricarbocyanine dyes (PD2350 and PD3428) along with the substituted tetra- and pentacarbocyanine dyes (PD824 and PD1659). The ideal case would be to examine an entire series of unsubstituted dyes from di- to pentacarbocyanine, but the tetra and penta forms are too unstable to exist in an unsubstituted form. The general characteristics of the linear absorption spectrum of polymethine molecules as the conjugation length is increased were discussed in the introduction. The main properties are a red shift and broadening of the linear absorption band as the conjugation length is increased. We are now in position to make a comparison between these linear absorption band properties and the ESA band properties.

First we will examine the red shift of the ESA spectrum as a function of conjugation length compared to that of the linear absorption spectrum. Figure 6.12a shows the absorption maximum for the linear (squares) as well as the ESA (circles) absorption profiles for di- to pentacarbocyanine. As can be seen the linear absorption peak shifts by over 350 nm while the ESA peak shifts by only 120 nm. This small shift in the ESA spectrum as a function of conjugation length could have important consequences for the design of broadband optical limiters using polymethines. In certain cases this small shift could be an advantage because it allows for the possibility to combine several dyes of different conjugation length, which have their linear absorption peaks outside of the visible, but have partially overlapping ESA spectra to adequately cover a large range of the visible spectrum. The major problem; however is that the visible spectrum covers the spectral range of approximately 400 -700 nm, and from Figure 6.12a it can be seen that it would be difficult to get polymethines with ESA spectrums to cover the range of 600 – 700 nm.

The second interesting characteristic to compare is the spectral width of the ESA band compared to that of the linear absorption band. It is more meaningful to look at frequency when comparing widths of spectra since it is directly proportional to the energy. Figure 6.12b shows the FWHM in wavenumbers (cm^{-1}) of the linear (squares) and ESA (circles) absorption bands. From this figure it is clearly seen that while the linear absorption width stays nearly constant up to the tetracarbocyanine the ESA spectrum width continuously decreases. It is probably more instructive to compare the integrated area ($\int \alpha(\nu) d\nu$) of the absorption bands since it is directly related to the oscillator strength of the transition [106]. The integrated areas of the linear and ESA absorption bands are shown in Figure 6.12c. The main characteristic to note from this figure is that as the conjugation length is increased, the areas of the linear and ESA absorption bands become similar. The ratio of the two areas is shown in Figure 6.12d. This is a very important result because this shows that as the conjugation length is increased the oscillator strength of the excited-state is a larger proportion of the ground state oscillator strength. For example, the pentacarbocyanine dye, PD1659, excited-state oscillator strength is nearly 90% of the ground state oscillator strength. This large oscillator strength means that the excited-state cross-section can be as large or even larger then the maximum ground state cross-section as can be seen in Figure 6.11f.

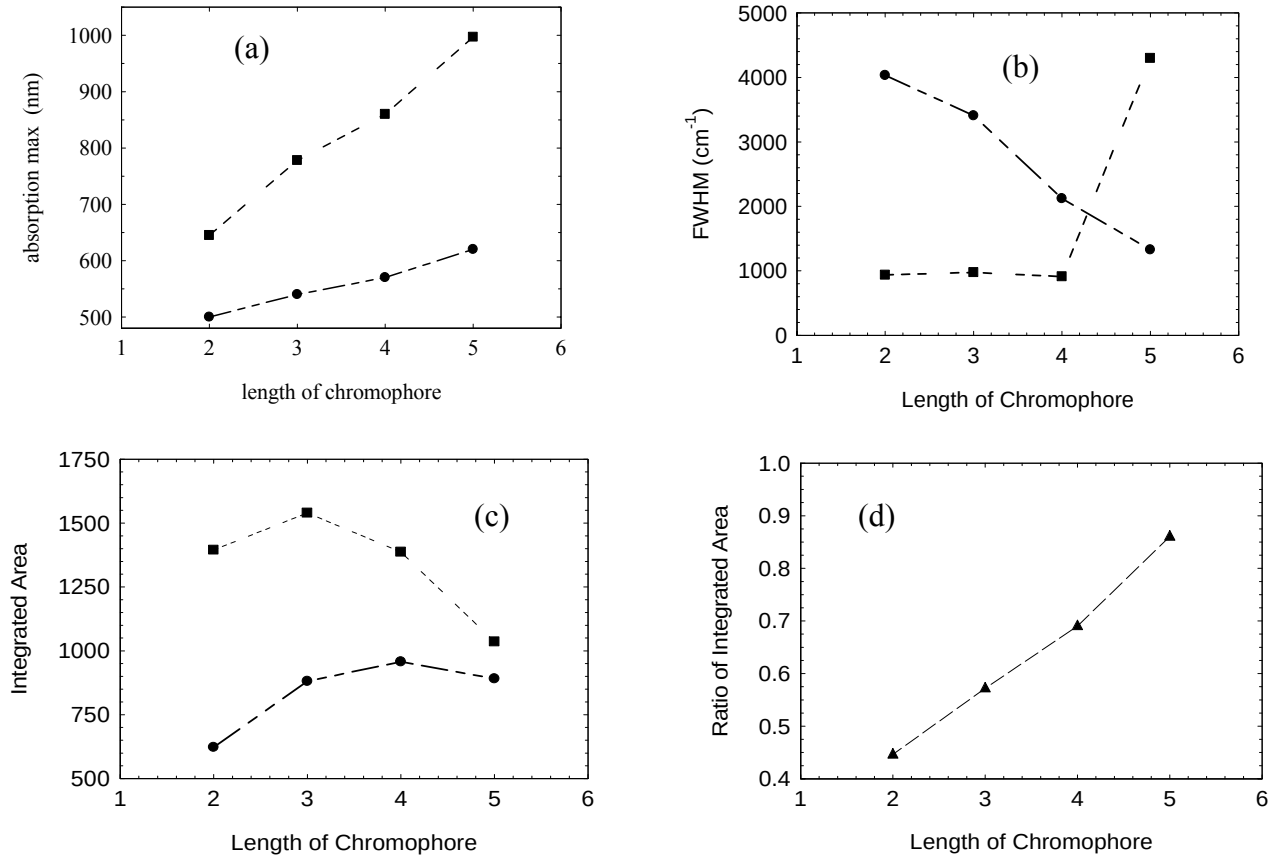

Figure 6.12: Analysis of ESA spectrums for di- to pentacarbcyanine dyes. (a) Peak of linear (squares) and ESA (circles) spectrums. (b) FWHM (cm^{-1}) of linear (squares) and ESA (circles) absorption bands. (c) Integrated area of linear (squares) and ESA (circles) absorption band. (d) Ratio of integrate areas of ESA and linear absorption bands

The final characteristic we would like to examine is the shape of the ESA spectrum from the di- to pentacarbocyanine molecule. It is seen in Figure 6.11a that for the dicarbocyanine molecule there are two clearly resolvable peaks in the ESA spectrum separated by 50 nm. As the conjugation length is increased to tri- and tetracarbocyanine the separation between these two peaks decreases to 41 nm and 20 nm, respectively. For the pentacarbocyanine shown in Figure

6.11f, the ESA spectrum has only a single peak. The reason for this is still being investigated, but is probably connected with the symmetric and asymmetric charge distribution of polymethine molecules discussed in Chapter 5. In Figure 5.5a the symmetric forms of the Δq-functions for the excited-state of thiacarbocyanines of chain lengths of 1 - 6 are shown, and this clearly shows two minima in the excited-state Δq-functions for chain lengths as short as dicarbocyanine. The barrier between these two minima in the Δq function decreases as the chain length is increased. The quantum chemical analysis of this is still in the initial stages, but this could have important consequences for maximum excited-state cross-sections possible for polymethines of a given chain length. For example, the two forms of the excited-state of the dicarbocyanine dye (Figure 6.11a) divide the possible oscillator strength for that transition thus reducing the maximum cross-section for this transition.

6.4.2. Excited-State Dynamics

In this section the ESA dynamics of the polymethine molecules will be discussed. This includes the dynamics directly measured by the pump-probe experiments (i.e. excited-state decay, orientational diffusion, and ground-state recovery times) and those determined indirectly from the fitting of picosecond and nanosecond data (i.e. higher excited-state decay, Cis-state formation and decay). The decay of the Cis excited-state (τ_{54}) determined from the fitting of the six-level model was found to be on the order of 20 – 100 picoseconds. All other excited-state dynamic results are displayed in Table 6.2.

Table 6.2: Excited-State Dynamics

Dye	τ_{10} (ns)	τ_{OR} (ps)	τ_{21} (ps)	τ_{14} (ns)	τ_{gr} (ns)	τ_{40}
PD2350						
Methanol	0.8	110	2	30	0.8	> 100 ns
Ethanol	1.0	230	1	30	1.1	> 100 ns
Butanol	1.4	440	4	11	1.7	> 100 ns
Pentanol	1.3	620	3	30	1.4	> 100 ns
DMF	1.5	310	11	7	1.9	> 100 ns
DMSO	1.6	310	11	9	1.9	> 100 ns
MF	1.1	400	9	7	1.3	> 100 ns
PC	1.3	480	2	25	1.3	> 100 ns
PD1952						
Methanol	1.0	140	3	2.0	2.1	> 100 ns
Ethanol	1.3	310	3	1.2	10	> 100 ns
Butanol	1.2	590	4	DNF	DNF	DNF
Pentanol	0.9	790	4	DNF	DNF	DNF
DMF	1.3	270	8	3.0	2.3	> 100 ns
DMSO	1.5	430	4	1.9	7.0	> 100 ns
MF	1.2	460	4	1.4	9.0	> 100 ns
PC	1.3	580	3	1.5	11.0	> 100 ns
PD2410						
Methanol	1.2	160	3	NA	NA	NA
Ethanol	1.4	370	7	NA	NA	NA
DMSO	1.3	360	7	61	1.4	> 100 ns
PC	0.7	620	3	13	0.8	> 100 ns
PD3428						
Methanol	1.0	220	9	2	1.9	> 100 ns
Ethanol	1.3	350	17	1.9	4.0	> 100 ns
Butanol	1.3	610	17	2.8	2.5	> 100 ns
DMF	1.3	350	12	1.9	3.7	> 100 ns
DMSO	1.6	780	16	DNF	DNF	DNF
MF	1.2	500	15	1.8	3.9	> 100 ns
PC	1.60	630	15	2.6	4.0	> 100 ns
PD824						
Methanol	0.2	190	10	3.5	0.2	> 100 ns
Ethanol	0.3	260	11	2.8	0.3	> 100 ns
Butanol	0.3	620	15	6	0.3	> 100 ns
Pentanol	0.3	860	8	1.8	0.4	> 100 ns
DMSO	0.4	890	16	35	0.4	> 100 ns
PC	0.4	990	16	1.5	0.5	> 100 ns

DNF: Did not fit, NA: Not applicable, because parameters were not required.

First we will examine the energy level kinetics, which encompasses all the lifetimes of the various models. In this analysis we are trying to identify the kinetics which are beneficial for picosecond and nanosecond optical limiting and the connection between these model parameters to the molecular and solvent parameters. A long excited-state lifetime (τ_{10} > pulsewidth, in this case nanoseconds) has often been regarded as a key molecular parameter for efficient optical limiting [20]. Therefore, understanding the connection between conjugation length and solvent properties on excited-state lifetime is important. Figure 6.13 shows the dependence of excited-state lifetime on conjugation length and demonstrates that for polymethines with chain lengths longer than tricarbocyanine the excited-state lifetime drops off dramatically. This doesn't mean that all polymethines with chain lengths longer than tricarbocyanine will be poor optical limiters; however, it does mean that the other molecular parameters will need to be able to compensate for this deficiency (i.e. large cross-sections).

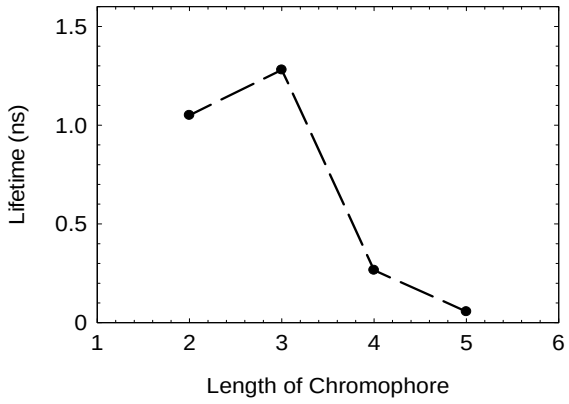

Figure 6.13: Excited-state lifetime as a function of conjugation length for di- to pentacarbocyanine in methanol

The excited-state decay pathway also plays a crucial role in the overall optical limiting performance. At high fluence levels in the nanosecond regime in which the Cis-state can be populated, it is shown by Eq. 41 that the excited-state decay has two pathways. In cases where the excited-state decay time (τ_{10}) is close to or equal to the ground-state recovery time (τ_{gr}) the four-level model applies, and as can be seen in Figure 6.9 (dashed lines), better limiting performance is observed. In contrast, where there is a large difference between τ_{10} and $\tau_{gr,}$ means a large population is building up in the weakly absorbing Cis-State (short τ_{14}), thus hindering the optical limiting performance. The dicarbocyanine (PD2350) and conjugated bridge tricarbocyanine (PD2410) dyes appear to be the most rigid molecules out of the five studied, having the longest formation time for the Cis-state. Surprisingly, the dye with the longest chain length, the tetracarbocyanine (PD824), possesses a Cis-formation rate an order of magnitude larger than its excited-state lifetime. While the other two tricarbocyanines (PD1952, PD3428) have Cis formation rates on the same order as their excited-state lifetime.

If there was a way to externally increase the excited-state lifetime of a molecule that already possesses a large cross-section, it would be ideal. The large class of host solvents allowed us to look for connections between excited-state lifetime and solvent. Figure 6.13b shows the excited-state lifetime of PD1952 in all 8 host solvents as a function of refractive index. From the graph and Table 6.2 there appears to be a slight dependence of excited-state lifetime on index of refraction. From the solvent with the smallest index (methanol) to the solvent with the largest index (DMSO) the excited-state lifetimes become on average 60% larger.

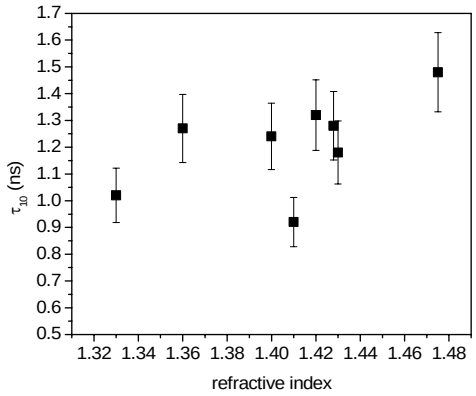

Figure 6.14: Excited-state lifetime as a function of solvent for PD1952 in all solvents as a function of refractive index.

The effect of the higher excited-state lifetime has on picosecond optical limiting was demonstrated in Chapter 2. The fact that the higher excited-state has a finite lifetime is the cause of the saturation effect in the picosecond regime. Molecules with shorter higher excited-state lifetimes will be better picosecond optical limiters. This is due to the fact that the shorter the lifetime the faster the molecules return to the first excited state and can be reabsorbed by the same pulse. This lifetime however has no observable effect on the nanosecond limiting. Also the recover time from the Cis-state back to the Trans-state (τ_{40}) appears to be much longer than the pulsewidth, independent of the solvent. From the fitting, we can only put a lower limit on this time of ~100 nanoseconds.

The final dynamic property we want to cover in this section is a thorough analysis of the orientational diffusion times of the molecules. In chapter 3 it was demonstrated that the SED model underestimates the orientational diffusion times and the error was attributed to a solvent shell surrounding the solute molecule. But as noted in the introduction several key features were

neglected and will be examined at this time. In this section we are going to use the modified SED model including dielectric friction given as:

$$\tau_r = \frac{\eta V}{kT} f C_{bnd} + \tau_{DF} \tag{42}$$

where C_{bnd} is a constant that describes the boundary condition and $C_{bnd} = 1$ for stick condition and $0 \le C_{bnd} < 1$ for the slip boundary condition. The simplest method for determining the slip condition was proposed by Hu and Zwanzig [99] and only takes into account the size and shape of the solute molecule were as more recent theories have considered both the solute and solvent size and shapes and the interaction between them [97]. In this work we will only consider the Hu and Zwanzig slip condition. The Perrin shape factor (*f*) corrects for the nonspherical shape of the polymethines and for a prolate ellipsoid of revolution is given as:

$$f = \frac{2}{3} \frac{1-\rho^4}{(2-\rho^2)\frac{\rho^2}{\sqrt{1-\rho^2}} \ln\left[\frac{1+\sqrt{1-\rho^2}}{\rho}\right] - \rho^2} \qquad \rho < 1 \tag{43}$$

where ρ is the ratio of the average of the two short axes by the long axis. The SED model itself describes hydrodynamic friction arising out of the viscosity itself. When dealing with dipolar solute molecules in polar solvents, dielectric friction needs to be taken into consideration. The dielectric friction term [98] is given as:

$$\tau_{DF} = \frac{\mu^2}{9a^3 kT} \frac{(n^2+2)^2(\varepsilon_0 - n^2)}{(2\varepsilon_0 + n^2)^2} \tau_D \tag{44}$$

where μ is the excited-state dipole moment, a is the cavity radius the solute molecule rotates within, and τ_D is the dielectric relaxation time of the solvent given in Table 6.2. The cavity radius (*a*) is calculated two different ways in the literature [98] to give a maximum and minimum

value. The method to determine the minimum value of the cavity radius is to treat the Van der Waals volume of the solute molecule as a sphere and calculate the radius. The second method, which gives the maximum value, is to take half the length of the long axis of the molecule. The value of all molecular parameters including molecular volumes, dimensions, ground and excited-state dipole moments, shape factor (f), and maximum and minimum cavity radius for each molecule is given in Table 6.3.

Table 6.3: Molecular Parameters for Orientational Diffusion Analysis

Dye	Volume ($Å^3$)	Dx,Dy,Dz (Å)	S_0 Dipole Moment (Debye)	S_1 Dipole Moment (Debye)	f	a (Å) min, max
PD2350	470	18.6,6,4.5	0.3	1.9[b]	2.89	4.8, 9.3
PD1952	420	23,11,6	1.5	4.2[a]	2.08	4.6, 11.5
PD3428	380	21,6,4.5	1.2	3.2[a]	3.40	4.5, 10.5
PD2410	415	23,12,6	1.5	4.0[a]	1.94	4.6, 11.5
PD824	490	23.5,6.7,7.5	0.8	NA	2.65	4.9, 11.75

a: determined from quantum chemical calculations, b: determined from fit of Lippert-Mataga equation,
NA: unable to take fluorescence data to fit

To calculate the dielectric friction contribution, to the reorientationl diffusion time the excited-state dipole moment and correct cavity radius (between maximum and minimum values) of the molecules must be determined. For the tricarbocyanines the excited-state dipole moments are determined from quantum chemical calculations. To determine the correct cavity radius we turn to the Lippert -Mataga equation, given by Eq. 38, and fit the difference between the absorption and fluorescence peaks ($\Delta\nu$) as a function of polarity. The results for PD3428 (squares) and PD1952 (triangles) are shown in Figure 6.15 and from the fits it is determined that the minimum cavity radius should be used. So to determine the excited-state dipole moment of

PD2350 we use the minimum cavity radius and the fitting parameter is $\Delta\mu_{ge}$ in the Lippert-Mataga equation. The result for PD2350 (circles) is shown in Figure 6.15 and $\Delta\mu_{ge}$ is found to be 1.6 Debye, so using the ground-state dipole moment from Table 6.3 results in an excited-state dipole moment of 1.9 Debye. For PD824 the fluorescence measurement can not be performed due to the limitation of the spectrofluorimeter.

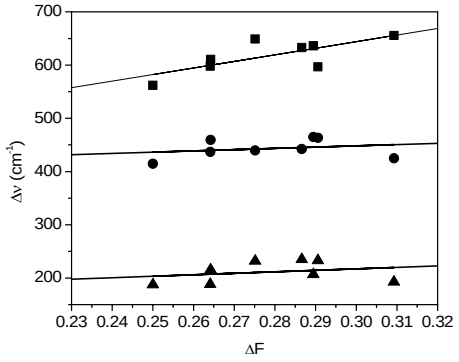

Figure 6.15: Δν versus polarity for PD3428 (squares), PD2350 (circles), and PD1952 (triangles) with fits using the Lippert-Mataga equation. Fit parameter for PD3428 a: 6.4 Å, PD1952 a: 4.5 Å, PD2350: $\Delta\mu_{ge}$= 1.6 Debye, μ_e=1.9 Debye.

To analyze the orientation diffusion time including the dielectric friction contribution, relationships between viscosity and dielectric constant, index of refraction, and dielectric relaxation times must be developed. In order to do this we fit these solvent parameters as a function of viscosity with fifth order polynomials for the alcohols only. The fact that the solvatochromatic shifts follow the same trend for both the protic (alcohols) and aprotic solvents shows that this is a good approximation. The experimental data for PD1952 and PD2350 along with the model given by Eq. 42 and a stick boundary condition ($C_{bnd} = 1$) is shown (solid line) in

Figure 6.16. The model using the slip boundary condition predicted by the Hu and Zwanzig model for PD1952 ($C_{bnd} = 0.41$) and PD2350 ($C_{bnd} = 0.53$) are also shown (dotted line) in Figure 6.16. The main characteristic to note is that PD1952 follows the stick boundary condition where as PD2350 follows the slip boundary condition. In fact PD2350 is the only dye that follows a slip boundary condition. The reason for this is not readily obvious, but could be connected with PD2350 is the shortest molecule studied and its optimized geometry is planer (small values of dy and dz). However, this is not a complete explanation because PD3428, which is a tricarbocyanine and also has a planer geometry, but more closely follows the stick boundary condition than the slip.

Overall the modified SED model accurately predicts orientational diffusion times without invoking a solvent shell. This modified SED model is advantageous over the inclusion of a solvent shell because the size of this shell is arbitrary and any other solvent effect would be neglected, such as the identification of the slip boundary condition for PD2350. The Perrin shape factor correction plays the biggest role in this modified equation, where as the dielectric friction term only alters the orientational diffusion time on the order of 5 – 15 picoseconds and could be neglected in future orientational diffusion analysis.

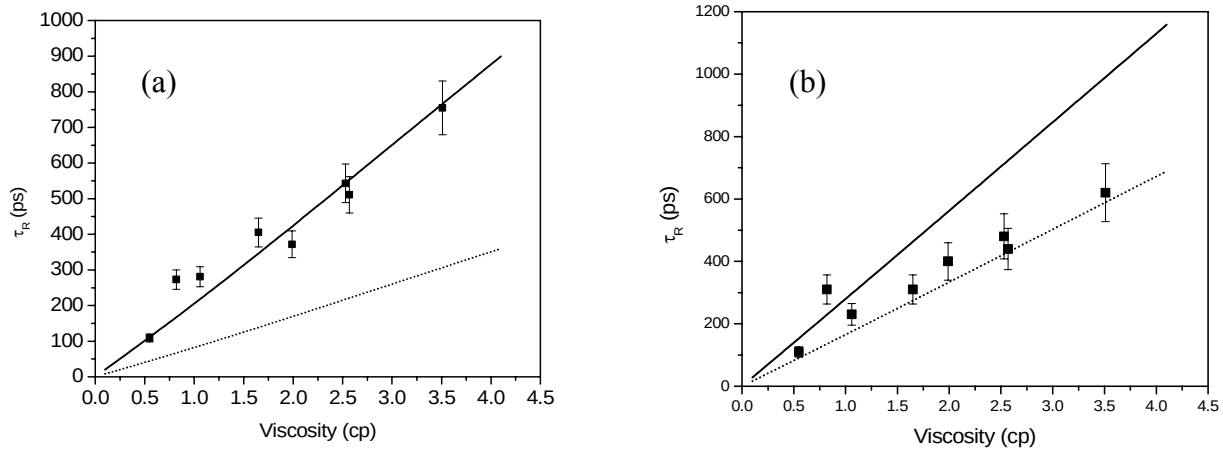

Figure 6.16: Orientational diffusion times and fits with a stick boundary condition (solid line) and slip boundary condition (dotted line) for (a) PD1952 and (b) PD2350.

6.4.3. Nonlinear Optical Characterization

In this section we will be concerned with identifying the affects of conjugation length, bridge structure, and host solvent on the overall ESA properties of the five polymethines, and how these parameters apply to optical limiting. This will include an analysis of how the molecular and solvent parameters affects the cross-sections (ground, 1st and higher excited-states, and Cis-State). Given this analysis, we will be in a good position to examine the optical limiting curves spanning the picosecond to nanosecond time regime. The absorption from the Cis-state can only be approximated due to the fact that with the inclusion of absorption from this state too many free parameters exist in the model to make an accurate determination. With that said, the fits of the Cis-state cross-section were measured to be $2.44 - 7.92 \cdot 10^{-17}$ cm^2 for the three molecules (PD3428, PD1952, PD824) requiring absorption out of the Cis-state. The data for all other cross-sections are displayed in Table 6.4. The results of the picosecond and nanosecond Z-

scans are displayed as “α pico” and “α nano”, respectively, and are the ratio of the ESA cross-section to the ground-state cross-section at the peak of the ESA. The column “α 532” is the ratio used in the limiting experiments and was determined from using the ESA spectra to extrapolate from the peak to 532 nm. The higher-excited-state is given as β, and is also in reference to 532 nm. As seen in Table 6.4 the discrepancy between the results of the picosecond (α pico) and nanosecond (α nano) Z-scans is larger than the experimental error for PD3428 and PD824. This could be due to absorption of the Cis-state which seems to have the largest contribution for the unbridged tricarbocyanine (PD3428) and the tetracarbocyanine (PD824).

Table 6.4: Nonlinear Absorption Properties

Dye (ESA Peak λ)	Peak GS x-section ($\cdot 10^{-15}$ cm^2)	GS @ ESA peak x-section ($\cdot 10^{-18}$ cm^2)	α peak pico	α peak nano	GS @ 532 nm x-section ($\cdot 10^{-18}$ cm^2)	α 532 nm	β
PD2350 (500 nm)							
Methanol	0.88	5.4	46	46	24.5	2.8	2
Ethanol	0.90	4.7	45	55	29.0	2.5	2.2
Butanol	0.89	4.1	62	60	15.0	3.8	2.3
Pentanol	0.83	7.3	40	42	29.0	3.0	2.5
DMF	0.83	6.6	45	38	21.0	5.0	2.4
DMSO	0.91	4.2	66	58	18.2	5.0	2.6
MF	0.66	4.3	54	66	16.9	5.3	2.4
PC	0.84	6.7	43	50	25.3	3.5	2.3
PD1952 (532 nm)							
Methanol	1.02	3.1	84	70	Peak @ 532		7
Ethanol	1.12	2.2	128	95			6.8
DMF	0.90	4.5	55	55			4.5
DMSO	0.82	3.1	78	48			5.2
MF	0.70	1.9	122	162			5.2
PC	0.85	2.6	95	98			6.3
PD2410 (594 nm)							
Methanol	0.92	119	3.2	4.2	36.1	4.3	2.9
Ethanol	0.94	115	2.9	4.5	34.7	4	2.9
DMSO	0.72	94	2.4	3.9	28.4	4	2.4
PC	0.76	99	3.0	6.5	30	4.8	2.8
PD3428 (532 nm)							
Methanol	1.10	6.3	50	87	Peak @ 532		6
Ethanol	1.11	6.4	44	73			5.3
Butanol	1.02	6.0	30	57			4.8
DMF	0.77	7.7	34	36			4.8
DMSO	0.89	5.1	63	NM			5.5
MF	0.74	4.3	65	90			4.3
PC	0.91	5.2	58	85			3.6
PD824 (570 nm)							
Methanol	0.88	16.4	23	39	15.8	17	3.5
Ethanol	0.85	10.2	38	63	13.7	20	4.3
Butanol	0.90	7.5	52	80	16.2	12	2.8
Pentanol	0.29	7.9	41	49	10.7	25	3.8
DMSO	0.49	22.9	16	26	28.0	7	2.6
PC	0.32	7.8	39	60	7.8	24	2.6

NM: not measured, Error in α: ± 10%, β: ± 20%

First we will examine the results of the linear absorption measurements and the Z-scans, which provide information about the ground and 1st excited-state cross-sections, respectively. Figure 6.17a shows the ground (squares) and excited-state (circles) cross-section for PD1952 in all host solvents. As can be seen in the figure and Table 6.4 there is no strong connection between solvent and peak ground-state cross-section, which has values on the order of 10^{-15} cm^2. The only noticeable trend is that the ground-state cross-sections are on average 5-15% smaller in the aprotic solvents. But, as can be seen from the excited-state cross-sections (circles in Figure 6.17a) this small variation in the peak ground-state cross-section has no noticeable connection to the ESA cross-sections. It is also interesting to compare the peak ground-state cross-section to the cross-sections at the wavelengths the nonlinear optical measurements are performed. For PD2350, PD1952, and PD3428 the values of the ground state cross-sections at the wavelength of the peak ESA spectra are 2 - 3 orders of magnitude smaller. For these values of the ground state cross-sections the concentrations of these three dyes for all the nonlinear optical measurements is $\sim 10^{-4}$ mol $liters^{-1}$ ($T_L \approx 0.80$). For PD2410 and PD824 the difference in cross-sections is only 1 order of magnitude due to the redshift of the ESA peak for PD2410 and the broadening of the linear absorption spectrum for PD824. This small difference (larger ground-state cross-section for the nonlinear measurements) means the concentration is on the order of 10^{-5} mol $liters^{-1}$, which could pose a problem from the stand point of optical limiting because it is easier to saturate these materials either by population saturation or photobleaching. As can be seen in Figure 6.6 the picosecond limiting results show PD2350 and PD824 saturate more quickly than is predicted by the four-level model, but not PD2410. This could be explained by the fact that PD2410 has the smallest ratio of ground- to excited-state cross-section ($\alpha \approx 4$) so it is not easily

saturated, while PD824 and PD2350 have large ESA and ground-state cross-sections at 532 nm resulting in rapid saturation.

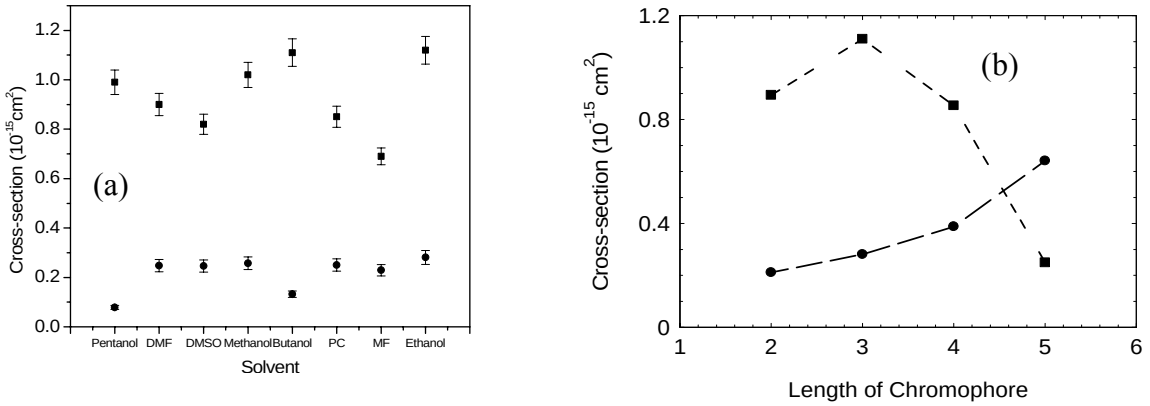

Figure 6.17: Analysis of ground and ESA cross-sections. (a) Ground (squares) and excited-state (circles) cross-section for PD1952 in all host solvents. (b) Peak ground-state cross-section (squares) and excited-state cross-section (circles) as a function of conjugation length (di: DP2350, tri: PD3428, tetra: PD824, penta: PD1659), all dyes in methanol.

The peak ground (squares) and ESA (circles) cross-sections as a function of conjugation length are shown in Figure 6.17b, and show that while the peak ground-state cross-section decreases as the conjugation length increases to tetra- and pentacarbocyanine the ESA cross-section continuously increases until it is larger than the ground-state cross-section. This result was alluded to in the discussion of the ESA spectra when the ratio of integrated areas of the ground- and excite-state spectra was shown in Figure 6.12d. As stated in Chapter 5 this is the first time an ESA cross-section has been found to be larger than the peak ground-state cross-section. The usefulness of this molecule for nanosecond optical limiting is in doubt though due to its poor photochemical stability and short excited-state lifetime ($\tau_{10} \approx 50$ picoseconds).

The picosecond optical limiting results not only provide information about the higher-excited-state cross-section (β) of the polymethines, but more importantly we can determine characteristics of the polymethines that are ideal for picosecond optical limiting. The experimental data of all five dyes is shown for two solvents in Figure 6.18a,b. The results of the picosecond optical limiting experiments for all dyes, including the linear transmittance (T_L), minimum transmittance, percent change in transmittance, and turnover fluence are summarized in Appendix C in Table C.1. In Figure 6.18 the best limiter in the picosecond regime is clearly the tricarbocyanine dye PD1952 and the worst is the dicarbocyanine dye, PD2350. But performing an analysis in this way is rather misleading since we are not at the peak ESA spectral position for each dye.

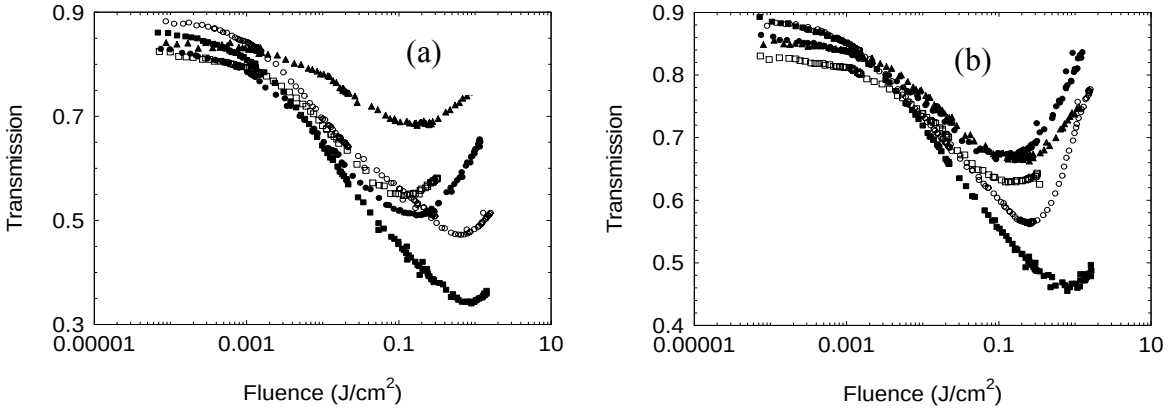

Figure 6.18: Experimental picosecond limiting results for PD2350 (triangles), PD1952 (closed squares), PD2410 (open squares), PD3428 (open circles), and PD824 (closed circles) in (a) methanol, and (b) DMSO.

In order to make a direct comparison of the limiting ability of each molecule we must examine the limiting at the peak of the ESA spectrum, remembering that all limiting curves were taken at 532 nm. It is possible to get a good idea of what the limiting curve would be at the peak of the ESA spectrum for each dye since we have a reliable model, at least to the turning point, for the picosecond regime and know all the molecular parameters (Table 6.2 and Table 6.4). The only assumption we have to make in doing this is that the higher excited-state cross-section is a constant over this band, and since we know this cross-section at 532 nm we can extrapolate what β would be at the peak of the ESA spectrum. Figure 6.19 shows theoretical curves using the 4-level all singlet energy manifold to model the picosecond limiting for the five dyes at the peak of their ESA spectrum in methanol using the parameters in Table 6.4 and the ESA dynamics in Table 6.2.

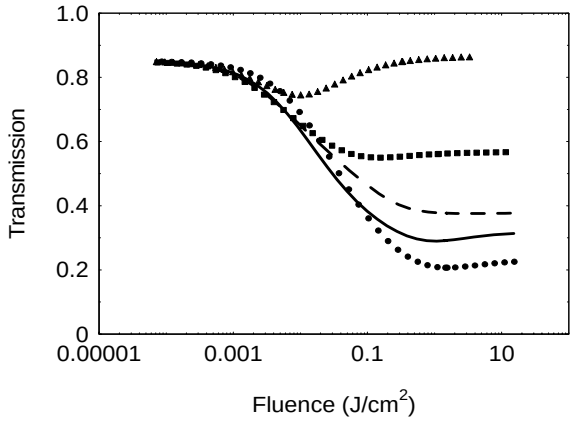

Figure 6.19: Picosecond limiting using peak parameters for the five dyes in methanol: PD2350 (circles) α_{500}: 46, β_{500}: 9, PD1952 (solid line) α_{532}: 84, β_{532}: 7, PD2410 (triangles) α_{594}: 3.2, β_{594}: 0.9, PD3428 (dashed line) α_{532}: 50, β_{532}: 6, PD824 (squares) α_{570}: 23, β_{570}: 3.5

Since there is not a strong solvent dependence on the picosecond optical limiting results as can be seen from Table C.1 we will concentrate on examining the picosecond optical limiting performance as a function of conjugation length and bridge structure using the theoretical curves showing in Figure 6.19. From looking at the experimental data in Figure 6.18 the worst performing dye was PD2350, however when we look at how the material would limit at its peak ESA spectral position (500 nm) it turns out to be the best. It not only has the largest change in transmission (75%), but also the largest turnover fluence (1.23 J/cm^2). This can be attributed to the fact that this molecule has the shortest higher excited-state lifetime ($\tau_{21} \approx 2$ ps) and on average the second largest ratio of excited-state to ground-state cross-section (α). PD2410, which performed the third best in the experiments at 532 nm, would be the worst if the experiments were taken at its ESA spectral peak of 594 nm. This result is mainly connected with this molecule having a large ground-state cross-section ($1.1 \cdot 10^{-16}$ cm^2) at the ESA peak, which is nearly two orders of magnitude larger than the other molecules in this study. This results in the smallest α of only 4. As seen in Figure 6.19 (triangles), this molecule saturates at an extremely low fluence level (0.01 J/cm^2), and has a change of transmittance of only 13%, from which we can conclude that the conjugated bridge structure is detrimental to the ESA properties of polyemthines - at least for picosecond optical limiting. In order from best to worst, the three remaining dyes rank as: PD1952, PD3428, and PD824. It is a little surprising that the tetracarbocyanine (PD824), which has the largest excited-state cross-section, performs worse than the two tricarbocyanines (PD1952, PD3428). Even though this molecule has the largest excited-state cross-section out of the three it has the smallest α and β, which results in a small saturation fluence of 0.13 J/cm^2. The short lifetime of PD824 is not a contributing factor, because

even with a lifetime on the order of 200 picoseconds, it is still over an order of magnitude greater than the pulsewidth. PD1952 and PD3428 are quite similar in both maximum change of transmission ($\approx 60\%$) and turnover fluence (≈ 0.75 J/cm^2), demonstrating that the unconjugated bridge has little effect on the ESA properties of the molecule.

Now we are in position to analyze the nanosecond limiting results since we have examined the picosecond limiting results and have seen which molecules work the best. The results for all five dyes in two solvents are given in Figure 6.20a,b. The results of the nanosecond optical limiting experiments for all dyes, including the linear transmittance (T_L), minimum transmittance, percent change in transmittance, and turnover fluence are summarized in Appendix C in Table C.2. As seen in Figure 6.20 the tricarbocyanines PD1952, and PD3428 are the two best limiters in the nanosecond regime, and the worst is the dicarbocyanine dye, PD2350.

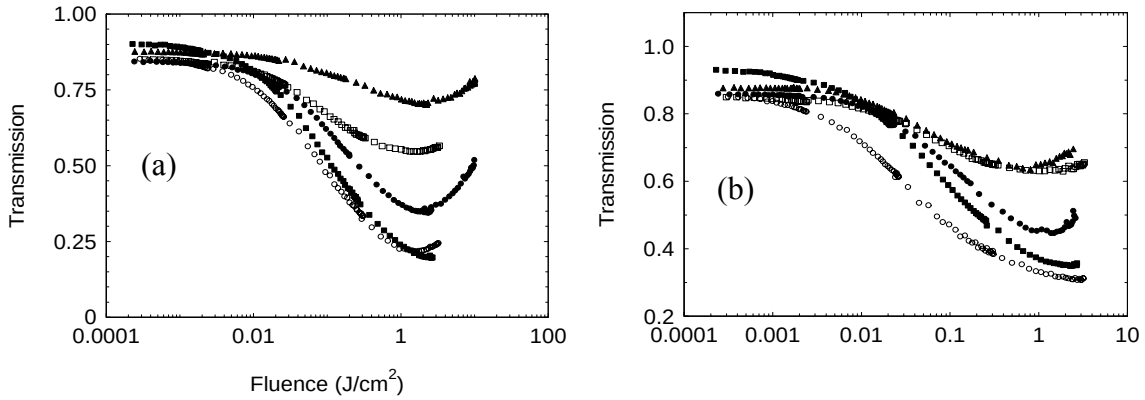

Figure 6.20: Experimental nanosecond limiting results for PD2350 (triangles), PD1952 (closed squares), PD2410 (open squares), PD3428 (open circles), and PD824 (closed circles) in (a) methanol, and (b) DMSO.

As with the picosecond measurements, in order to make a direct comparison of the limiting ability of each molecule we must examine the limiting at the peak of the ESA spectrum. The theoretical curves using the five level model shown in Figure 6.8 with the Peak ESA spectral parameters given in Table 6.4 and β determined as discussed above are shown in Figure 6.21. The dicarbocyanine dye (PD2350) again has the best overall limiting performance with the largest change in transmission (≈ 95%) and the highest turnover fluence (13.4 J/cm^2). The reasons for why this dye was effective in the picosecond regime still apply, but this dye has one feature which is particularly attractive for nanosecond limiting. As can be seen in Table 6.2 the ground state recovery time is very close to the excited-state decay time and the Cis transformation time is very long (30 nanoseconds). This means that the molecule does not easily transform into the Cis-state which appears to have a smaller cross-section than the Trans excited-state. To fit the nanosecond limiting data for PD2410 in methanol and ethanol the four-level all singlet model could be used without the addition of the Cis-state. However, due to the reasons discussed in the picosecond analysis this dye performs very poorly in the nanosecond regime. Therefore, we can conclude that the conjugated bridge structure is good at stabilizing the Trans-state in some host solvents, but this advantage is far out weighed by the reduction in excited-state absorption properties compared to the unconjugated and nonbridged structures of PD1952 and PD3428. These two tricarbocyanines (PD1952 and PD3428), much like for the picosecond limiting results, behave similarly. The turnover fluence and change in transmission of PD1952 and PD3428 is 3.9 and 1.1 J/cm^2, 90% and 75%, respectively. It is interesting to note that the gap in performance between the two tricarbocyanines and the dicarbocyanine has increased in the nanosecond regime. Whereas in the picosecond regime the turnover fluence for PD2350 was

twice as high as the tricarbocyanines it is now 4 and 10 times larger for PD1952 and PD3428, respectively. This can be attributed to the fact that the tricarbocyanines are more easily converting over to the CIS-state thus reducing the population of molecules in the singlet states. Interestingly the limiting properties of the tetracarbocyanine have improved with respect to the other molecules. The turnover fluence for PD824 has improved by an order of magnitude to 1.41 J/cm^2, while its change in transmittance has also improved slightly to 54% from 36%. This could be due to the lower irradiance values in the nanosecond regime so that photodegradition is not as much of a factor as it was in the picosecond regime. Also, as can be seen in Figure 6.21 the limiting starts at a higher fluence value than the other molecules. This is due to the short excited-state lifetime of PD824, which is approximately 5 times shorter than the other molecules.

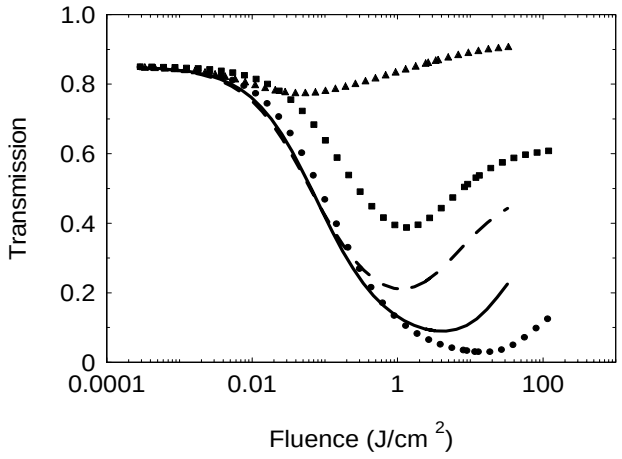

Figure 6.21: Nanosecond limiting using peak parameters for the five dyes in methanol: PD2350 (circles) α_{500}: 46, β_{500}: 9, PD1952 (solid line) α_{532}: 84, β_{532}: 7, PD2410 (triangles) α_{594}: 3.2, β_{594}: 0.9, PD3428 (dashed line) α_{532}: 50, β_{532}: 6, PD824 (squares) α_{570}: 23, β_{570}: 3.5

6.5. Conclusion

We have performed a detailed experimental investigation of five polymethines of chain lengths from di- to tetracarbocyanine in a large class of solvents to determine key molecular and solvent parameters for nanosecond optical limiting. By looking at the experimentally measured optical limiting curves the tricarbocyanine dyes PD1952 and PD3428, which have an ESA peak at 532 nm, seemed to perform the best. But when theoretical curves were generated using molecular parameters at the peak of the ESA spectrum for each molecule the result was different. The main result was that the shortest molecule studied (PD2350) performed the best in both the picosecond and nanosecond time regimes. The unconjugated bridge (PD1952) and nonbridged (PD3428) molecules performed adequately, whereas the conjugated bridge molecule (PD2410) performed very poorly. The fact that the conjugated bridge structure reduces the effectiveness of the ESA properties is a little disappointing since this type of bridge structure seemed to help stabilize the molecule in the Trans-state. The tetracarbocyanine dye (PD824) did not perform as well as the two tricarbocyanines, but showed enough promise that other moieties of this chain length should be investigated. The main limitation of molecules of this chain length or longer appears to be photochemical stability.

In this study we investigated the ESA spectra of the five molecules in up to eight host solvents. From these spectra we not only determined at which wavelength to conduct the Z-scans to measure the peak excited-state cross-section, but we also gained some insight into the nature of ESA in the polymethines. The main characteristic is a larger percentage of the oscillator strength remains in the excited-state transition as the chain length is increased. This helps explain

the important result of measuring an excited-state cross-section that is larger (≈ 3 times) than the ground state cross-section at the peak spectral position. We also observed that the shape of the ESA spectrum and position of the ESA peak did not depend on solvent. This simplified the nonlinear measurements since each molecule in all solvents could be performed at a single wavelength.

The analysis of the excited-state dynamics showed that the excited-state lifetime of molecules slightly increases as a function of the index of refraction of the solvent. The lifetimes of the di- and tricarbocyanines were on the order of 1 nanosecond, whereas the tetracarbocyanine dye was only about 200 picoseconds. The short lifetime of the tetracarbocyanine dye increased the fluence for the onset of limiting by nearly an order of magnitude over the di- and tricarbocyanines. An analysis of the orientational diffusion times was also performed that showed that no specific solvent effect affected the rotational times of the polymethines. This could also be seen by examining the wavelength shift between the absorption and fluorescence spectrums as a function of solvent. The orientational diffusion times could be accurately predicted using the modified SED model including both the Perrin shape factor and dielectric friction. It was also found that four of the five polymethines studied in this chapter followed a stick boundary condition, which makes sense since the polymethine molecules are much larger than the solvent molecules. The shortest dye studied, PD2350, followed a slip boundary condition and the reason for this cannot be completely explained.

Picosecond and Nanosecond Z-scans were performed at the peak of the ESA spectrum for each molecule in all host solvents. For PD2350, PD2410, and PD1952 there is good agreement between the predicted excited-state cross-sections from the picosecond and

nanosecond results, at least within the experimental error of the measurements. For PD3428 and PD824 in which the agreement was not as good the other dyes. This behavior may be explained by additional absorption out of a Cis-states.

The picosecond and nanosecond limiting results provided insight into the ESA properties of the polymethine molecule at high fluence levels. From this data we were able to develop energy level models which can predict limiting in polymethines from the picosecond to the nanosecond time regime. Currently the existence of a Cis-state can only indirectly be inferred from failure of the energy level models developed from the picosecond data to accurately predict the nanosecond results. The evidence however is quite strong that this is indeed the correct model to use. One example is that the short nanosecond pulsewidth measurements for PD2410 predicted that no Cis-state was present, and the long nanosecond pulsewidth measurements agreed with this prediction. Also, the unbridged tricarbocyanine (PD3428), which should be the easiest to transform to a Cis-state had the largest discrepancy between the four-level model and the nanosecond limiting results.

CHAPTER 7: CONCLUSION

7.1. Results

In this dissertation we have studied the excited-state absorption properties of polymethines. We have performed a thorough study of the effects of conjugation length and bridge structure on nanosecond optical limiting performance, which is the main nonlinear optical application of interest. This led to the result that the dicarbocyanine dye (PD2350), which was the shortest molecule studied, performed the best. The formation of a Cis-state in the longer chain polymethines was indirectly observed, and determined as the limiting factor for nanosecond limiting applications. An energy level manifold was developed that models the nonlinear absorption properties of polymethines from the picosecond to the nanosecond regime. The independence of ESA properties of polymethines on host solvent was demonstrated, which will simplify further work with polymethines.

In the course of this research a new technique was developed to determine the spectral position of the energy levels of linear chain molecules as opposed to the typical steady-state fluorescence anisotropy method. This method is based on the two-color picosecond polarization-resolved pump-probe method, which was used to perform the excited-state dynamic measurements. This method is advantageous over the steady-state fluorescence method because it is applicable to nonfluorescent molecules and molecules in low viscosity solvents.

The complicated system of partial differential equations consisting of the rate and propagation equations for the four-level, all-singlet model, which is used to predict saturation of the RSA process in the picosecond regime, was reduced to a single ordinary differential

equation. This allows for quick simulations of material parameters to determine how well the material will limit and when it will saturate in the picosecond regime.

7.2. Future Work

The results of this work show that out of the five molecules studied the shortest dye is the best picosecond and nanosecond optical limiter. Different moieties of this molecule, which include different end groups and bridge structures, should be synthesized and studied. The molecules studied in this dissertation all had very similar end groups so a study could be performed on the effects of end groups on the ESA properties. This would be useful for helping to design better molecules once ideal bridge and conjugation lengths are determined. A detailed photodegradation study should also be performed to determine the cause of the poorness of the limiting fits in the picosecond regime for not only PD2350, but also PD824.

The continued research of the tri- and tetracarbocyanines should be in the direction of understanding the formation of the Cis-state and direct measurement of its properties. A double pump-probe method has been used to study the absorption properties of triplet states [46,47] and could be applied to the investigation of the Cis-state. In order for polymethines to work satisfactorily in the nanosecond regime a way to hinder formation of the Cis-state will be required. Some research is currently being performed in locked all-trans conformations of Oligoenes [107] that may be attempted with polymethines.

The triplet yield of polymethines is extremely small with formation rates on the order of hundreds of nanoseconds. Inserting heavy atoms into the polymethine structure would drastically lower this rate. If this proves too difficult to synthesize, an alternative is to try to use external

heavy atom effects (solvents with heavy atoms) to improve triplet yield and thus optical limiting performance [108].

A new method to determine the spectral position of the energy levels of polymethines molecules was discussed in this dissertation, but its applicability to other molecules has yet to be investigated. The search for a molecule that would give different information from the fluorescence and pump-probe experiments within the wavelength range that we can measure should be continued. Ideally this molecule would have two strong ground state transitions (Q- and B- band transitions) closely spaced in the visible region. Phthalocyanines and porphyrins are candidates, but the spectral separation of the Q and B bands needs to be reduced so that we can measure them using our current laser systems.

APPENDIX A: CHEMICAL STRUCTURES

These PDs were synthesized at the Institute of Organic Chemistry, Kiev, Ukraine. Their molecular structures were confirmed by elemental analysis and nuclear magnetic resonance spectra measurements. Synthesis of most of the dyes was performed by standard methods described in [109]. Specific synthesis for the dyes with bridged polymethine chromopores (PDs 1952, 2410, 2338, 824, and 2332) is described in [110].

Table A.1: Chemical Names of Polymethines

Chemical Label	Chemical Name
PD 2350	2-[5-(1,3-dihydro-3,3-dimethyl-1-propyl-2H-indol-2-ylidene)-1,3-pentadienyl]-3,3-dimethyl-1-propylindolium iodide
PD 2351	2-[5-(1,3-dihydro-3,3-dimethyl-1-propyl-2H-indol-2-ylidene)-3-cyano-1,3-pentadienyl]-3,3-dimethyl-1-propylindolium iodide
PD 2335	2-[2-[3-[(1,3-dihydro-1,3,3-trimethyl-5-phenyl-2H-indol-2-ylidene)ethylidene]-5-methyl-2-(4-methoxyphenyl)-1-cyclohexen-1-yl]ethenyl]-1,3,3-trimethyl-5-phenylindolium tetrafluoroborate
PD 2338	2-[2-[3-[(1,3-dihydro-1,3,3-trimethyl-5-phenyl-2H-indol-2-ylidene)ethylidene]-2-phenyl-1-cyclohexen-1-yl]ethenyl]-1,3,3-trimethyl-5-phenylindolium tetrafluoroborate
PD 824	2-[9-(1,3-dihydro-1,3,3-trimethyl-2H-indol-2-ylidene)-3,7-dimethyl-4,6-(2,2-dimethyltrimethylene)-1,3,5,7-nonatetraenyl]-1,3,3-trimethylindolium perchlorate
PD 2332	2-[9-(1-ethyl-3,3-dimethyl-2H-benzo[e]indol-2-ylidene)-3,7-dimethyl-4,6-(2,2-dimethyltrimethylene)-1,3,5,7-nonatetraenyl]-1-ethyl-3,3-dimethylbenzo[e]indolium perchlorate
PD 2257	2-[3-(1-butyl-6-butoxybenz[c,d]indol-2-ylidene)-1-propenyl]-1-butul-6-butoxybenz[c,d]indolium tetrafluoroborate
PD 3428	3,3,3,3-tetramethyl-1,1-diphenylindotricarbocyanine perchlorate
PD 1952	1,3,3-trimethyl-2-(2-{2-phenyl-3[2-(1,3,3-trimethyl-1,3-dihydroindo-2-ylidene)ethylidene]cyclopent-1-enyl}vinyl)-3H-indolium tetrafluoroborate
PD 2410	1,3,3-trimethyl-2-(2-{2-phenyl-3[2-(1,3,3-trimethyl-1,3-dihydroindo-2-ylidene)ethylidene]cyclopenta-1,4-dienyl}vinyl)-3H-indolium perclhorate
PD 2398	3,3'-Diethyl-5,5-dimethoxy-9,11,15,17-di(β,β-dimethyltrimethylene) thiapentacarbocyanine iodide
PD 1659	3,3'-Diethyl-9,11,15,17-di(β,β-dimethyltrimethylene)thiapentacarbocyanine iodide

APPENDIX B: DERIVATION OF ANISOTROPY EQUATION

In determining the induced anisotropy of an initial isotropic system we must consider what physical processes are occurring and what the system is measuring. First we have to consider the absorption of the excitation source and how it changes an isotropic distribution to an anisotropic distribution. Next we have to take into account the detection of the anisotropy whether it is by fluorescence or absorption of a weak probe; the signal is decomposed into parallel and perpendicular components with respect to the excitation source. Both the creation of the anisotropic distribution and the detection of this distribution play a crucial role in the development of the anisotropy equation given by Eq. 22. We will examine the problem in terms of fluorescence and start from the side of detecting the fluorescence from the emission dipole (μ_e) shown in Figure B.1.

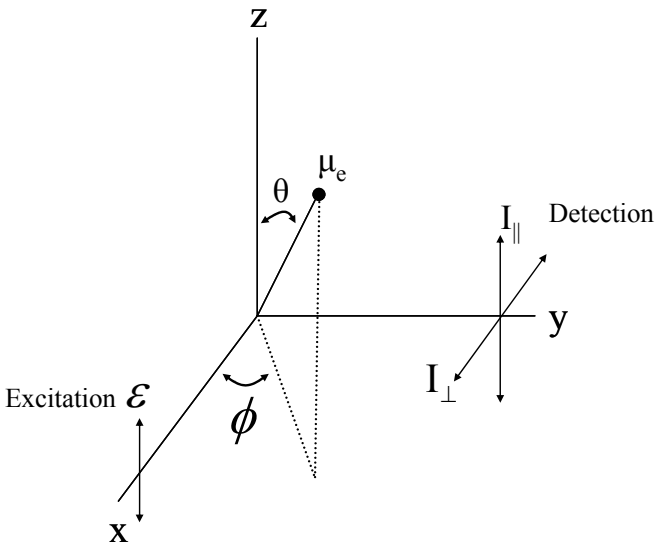

Figure B.1: Laboratory fixed axes with an excited-state dipole moment (μ_e) oriented at (θ,ϕ). The excitation beam (ε) is polarized along z and propagates along x. The fluorescence is detected along y and is decomposed along z (parallel) and x (perpendicular).

For an oscillating dipole (μ_e) oriented at (θ,ϕ), as shown in Figure B.1, the intensity of the emission when observed along the y axis is proportional to [111]:

$$\left|(\hat{y}\times\vec{\mu}_e)\times\hat{y}\right|^2 = \mu_x^2 + \mu_z^2 \tag{45}$$

Therefore, the microscopic intensities from each individual emission transition dipole (μ_e) polarized along the z axis (parallel component) and along the x axis (perpendicular component) are given as:

$$i_{\parallel}(\theta,\phi) \approx \mu_z^2 = \mu_e^2\cos^2(\theta) \tag{46}$$

$$i_{\perp}(\theta,\phi) \approx \mu_x^2 = \mu_e^2\sin^2(\theta)\cos^2(\phi) \tag{47}$$

To obtain the macroscopic intensities the microscopic intensities must be averaged over all orientations and are given as:

$$I_{\parallel} = \iint i_{\parallel}(\theta,\varphi)W_e(\theta,\phi)\sin(\theta)d\theta d\phi \tag{48}$$

$$I_{\perp} = \iint i_{\perp}(\theta,\varphi)W_e(\theta,\phi)\sin(\theta)d\theta d\phi \tag{49}$$

where $W_e(\theta,\phi)$ is normalized distribution of the orientations of the emission dipole moments, or in other words the probability that the emission dipole moment is oriented at (θ,ϕ). The form of $W_e(\theta,\phi)$ depends on the orientation of the absorption dipole moment (μ_a) with respect to the emission dipole moment.

We will first examine the case of when the absorption and emission dipole moments are parallel. So in Figure B.1 we can simply replace μ_e with μ_a, which means that the angle θ represents the angle between the electric field vector (ε) and the absorption dipole moment. In this case $W_e(\theta,\phi) = W_a(\theta,\phi)$, and the probability for a molecule to absorb a photon from the

electric field is proportional to $\left|\vec{\mu}_a \cdot \hat{\varepsilon}\right|^2 = \mu_z^2$. From this the normalized distribution function in this case is:

$$W_a(\theta,\phi) = W_e(\theta,\phi) = \frac{3}{4\pi}\cos^2(\theta) = \frac{1}{4\pi}[1 + 2P_2(\cos(\theta))] \tag{50}$$

where $P_2(\cos(\theta))$ is the second order Legendre polynomial. Substituting Eqs. 46,47, and 50 into Eqs. 48,49 results in $I_{\parallel} = 3/5$ and $I_{\perp} = 1/5$, which results in the anisotropy being $R = 2/5 = 0.4$. Therefore when the absorption and fluorescence dipole moments are parallel the maximum anisotropy of 0.4 is achieved.

Next we will examine the case when the absorption and fluorescence dipole moments are not parallel, and are separated by the angle β, which is anisotropy equation given by Eq. 22 that we are trying to prove. The important quantities are shown in Figure B.2 along with a newly defined coordinate system (x`,y`,z`) which has the emission dipole moment oriented along the z` axis. The focus is on the emission dipole since $W_e(\theta,\phi)$ in Eqs. 48,49 is defined with respect to the initial coordinate system.

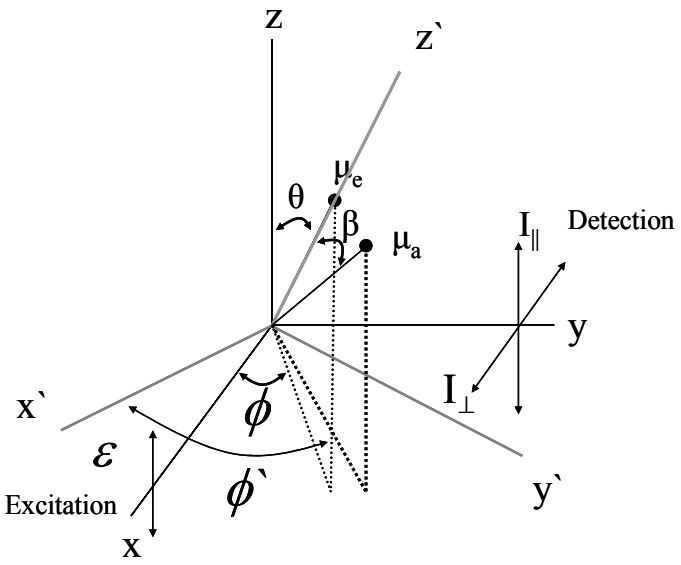

Figure B.2: Laboratory fixed axes with an excited-state dipole moment (μ_e) oriented at (θ,ϕ) in this axes system. And a new axes system with z` aligned with the excited-state dipole moment orientation. Within this new axes system (x`,y`,z`) the absorption transition dipole moment (μ_a) is oriented at (β,ϕ`).

The first thing to do is to determine the relationship between $W_e(\theta,\phi)$ of the initial coordinate system and $W_a(\beta,\phi`)$ of the new coordinate system. To determine the probability of finding an absorption dipole moment ( $\mu_a$ ) with an orientation of $\beta,\phi`$ with respect to z` we integrate only over $\phi`$ since β is fixed. Therefore, the relationship between $W_e(\theta,\phi)$ and $W_a(\beta,\phi`)$ is:

$$W_e(\theta,\phi) = \frac{1}{2\pi} W_a(\beta,\phi`) \tag{51}$$

The normalized absorption dipole moment distribution ($W_a(\beta,\phi`)$) is determined by the dot product of the electric field vector ($\hat{\varepsilon} \| \hat{z}$) and absorption dipole oriented at $\beta,\phi`$ in the new coordinate system and is given as:

$$W_a(\beta,\phi`) = \frac{3}{4\pi}\left[\hat{z}\cdot\hat{\mu}_a(\beta,\phi`)\right]^2 \tag{52}$$

In order to perform the dot product in Eq. 52 a coordinate transformation from the new coordinate system to the old coordinate system must be performed and is given as:

$$\begin{pmatrix}\hat{x}'\\ \hat{y}'\\ \hat{z}'\end{pmatrix} = \begin{pmatrix}\cos(\theta)\cos(\phi) & \cos(\theta)\sin(\phi) & -\sin(\theta)\\ -\sin(\phi) & \cos(\phi) & 0\\ \sin(\theta)\sin(\phi) & \sin(\theta)\sin(\phi) & \cos(\theta)\end{pmatrix}\begin{pmatrix}\hat{x}\\ \hat{y}\\ \hat{z}\end{pmatrix} \tag{53}$$

The total probability is obtained by integrating over all the absorption dipoles and is given as:

$$W_e(\theta,\phi) = \frac{1}{2\pi}\frac{3}{4\pi}\int_0^{2\pi}[z\cdot\hat{\mu}_a(\beta,\phi`)]^2\,d\phi`$$

$$= \frac{1}{2\pi}\frac{3}{4\pi}\int_0^{2\pi}[\sin(\beta)\cos(\phi`)\hat{z}\cdot\hat{x}' + \sin(\beta)\sin(\phi`)\hat{z}\cdot\hat{y}' + \cos(\beta)\hat{z}\cdot\hat{z}']^2\,d\phi'$$

$$= \frac{3}{4\pi}\cos^2(\theta)P_2(\cos(\beta)) + \frac{3}{4\pi}\frac{\sin^2(\beta)}{2} \tag{54}$$

Substituting the new normalized distribution function (Eq. 54) and Eqs. 46,47, into Eqs. 48,49 results in:

$$I_{\|} = \frac{3}{5}P_2(\cos(\beta)) + \frac{\sin^2(\beta)}{2}$$

$$I_{\perp} = \frac{1}{5}P_2(\cos(\beta)) + \frac{\sin^2(\beta)}{2} \tag{55}$$

Which final leads to the anisotropy equation being:

$$R = \frac{2}{5} P_2(\cos(\beta)) = \frac{2}{5}\left[\frac{3\cos^2(\beta) - 1}{2}\right] \tag{56}$$

APPENDIX C: OPTICAL LIMITING RESULTS SUMMARY TABLES

Table C.1: Picosecond Optical Limiting Results

Dye	T_L (%)	Min-Transmission (%)	Percent Change in Transmission	Turnover Fluence (J/cm^2)
PD2350				
Methanol	84	68	19	0.15
Ethanol	82	64	22	0.18
Butanol	83	63	24	0.23
Pentanol	85	66	22	0.21
DMF	83	63	24	0.16
DMSO	82	59	28	0.17
MF	85	67	21	0.17
PC	83	63	24	0.12
PD1952				
Methanol	86	34	60	0.84
Ethanol	89	45	49	1.0
DMF	87	43	51	0.59
DMSO	89	46	48	0.78
MF	89	40	55	0.86
PC	90	46	49	0.72
PD2410				
Methanol	82	55	33	0.12
Ethanol	90	57	37	0.12
DMSO	83	63	24	0.15
PC	85	63	26	0.12
PD3428				
Methanol	88	47	47	0.63
Ethanol	88	52	41	1.3
Butanol	88	56	36	0.66
DMF	86	49	43	0.62
DMSO	89	51	43	1.1
MF	88	49	44	0.36
PC	86	57	34	0.36
PD824				
Methanol	84	49	42	0.22
Ethanol	84	49	42	0.22
Butanol	84	61	27	0.17
Pentanol	93	75	19	0.16
DMSO	86	67	22	0.13
PC	86	65	24	0.12

Table C.2: Nanosecond Optical Limiting Results

Dye	T_L (%)	Min-Transmission (%)	Percent Change in Transmission	Turnover Fluence (J/cm^2)
PD2350				
Methanol	87	70	20	2.22
Ethanol	87	72	17	1.8
Butanol	88	66	25	1.47
Pentanol	90	70	22	1.32
DMF	89	71	20	0.54
DMSO	88	65	26	0.71
MF	89	69	22	0.94
PC	89	66	26	1.78
PD1952				
Methanol	90	20	78	2.87
Ethanol	93	31	67	1.27
DMF	93	34	63	1.35
DMSO	93	35	62	2.45
MF	92	25	73	1.99
PC	91	21	77	1.42
PD2410				
Methanol	85	55	35	1.35
Ethanol	86	58	33	1.00
DMSO	85	63	26	0.83
PC	86	64	26	0.71
PD3428				
Methanol	85	22	74	1.41
Ethanol	85	17	80	1.57
Butanol	85	26	69	0.97
DMF	86	32	63	0.74
DMSO	85	31	64	2.18
MF	84	29	65	1.16
PC	86	21	76	1.07
PD824				
Methanol	84	35	58	2.22
Ethanol	86	41	52	1.87
Butanol	86	41	52	1.51
Pentanol	84	42	50	1.51
DMSO	86	45	48	1.47
PC	87	46	47	1.45

LIST OF REFERENCES

[1] R.W. Boyd, *Nonlinear optics*, Academic Press, 1992.

[2] N. Bloembergen, *Nonlinear optics*, Addison Wesley, 1991.

[3] Y.R. Shen, *The principles of nonlinear optics*, John Wiley and Sons, 1984.

[4] T.H. Maiman, "stimulated optical radiation in ruby," *Nature*, vol. 187, pp. 493, 1960.

[5] P.A. Franken, A.E. Hill, C.W. Peters, and G. Weinreich, " Generation of Optical Harmonics," *Phys. Rev. Lett.*, vol. 7, pp. 118, 1961

[6] D.C. Hutchings, M. Sheik-Bahae, D.J. Hagan, E.W. Van Stryland, " Kramers-Krönig relations in nonlinear optics," *Opt. and Quantum Electron.*, vol. 24, pp. 1, 1992.

[7] G.N. Lewis, D. Lipkin, and T.T. Magel, "Reverse photochemical processes in rigid media. A study of the phosphorescent state*," J. Am. Chem. Soc.* vol. 63, pp. 3005-3018, 1941.

[8] C.R. Giuliano and L.D. Hess, "Nonlinear Absorption of Light: Optical Saturation of Electronic Transitions in Organic Molecules with High Intensity Laser Radiation," *IEEE J. Quantum Electron*., vol. 3, pp. 358-367, 1967.

[9] J.W. Perry, "Organic and Metal-Containing Reverse Saturable Absorbers for Optical Limiters," in Nonlinear Optics of Organic Molecules and Polymers, H. S. Nalwa and S. Miyata, eds. (CRC Press, Boca Raton, Fla., 1997), pp. 813-840.

[10] P. Kafalas, J.I. Masters, and E.M.E. Murray, "Photosensitive liquid used as a nondestructive passive Q-switch in a ruby laser," *J. Appl. Phys.,* vol. 35, pp. 2349-2350, 1964.

[11] B.H. Soffer and B.B. McFarland, "Frequency locking and dye spectral hole burning in Q-spoiled lasers," *Appl. Phys. Letters,* vol. 8, pp. 166-169, 1966.

[12] M. Hercher, W. Chu, and D. L. Stockman, "An experimental study of saturable absorbers for ruby lasers," *IEEE J. Quantum Electron.*, vol. QE- 4, pp. 954-968. 1968.

[13] M. Hercher, "An Analysis of saturable absorbers," *Appl. Opt*., vol. 6, 947-953, 1967.

[14] H. A. Haus, "Theory of mode locking with a slow saturable absorber," *IEEE J. Quantum Electron.,* vol. QE-11, pp. 736-746, 1975.

[15] C. David Decker, "Excited state absorption and laser emission from infrared laser dyes optically pumped at 532 nm," *Appl. Phys. Lett*., vol. 27, pp. 607-609, 1975.

[16] M. M. Fisher, B. Veyret, and K. Weiss, "Non-linear absorption and photoionization in the pulsed laser photolysis of anthracene," *Chem. Phys. Lett.,* vol. 28, pp. 60-65, 1974.

[17] D.J. Harter, Y.B. Band, and E.P. Ippen, "Theory of mode-locked lasers containing a reverse saturable absorber," *IEEE J. Quantum Electron.,* vol. QE-21, pp. 1219-, 1985.

[18] Y.B. Band, D.J. Harter, and R. Bavli, "Optical pulse compressor composed of saturable and reverse saturable absorbers," *Chem. Phys. Lett.,* vol. 126, pp. 280-284, 1986.

[19] D.J. Harter, M.L. Shand, and Y.B. Band, "Power/energy limiter using reverse saturable absorption," *J. Appl. Phys*., vol. 56 (3), pp. 865-868, 1984.

[20] L.W. Tutt, T.F. Boggess, “A review of optical limiting mechanisms and devices using organics, fullerenes, semiconductors and other materials,” *Prog. Quant. Electr.*, vol. 17, pp. 299-338, 1993.

[21] D. Dini, M. Barthel, and M. Hanack, “Phthalocyanines as active materials for optical limiting*,” Eur. J. Org. Chem*., vol. 2001, pp. 3759 -3769, 2001.

[22] Hanack et. al., “Indium phthalocyanines and naphthalocyanines for optical limiting,” *Coord. Chem. Rev,.*vol. 235, pp. 219-221, 2001.

[23] J.W. Perry et. al., “Organic optical limiter with a strong nonlinear absorptive response,” *Science,* vol. 273, pp. 1533-1536, 1996.

[24] J.H. Lim et. al., “Polymethine and squarylium molecules with large excited-state absorption,” *Chem. Phys.*, vol. 245, 79-97, 1999.

[25] A. Mishra et. al., “Cyanines during the 1990s: A Review,” *Chem. Rev.,* vol. 100, pp. 1973-2012, 2000.

[26] N. Tyutyulkov, et. al., Polymethine dyes structure and properties, Sofia, St. Kliment Ohridski University Press, 1991.

[27] Y. Miyazoe and M. Maeda, “Stimulated emission from 19 polymethine dyes-laser action over the continuous range 710-1060 nm,” *App. Phys. Lett.,* vol. 12 (5), pp. 206-208, 1968.

[28] Y.H. Meyer, M. Pittman, and P. Plaza, “Transient absorption of symmetrical carbocyanines,” *J. Photochem. Photobiol.*, vol. A 114, pp. 1-21, 1998.

[29] S. N. R. Swatton, K. R. Welford, S. J. Till, and J. R. Sambles, "Nonlinear absorption of a carbocyanine dye 1,1',3,3,3',3'-hexamethylindotricarbocyanine iodide using a z-scan technique," *Appl. Phys. Lett.*, vol. 66, pp. 1868-1870, 1995.

[30] S. Hughes and B. Wherrett, "Multilevel rate equation analysis to explain the recent observations of limitations to optical limiting dyes," *Phys. Rev. A,* vol. 54, pp. 3546-3552, 1996.

[31] X. Deng, X. Zhang, Y. Wang, Y. Song, S. Liu, and C. Li, "Intensity threshold in the conversion from reverse saturable absorption to saturable absorption and its application in optical limiting," *Optics Commun.*, vol. 168, pp. 207-212, 1999.

[32] C. Li, L. Zhang, M. Yang, H. Wang, and Y. Wang, "Dynamic and steady- state behaviors of reverse saturable absorption in metallophtalocyanine", *Phys. Rev. A*, vol. 49**,** pp. 1149-1157, 1994.

[33] C. Li, J. Si, M. Yang, R. Wang, and L. Zhang, "Excited-state nonlinear absorption in multi-energy-level molecular systems", *Phys. Rev. A*, vol. 51**,** pp. 569-575, 1995.

[34] T. Xia, D. J. Hagan, A. Dogariu, A. Said, E.W. Van Stryland, "Optimization of optical limiting devices based on excited state absorption," *Appl. Opt*., vol. 36**,** pp. 4110-4122, 1997.

[35] K. R. Welford, S. N. R. Swatton, S. Hughes, S. J. Till, G. Spruce, R. C. Hollins, and B. S. Wherrett, "Nonlinear absorption in organic dyes," *Mat. Res. Soc. Symp. Proc.*, vol. 374, pp. 239-256, 1995.

[36] T. H. Wei, T. H. Huang, and T. C. Wen, "Mechanism of reverse saturable absorption in chloro-aluminium phthalocyanine solution studied with Z-scan," *Chem. Phys. Lett.*, vol. 314, pp. 403-410, 1999.

[37] P. Miles, "Bottleneck optical pulse limiters revisited," *Appl. Opt.*, vol. 38**,** pp. 566 – 570, 1999.

[38] P. Miles, "Bottleneck optical limiters: the optimal use of excited-state absorbers," *Appl. Opt*., vol. 33**,** pp. 6965-6979, 1994.

[39] A. Kobyakov, D. J. Hagan, and E. W. Van Stryland, "Analytical approach to dynamics of reverse saturable absorbers," *J. Opt. Soc. Am. B*, vol. 17, pp.1884-1893, 2000.

[40] O. V. Przhonska, J. H. Lim, D. J. Hagan, E. W. Van Stryland, M. V. Bondar, and Y. L. Slominsky, "Nonlinear light absorption of polymethine dyes in liquid and solid media," *J. Opt. Soc. Am B*, vol. 15, pp. 802-809, 1998.

[41] J.A. Armstrong, "Measurement of picosecond laser pulse widths," *Appl. Phys. Lett.*, vol. 10, pp. 16-, 1967.

[42] K.L. Sala, G.A. Kenney-Wallace, and G.E. Hall, "CW autocorrelation measurements of picosecond laser pulses*," IEEE J. Quantum Electron.*, vol. QE-16, pp. 990-996, 1980.

[43] M. Sheik- Bahae, A. A. Said, T. H. Wei, D. J. Hagan, E. W. Van Stryland, "Sensitive Measurement of Optical Nonlinearities Using a Single Beam," *IEEE J. Quantum Electron.,* vol. 26, pp. 760-769, 1990.

[44] W. T. Silfvast, in: Laser Fundamentals, first ed., Cambridge University Press, New York, 1996, pp. 337-345.

[45] A. E. Siegman, "Output Beam Propagation and Beam Quality from a Multimode Stable-Cavity Laser*," IEEE J. Quantum Electron.*, vol. 29 (4), pp. 1212-1217, 1993.

[46] S. N. R. Swatton, K. R. Welford, R. C. Hollins, and J. R. Sambles, "A time resolved double pump-probe experimental technique to characterize excited-state parameters of organic dyes," *Appl. Phys. Lett.*, vol. 71, pp. 10-12, 1997.

[47] J. Schell, D. Ohlmann, D. Brinkmann, R. Levy, M. Joucla, J. L. Rehspringer, and B. Honerlage, "Reverse saturable absorption in C_{60} - doped porous glasses studied by single- and double-pulse pump-probe experiments," *J. Chem. Phys.*, vol. 111, pp. 5929-5937, 1999.

[48] R.A. Negres, O.V. Przhonska, D.J. Hagan, E.W. Van Stryland, M.V. Bondar, Yu.L. Slominsky, A.D. Kachkovski, *IEEE J. on Selected Topics in Quantum Electronics*, vol. 7, pp. 849-863, 2001.

[49] H.E. Lessing, A. Von Jena, "Orientation of $S_1 - S_n$ transition moments of oxazine dyes from continuous picosecond photometry, " *Chem. Phys. Lett.*, vol. 59, pp. 249-253, 1978.

[50] A. Penzkofer, J. Wiedmann, "Orientation of transition dipole moments of rhodamine 6G determined by excited state absorption," *Opt. Commun*., vol. 35, pp. 81-86, 1980.

[51] H.E. Lessing, A. Von Jena, "Separation of rotational diffusion and level kinetics in transient absorption spectroscopy," *Chem. Phys. Lett.*, vol. 42, pp. 213-217, 1976.

[52] A. Von Jena, H.E. Lessing, "Rotational-diffusion anomalies in dye solutions from transient-dichroism experiments," *Chem. Phys.*, vol. 40, pp. 245-256, 1979.

[53] H.E. Lessing, A. Von Jena, "Rotational diffusion of dyes in micellar media from transient absorption," *Chem. Phys.,* vol. 41, pp. 395-406, 1979.

[54] J.R. Lakowicz, in: Principles of Fluorescence Spectroscopy, second edition, Kluwer Academic/Plenum Publishers, New York, 1999.

[55] T. Tao, "Time-dependent fluorescence depolarization and Brownian rotational diffusion coefficients of macromolecules," *Biopolymers*, vol. 8, pp. 609-632, 1969.

[56] H.E. Lessing, A. Von Jena, Laser Handbook

[57] A. Dogariu, T. Xia, D. J. Hagan, A. A. Said, E. W. Van Stryland, and N. Bloembergen, "Purely refractive transient energy transfer by stimulated Rayleigh-wing scattering," *J. Opt. Soc. Am. B*, vol. 14, pp. 796-803, 1997.

[58] R. L. Fork, C. V. Shank, C. Hirlimann, R. Yen, and W. J. Tomlinson, *Opt. Lett.*, vol. 8, pp. 1-4 ,1983.

[59] O.V. Przhonska, D.J. Hagan, E. Novikov, R. Lepkowicz, E.W. Van Stryland, M.V. Bondar, Yu.L. Slominsky, A.D. Kachkovski, "Picosecond absorption anisotropy of polymethine and squarylium dyes in liquid and polymeric media," *Chem. Phys.*, vol. 273, pp. 235-248, 2001.

[60] A. Sanchez-Galvez, P. Hunt, M.A. Robb, M. Olivucci, T. Vreven, H.B. Schlegel, "ultrafast radiationless deactivation of organic dyes: evidence for a two-state two-mode pathway in polymethine cyanines," *J. Am. Chem. Soc.*, vol. 122, pp. 2911-2924, 2000.

[61] Eugene Hecht, in: Optics, third ed., Addison-Wesly, New York, 1998, pp. 604-611.

[62] R.S. Lepkowicz, O.V. Przhonska, J.M. Hales, D.J. Hagan, E.W. Van Stryland, M.V. Bondar, Yu.L. Slominsky, A.D. Kachkovski, "Excited-state absorption dynamics in polymethine molecules detected by polarization-resolved pump-probe method," *Chem. Phys*., vol. 286, pp. 277-291, 2003.

[63] R.S. Lepkowicz, O.V. Przhonska, J.M. Hales, D.J. Hagan. E.W. Van Stryland, M.V. Bondar, Yu.L. Slominsky, A.D. Kachkovski, "Excited-state absorption dynamics in polymethine molecules detected by polarization-resolved pump-probe method," submitted to *Chem. Phys*. 2003

[64] J.S. Craw, J.R. Reimers, G.B. Bacskay, A.T. Wong, N.S. Hush, "Solitons in finite- and infinite-length negative-defect trans-polyacetylene and the corresponding Brooker (polymethinecyanine) cations. I. Geometry," *Chem. Phys.,* vol. 167, 77-99, 1992.

[65] J.S. Craw, J.R. Reimers, G.B. Bacskay, A.T. Wong, N.S. Hush, "Solitons in finite- and infinite-length negative-defect trans-polyacetylene and the corresponding Brooker (polymethinecyanine) cations. II. Charge-density wave," *Chem. Phys.,* vol. 167, pp. 101-109, 1992.

[66] J.R. Reimers, N.S. Hush," Hole, electron and energy transfer through bridged systems. VIII. Soliton molecular switching in symmetry-broken Brooker (polymethinecyanine) cations," *Chem. Phys.*, vol. 176, pp. 407-420, 1993.

[67] Yu.N. Bernatskaya, A.D. Kachkovski, *Teor. Eksper. Khim. (Russian)*, vol. 35, pp. 142-145, 1999.

[68] A.D. Kachkovski, O.O. Zhukova, *Teor. Eksper. Khim. (Russian)*, vol. 37, pp. 280-284, 2001.

[69] M.J.S. Dewar, in: The Molecular Orbital Theory of Organic Chemistry, McGRAW-HILL Book Company, New York, 1969.

[70] A.D. Kachkovski, *Russ. Chem. Rev.*, vol. 66, pp. 647-664, 1997.

[71] S. Daehne, "Color and Constitution: one hundred of research," *Science*, vol. 199, pp. 1163-1172, 1978.

[72] N.S. Bayliss, "A "metallic" model for the spectra of conjugated polyenes," *J. Chem. Phys.*, vol. 16, pp. 287-292, 1948.

[73] H. Kuhn, "A quantum-mechanical theory of light absorption of organic dyes and similar compounds," *J. Chem. Phys.*, vol. 17, pp. 1098-1212, 1949.

[74] W.T. Simpson, "A mathematical treatment of the color of the merocyanine dyes," *J. Amer. Chem. Soc.*, vol. 73, pp. 5359-5363, 1951.

[75] W. Konig, *J. Prakt. Chem.*, 112, 1, 1926.

[76] S. Daehne, J. Ranft, "Proton resonance spectra of simple polymethine dyes," *Z. Phys. Chem. (Leipzig)*, vol. 224, pp. 65-73, 1963.

[77] S. Daehne, "Systematology and broadening of the definition of polymethine dyes," *Z. Chem.*, vol. 5, pp. 441-51, 1965.

[78] S. Daehne, D. Leupold, ","*Angew. Chem.*, vol. 78, pp. 1029, 1966.

[79] S. Daehne, R.Radeglia, “Revision of the Lewis-Calvin rule for characterization of vinyl homologs. Polyene and polymethine-like compounds,” *Tetrahedron*, vol. 27, pp. 3673-3683, 1971.

[80] S. Daehne, S. Kulpe. Structural principles of unsaturated organic compounds, Akademie-Verlag, Berlin, 1977.

[81] A.I. Tolmachev, Yu.L. Slominsky, A.A. Ishchenko, in: Near-Infrared Dyes for High Technology Applications. Ed. Daehne, S., Resh-Genge, U., Wolfbeis, U. Kluwer Acad. Publisher, 1998. pp. 384-515.

[82] S. Hunig, F. Linhardt, J. Liebigs, *Ann. Chem*., vol. 11, pp. 2116-2129, 1975.

[83] J. Fabian, H. Hartmann,” MO-LCAO calculations on polymethines. II. π-Electronic structure of polymethines,” *J. Mol. Struct.*, vol. 27, pp. 67-78, 1975.

[84] J. Bredas, R. Silbey, D. Boudreaux, R. Chance, ”Chain-length dependence of electronic and electrochemical properties of conjugated systems: polyacetylene, polyphenylene, polythiophene, and polypyrrole,” *J. Am. Chem. Soc.*, vol. 105, pp. 6555-6559, 1983

[85] L. Tolbert, M. Ogle, “Electronic spectra of polyacetylene model compounds: α,ω-diphenylpolyenyl anions,” *Synth. Metals*, vol. 41, pp. 1389-1392, 1991.

[86] L. Brooker. In Theory of the photographic process, 3-rd edition, Macmillan, New York, 1991.

[87] L.M. Tolbert, X. Zhao, “Beyond the cyanine limit: Peierls distortion and symmetry collapse in a polymethine dye,” *J. Amer. Chem. Soc.,* vol. 119, pp. 3253-3258, 1997.

[88] W.P. Su, J.R. Schrieffer, A.J. Heeger, "Solitons in polyacetylene," *Phys. Rev. Letters*, vol. 42, pp. 1698-701, 1979.

[89] W.P. Su, J.R. Schrieffer, A.J. Heeger, "Soliton excitations in polyacetylene," *Phys. Rev. B*, vol. 22, pp. 2099-111, 1980.

[90] L.Tolbert, M. Ogle," Carbon-13 NMR spectroscopy of α,ω-diphenylpolyenyl anions. Confirmation of charge localization in soliton model compounds," *J. Am. Chem. Soc.*, vol. 111, pp. 5958-5959, 1989.

[91] L. Tolbert, M. Ogle, "How far can a carbanion delocalize? Carbon-13 NMR studies on soliton model compounds," *J Am. Chem. Soc.*, vol. 112, pp. 9519-9527, 1990.

[92] Yu.N. Bernatskaya, A.D. Kachkovski, *Teoret. i Eksperim. Khem. (Russ.)*, vol. 35 pp. 142-145, 1999.

[93] A.D. Kachkovski, A.I. Tolmachev, Yu.L. Slominsky, M.A. Kudinova, N.A. Derevyanko, O.O. Zhukova. Electronic properties of polymethine systems. Soliton symmetry breaking and spectral features of dyes with a long polymethine chain. Dyes and Pigments, in press.

[94] A. Yu, C. Tolbert, D. Farrow, D. Jonas," Solvatochromism and solvation dynamics of structurally related cyanine dyes," J. *Phys. Chem. A*, vol.106, pp. 9407-9419, 2002.

[95] D.A. Oulianov, A.S. Dvornikov, P.M. Rentzepis, "Optical limiting and picosecond relaxation of carbocyanines upper electronic states," *Opt. Commun.,* vol. 205, pp. 427-436, 2002.

[96] R.S. Lepkowicz, O.V. Przhonska, J.M. Hales, D.J. Hagan. E.W. Van Stryland, M.V. Bondar, Yu.L. Slominsky, A.D. Kachkovski, "Nature of the electronic transitions in thiacarbocyanine with a long polymethine chain," submitted to *Chem. Phys*. 2003.

[97] G.B. Dutt, V.J.P. Srivatsavoy, A.V. Sapre, "Rotational dynamics of pyrrolopyrrole derivatives in alcohols: Does solute-solvent hydrogen bonding really hinder molecular rotation," *J. Chem. Phys.*, vol. 110 (19), pp. 9623-9629, 1999.

[98] G.B Dutt, S. Raman, "Rotational dynamics of coumarins: An experimental test of dielectric friction theories," *J. Chem. Phys.*, vol. 114 (15), pp. 6702-6713, 2001.

[99] C. Hu, R. Zwanzig, "Rotational fiction coefficients for spheroids with the slipping boundary condition," *J. Chem. Phys*., vol. 60 (11), pp. 4354-4357, 1974.

[100] F. Perrin, "Mouvement Brownien D'un ellipsoide (I). Dispersion dielectrique pour des molecules ellipsoidales," *J. Phys. Radium*, vol. 5, pp. 497-511, 1934.

[101] J. R. Knutson, J. M. Beechem, and L. Brand, "Simultaneous analysis of multiple fluorescence decay curves: a global approach," *Chem. Phys. Lett.*, vol. 102 (6), pp. 501-507, 1983.

[102] M. Levitus, R. Martin Negri, and P.F. Aramdenia, "Rotational relaxation of carbocyanines. Comparitive study with isomerization dynamics," *J. Phys. Chem.*, vol. 99, pp. 14231-14239, 1995.

[103] F. Momicchioli, I. Baraldi, and G. Berthier, "Theoretical study of Trans-Cis photoisomerism in polymethine cyanines," *Chem. Phys.*, vol. 123, pp. 103-112, 1988.

[104] P. Brochard, V. Grolier-Mazza, and R. Cabanel, "Thermal nonlinear refraction in dye solutions: a study of the transient regime," *J. Opt. Soc. Am. B*, vol. 14 (2), pp. 405-414, 1997.

[105] J. Robertson, P. Milsom, J. Duignan, and G. Bourhill, "Spatial redistribution of energy in a nanosecond laser pulse by an organic optical limiter," *Opt. Lett.*, vol. 25, pp. 1258-1260, 2000.

[106] Barnard Valuer, in: Molecular Fluorescence Principles and Applications, Wiley-VCH, New York, 2002.

[107] U. Lawrentz et. al.," Donor-acceptor oligoenes with a locked all-trans conformation: synthesis and linear and nonlinear optical properties," *Chem. Eur. J.,* vol. 8 (7), pp. 1573-1590, 2002

[108] C. Liu, X. Wang, et. al., "External heavy atom effect on optical limiting performance of conjugated phthalocyanine pentamer," *Chem. Phys. Lett.,*vol. 347, pp. 378-382, 2001.

[109] M. Hamer, in: The cyanine dyes and related compounds, Interscience Publisher, New York, 1964, p. 790.

[110] A.I. Tolmachev, Yu.L. Slominsky, and A.A. Ischenko, New cyanine dyes absorbing in the NIR region, in: Near-Infrared Dyes for High Technology Applications, in: S. Daehne, U. Resh-Genger, O. S. Wolfbeis (Eds.), NATO ASI Series, vol. 52, Kluger Academic Publishers, Dordrecht, Boston, London, 1998, 385-415.

[111] John D. Jackson, in: Classical electrodynamics, John Wiley & Sons, New York, 1998.